NASA TECHNICAL MEMORANDUM NASA TM-77292

CLEARANCE FLOW-GENERATED TRANSVERSE FORCES AT THE ROTORS OF THERMAL TURBOMACHINES

Karl Urlichs

(NASA-TM-77292) CLEARANCE FLOW-GENERATED TRANSVERSE FORCES AT THE ROTORS OF THERMAL TURBOMACHINES Ph.D. Thesis - Technische Univ., 1975 (National Aeronautics and Space Administration) 181 p HC A09/MF A01 N85-16180

G3/37 Unclas 13672

Translation of "Durch Spaltstroemungen hervorgerufene Querkraefte an den Laufern Thermischer Turbomaschinen", Muenchen, Technische Universitaet, Fachbereich Maschinenwesen, Doctoral Dissertation, 1975, pp. 1-159.

NATIONAL AERONAUTICS AND SPACE ADMINISTRATION
WASHINGTON, D.C., 20546 OCTOBER 1983

1. Report No. NASA TM-77292	2. Government Accession No.	3. Recipient's Catalog No.
4. Title and Subtitle CLEARANCE FLOW-GENERATED TRANSVERSE FORCES AT THE ROTORS OF THERMAL TURBO-MACHINES		5. Report Date October 1983
		6. Performing Organization Code
7. Author(s) Karl Urlichs		8. Performing Organization Report No.
		10. Work Unit No.
9. Performing Organization Name and Address SCITRAN Box 5456 Santa Barbara, CA 93108		11. Contract or Grant No. NASw- 3542
		13. Type of Report and Period Covered Translation
12. Sponsoring Agency Name and Address National Aeronautics and Space Administration Washington, D.C. 20546		14. Sponsoring Agency Code

15. Supplementary Notes

Translation of "Durch Spaltstroemungen hervorgerufene Querkraefte an den Laufern Thermischer Turbomaschinen", Muenchen, Technische Universitaet, Fachbereich Maschinenwesen, Doctoral Dissertation, 1975, pp. 1-159. (A76-43249)

16. Abstract

Self-excited rotor whirl represents a serious hazard in the operation of turbomachines. The reported investigation has, therefore, the objective to measure the lateral forces acting on the rotor and to determine the characteristic pressure distribution in the rotor clearance area. A description is presented of an approach for calculating the leakage flow in the case of an eccentric rotor position on the basis of empirical loss coefficients. The results are reported of an experimental investigation with a turbine stage, taking into account a variation of the clearance characteristics.

17. Key Words (Selected by Author(s))		18. Distribution Statement Unclassified-Unlimited	
19. Security Classif. (of this report) Unclassified	20. Security Classif. (of this page) Unclassified	21. No. of Pages 179	22. Price

I want to express my special gratitude to professor Dr. Eng. K.-J. Thomas, who as discoverer of clearance excitation provided the stimulus for this work and who always encouraged its progress with his interest.

I owe a debt of gratitude to all my colleagues at the Institute, especially engineer R. Wohlrab, for stimulating discussions and valuable suggestions. I also want to thank the Institute's machine-shops, which contributed substantially to the accomplishing of this effort. The test turbine manufacture was undertaken in part by AEG-Kanis. The measurements were performed within the research project "Rotor instability due to clearance excitation".

The numerical calculations were performed at the Leibniz Computer Center of the Bavarian Academy of Sciences, whose collaborators I would like to thank for their friendly assistance.

Munich, July 1975

Karl Urlichs

TM-77292

CLEARANCE FLOW-GENERATED TRANSVERSE FORCES AT THE ROTORS OF THERMAL TURBOMACHINES

[Durch Spaltstroemungen herforgerufene Querkraefte and den Laeufern thermischer Turbomachinen]

D i s s e r t a t i o n

authorized by the
Professional area Mechanical Engineering
of the
Technical University of Munich

to obtain the degree of
Doctor in Engineering

Submitted by
Eng. Karl Urlichs

1st Reporter: Prof. Dr. Eng. H.-J. Thomas
2nd Reporter: Prof. Dr. Eng. J. Raabe

Submission date: 07-03-1975
Acceptance date: 09-25-1975
Graduation date: 09-29-1975

TABLE OF CONTENTS

Page

1 INTRODUCTION /1*

In an engineering effort to significantly raise the output of turbomachine units, in high pressure turbines there appear, to an ever increasing extent, flexural vibrations unrelated to the rotational speed, placing severe operating restrictions on rotors that are thermodynamically properly designed. This output-dependent excitation of self-generated vibrations is not caused by bearing instability, but by forces produced as a consequence of the clearance flow generated between rotor and housing [1-4]. The development of these forces is generally summarized under the concept of clearance excitation.

A theoretical description of the vibrational system is already available [9, 10], for multi-supported shafts of any form. However, the treatment assumes knowledge of the support characteristics and the clearance excitation forces. Recently, several important papers have been published (for instance, [6]) in the area of friction bearing research; with their help, bearing instability (oil whip) can be substantially avoided by means of constructive measures. In addition, it is possible to determine system damping, which in a vibrating turbine shaft is predominantly caused by the bearings. In publications to date on rotor instability due to clearance excitation, the exciting forces are determined almost exclusively via theoretical statements based on Thomas' [1] fundamental considerations. Only recently have measurements become available [5] that allow a reliable estimation of the limiting output.

The clearance excitation forces originate in the sealing clearance - variable around the perimeter - that occurs when a deflection exists between turbine rotor and casing. Due to the changing clearance loss, the rotor blades are subjected to differing /2
peripheral forces, the resultant of which has an exciting

* Numbers in the margin indicate foreign pagination

effect, for a shaft vibrating in the same sense as the direction of rotation. Since in turbine stages the rotor's peripheral velocity is very large, the flow through the sealing clearance is of spiral type. For an eccentric rotor position, the consequence is a pressure distribution that varies along the perimeter - due to the different flow cross-sections - which in the case of banded "buckets" considerably magnifies the exciting forces.

The goal of this study is the measurement of the transverse forces acting on the rotor, as well as the determination of the characteristic pressure distribution in the rotor clearance. In addition, a procedure is provided with which the clearance flow, affected by torsional forces, can be calculated for eccentric rotor positioning, by means of empirical loss coefficients. The result contains the variable clearance throughput and the pressure distribution at the sealing clearance under consideration. This provides the two characteristics of the clearance flow through which transverse forces proportional to the lateral deflection act on the rotor.

2. FUNDAMENTAL CONSIDERATIONS AND STATUS OF RESEARCH

2.1. General definition based on a rotor model

$$\varphi_x = -\frac{\partial y}{\partial z}, \qquad \varphi_y = \frac{\partial x}{\partial z}.$$

The complex configuration of a turbine rotor can be represented

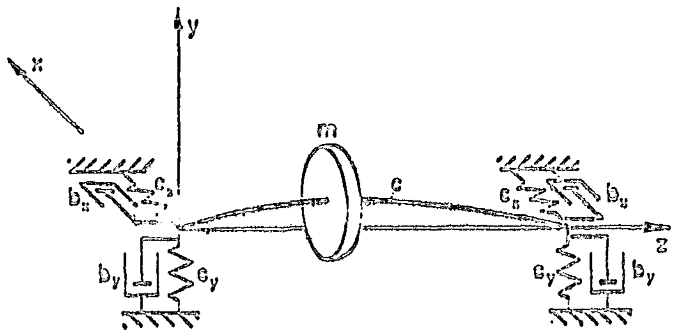

Figure 2.1 Rotor model

by sections of constant cross-section, provided the subdivisions are sufficiently small. The dynamics of each section is described by a system of differential equations which can be solved closed, in the linear case. Matrix transfer procedures are best suited to the description of such elastomechanic problems. They allow a particularly clear expression of the quantities describing the rotor elements. The knowledge of the external forces acting through the flow processes is of essential importance. They shall be defined below in a generally valid manner.

Figure 2.1, above, shows a simple vibration model, suitable for fundamental studies. For the spatial coordinates x, y and z, the z-axis describes the shaft's stationary rest position. If we represent the shaft's deformed center-line in a top and side projection, according to Figure 2.2, below, then we have, for the bending angle

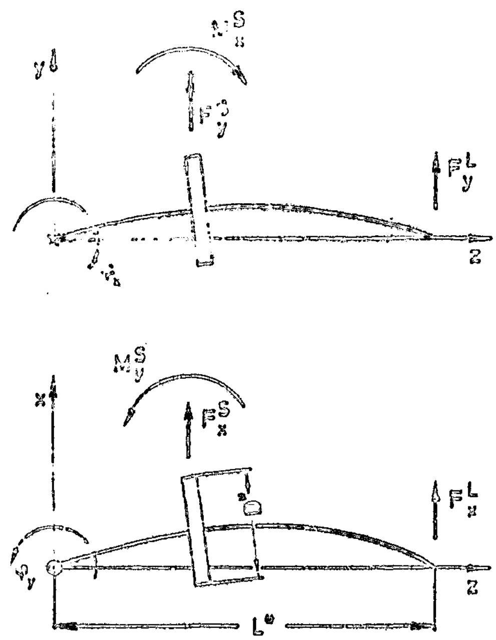

/4

Figure 2.2 Force definition on rotor model

As usual, the external forces acting on the rotor are defined as positive in the direction of the coordinates. The same applies also for external moments, in the right-handed system chosen.

Assuming small dynamic displacements, the external forces and moments occurring in addition to the stationary load can be assumed to be linear. In terms of this linear theory, the load vector $\mathcal{L}$ as a function of the motion vector w can be described as follows, in matrix notation:

$$\mathcal{L} = \mathcal{R}\, w + \tilde{\mathcal{R}} \frac{\partial w}{\partial t} . \qquad (2.1)$$

If we now consider only the forces $\underline{F}$ and moments $\underline{M}$ acting from the outside on the turbine shaft, then the load vector $\mathcal{L}$ and the motion vector $\mathfrak{w}$ are defined by

$$\mathcal{Y}_F = \begin{bmatrix} F_x \\ F_y \\ M_x \frac{2}{D} \\ M_y \frac{2}{D} \end{bmatrix}, \qquad \mathfrak{w} = \begin{bmatrix} x \\ y \\ \varphi_x \frac{D}{2} \\ \varphi_y \frac{D}{2} \end{bmatrix}. \qquad (2.2)$$

Considering the symmetry conditions - applicable because of /5
the problem's isotropy- the forces and moments caused by the flow will in general be described by the coefficients of the deflection matrix $\mathcal{R}_S$ and the velocity matrix $\bar{\mathcal{R}}_S$. The coefficients of this matrix have the dimensions of a spring or respectively, damping constant. For a shaft rotating clockwise, their sign will be given by the coordinate system to be introduced later, which rotates with the vibrational motion.

$$\mathcal{R}_S = \begin{bmatrix} q_1 & -q_2 & q_3 & q_4 \\ q_2 & q_1 & -q_4 & q_3 \\ p_1 & -p_2 & p_3 & p_4 \\ p_2 & p_1 & -p_4 & p_3 \end{bmatrix}, \qquad \bar{\mathcal{R}}_S = \begin{bmatrix} a_1 & -a_2 & a_3 & a_4 \\ a_2 & a_1 & -a_4 & a_3 \\ b_1 & -b_2 & b_3 & b_4 \\ b_2 & b_1 & -b_4 & b_3 \end{bmatrix}. \qquad (2.3)$$

The bearings' dynamic restoring forces can be represented in the spatial coordinate system x, y in a similar manner. In general, the symmetry conditions expressed above are not satisfied here. On the other hand, assuming point-bearings, the external moments vanish. In addition, forces due to the bearings' tilt as a rule can be neglected. The deflection matrix $\mathcal{R}_L$ and the velocity matrix $\bar{\mathcal{R}}_L$ for the bearing forces then are

$$\mathcal{R}_L = \begin{bmatrix} -c_{xx} & -c_{xy} & 0 & 0 \\ -c_{yx} & -c_{yy} & 0 & 0 \\ 0 & 0 & 0 & 0 \\ 0 & 0 & 0 & 0 \end{bmatrix}, \qquad \bar{\mathcal{R}}_L = \begin{bmatrix} -d_{xx} & -d_{xy} & 0 & 0 \\ -d_{yx} & -d_{yy} & 0 & 0 \\ 0 & 0 & 0 & 0 \\ 0 & 0 & 0 & 0 \end{bmatrix}. \qquad (2.4)$$

The bearings' characteristic quantities are composed of four spring and damping constants, whose sign is established by the coordinate system above. For the usual friction bearings a large volume of tests results is already available from Glienicke [6]. It should be pointed out that in those papers the direction of rotation is defined inversely, with the consequence that the signs must be changed during the transfer to the coordinate system chosen here.

/6

2.2 Simple rotor stability behavior

In turbine engineering, the force Q_2, described by the coefficient q_2, is of decisive significance. It acts perpendicularly to the direction of deviation and for a codirectionally vibrating shaft acts against the damping force. This can incite the system to self-generated vibration. Figure 2.3, below shows, in a defined coordinate system x, y the intersection point, displaced by the quantity $\underline{e}$ with the angle ψ, for a shaft rotating with angular velocity ω. The temporal derivative of the angle ψ represents the circular frequency ω_s of the vibrational movement.

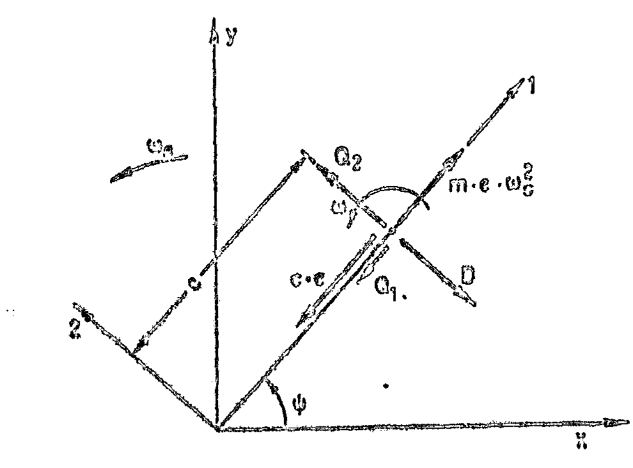

Figure 2.3 Vector diagram for circumpolar vibrations

In the system rotating around the stationary position, the centrifugal force $m e \omega_s^2$ acts in deviation direction "1" and against it, the spring force $-ce$, together with restoring force $-Q_1$, determined by the flow. The damping force D, balanced at the limit of stability by the force Q_2, acts against the vibrational motion. While the restoring force can be neglected, in turbines - because of its small magnitude - in comparison to the spring forces, the determination of the excitation force Q_2 is the main goal of this study.

Building on Thomas' fundamental work [1], several papers /7
contain theoretical considerations on the effect of external forces on the stability behavior of simple rotor models. In analogy to Thomas, Gasch [7] investigates - for rigid bearings - the effect of only the excitation constant q_2 for a central arrangement of the mass, while Piltz [13] takes into acount all the coefficients of the matrices R_s and D_s in an asymmetrical rotor. The stability limits for the simply engaged Laval shaft, taking the effect of friction bearings into account through consideration of the clearance excitation force Q_2, was calculated by Kraemer [2], Pollmann [3] and Vogel [9].

An example of such calculations is shown in Figure 2.4, below. A stability value was formed with the shaft rigidity c and the excitation constant q_2 which is plotted against the shaft's /8

$$\sigma = \frac{q_2}{c}$$

ajustment ω/ω_k. Besides the bearing type, the relative shaft

$$\alpha = \frac{mg}{c}\,\frac{1}{2R\psi}$$

elasticity was varied, which indicates the ratio of static flexure under its own weight, to the friction bearing's diameter play. The

Sommerfold coefficient $So_k = \frac{mg}{2bd}\,\frac{\psi^2}{\eta\,\omega_k}$

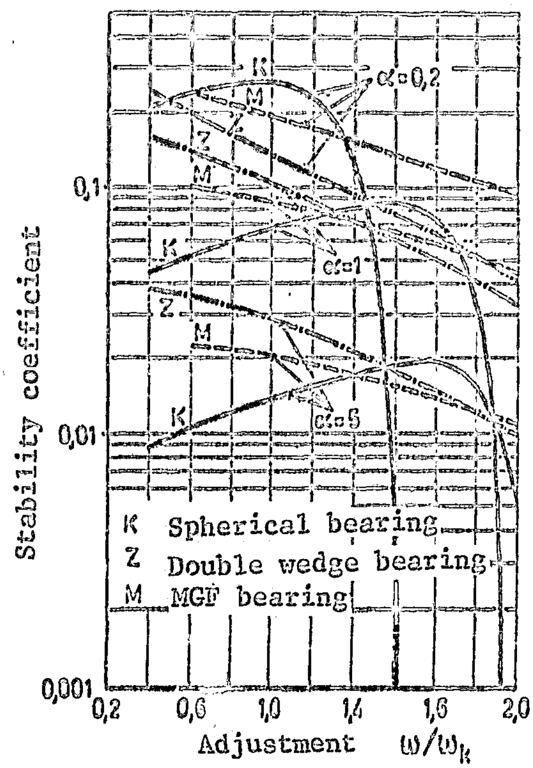

Figure 2.4 Stability chart for the symmetrical unit-mass vibrator with friction bearings. $So_k = 0.2$; $b/d = 0.5$

and the bearing's width ratio b/d is kept constant. Below the characteristic limiting curve the shaft is stable, while above it instability begins. The steep drop of the rotational rate - which increases with ω/ω_k - characterizes instability due the friction bearing's so-called oil whip.

Essential information regarding the construction of a turbine shaft can be derived from stability charts of this kind. However, a quantitatively accurate vibration calculation is possible only when the rotor's geometry has been defined more accurately, by subdivision into individual fields, and once the shafting's multiple support can be taken into account. This was solved, for instance, by matrix transfer procedures, by Schirmer [10] and Vogel [9], as well as by Gasch with finite elements [8].

2.3 Flow-generated forces - Research status /9

When turbine rotors are mounted in casings, at the non-contact sealing clearances of the stator and the rotor, of necessity clearance widths will differ along the circumference. This leads to clearance loss and tangential force differences at the rotor and in turn, to a resulting transverse force at the shaft. In addition, an asymmetrical pressure distribution appears at the sealing clearances, which generates a force that acts on the rotor. For a vibration calculation, both components - the transverse force from clearance loss Q_S and that from the pressure distribution Q_D - must be added.

$$Q = Q_S + Q_D . \qquad (2.5)$$

To the extent that those forces Q are linear and a function of the deflection $\underline{e}$, the constants $q = Q/e$ of the deflection matrix of equation (2.3) are easily determined.

The flow velocity caused by these forces in the usual turbines are two orders of magnitude higher than the rotor's vibration velocity. It is for this reason that forces from the matrix in equation (2.3) that are proportional to the velocity, can as usually be neglected.

2.3.1 Forces from the variable tangential force at the rotor grid

2.3.1.1. Eccentric rotor position

A first physical explanation of an excitation force [1] starts from the premise that a turbine rotor as shown in Figure 2.5, below, will experience uneven tangential forces, for a deflection e. For a small local sealing clearance ($\psi = 0$), due to the low clearance loss the peripheral force will be larger, while it will be correspondingly smaller at the diametrically opposed side.

/10

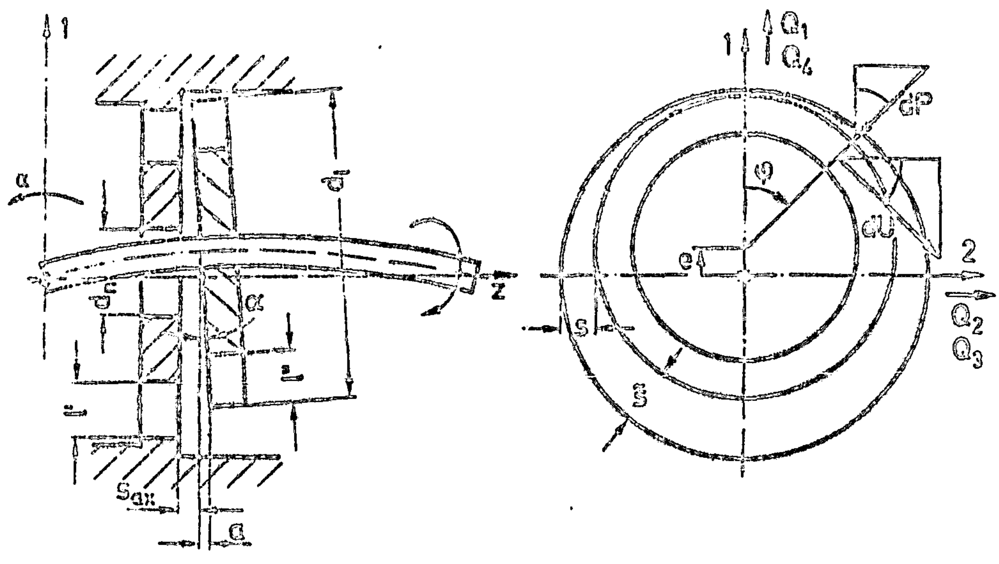

Figure 2.5 Derivation of the clearance excitation forces

The peripheral or tangential force U_i of a turbine stage is obtained from the specific work, a_i, the throughput, $\dot{m}$, and the tangential velocity, u:

$$U_i = \frac{a_i \dot{m}}{u} . \qquad (2.6)$$

The dependence of the internal tangential force U_i on the sealing clearance width can be represented either by the minimum work, a_{sp} [14], or as in [1], by a quantity-loss, $\dot{m}_{sp}$. Both effects can be combined in the tangential velocity lost due to the clearance,

$$U_{sp} = U_u - U_i \tag{2.7}$$

where U_u is the tangential force without clearance losses. If we define the isentropic tangential force, U_s, that would be attained with a loss-free flow, then the internal and the peripheral efficiency, as well as the clearance loss can be represented as force ratios

/11

$$\eta_u = \frac{U_u}{U_s}, \quad \eta_i = \frac{U_i}{U_s}, \quad \xi_{sp} = \frac{U_{sp}}{U_s}. \tag{2.8}$$

For the local tangential force we thereby obtain the simple equation

$$dU_i = U_i \frac{d\varphi}{2\pi} = U_s(\eta_u - \xi_{sp})\frac{d\varphi}{2\pi}. \tag{2.9}$$

The integral of this force along the rotor perimeter yields - using the coordinates of Figure 2.5 - the forces acting on the rotor; the constant tangential efficiency, n_u, cancels out.

$$\left.\begin{aligned} Q_{1s} &= -\int_0^{2\pi} dU_i \sin\varphi = \frac{U_s}{2\pi}\int_0^{2\pi} \xi_{sp} \sin\varphi \, d\varphi, \\ Q_{2s} &= \int_0^{2\pi} dU_i \cos\varphi = -\frac{U_s}{2\pi}\int_0^{2\pi} \xi_{sp} \cos\varphi \, d\varphi. \end{aligned}\right\} \tag{2.10}$$

This integral can be solved only if the local clearance loss along the perimeter of the variable sealing clearance is known.

There are equations for the dependence of clearance loss on clearance width in several of the papers comparatively reviewed by Winter [11]. According to Traupel [14], clearance loss can be expressed as the ratio of lost work, a_{sp}, caused by the sealing clearance to the available isentropic heat gradient, Δh_s,

$$\xi_{sp} = \frac{a_{sp}}{\Delta h_s} . \qquad (2.11)$$

If the isentropic tangential force is defined by

$$U_s = \frac{\dot{m}\,\Delta h_s}{u} , \qquad (2.12)$$

/12

then the clearance loss, ζ_{sp}, is identical to equation (2.8), where the tangential force, reduced by the clearance effect takes the value of equation (2.6).

The stage clearance loss is composed of a loss at the stator blades, ζ'_{sp}, and a loss at the rotor blades, ζ''_{sp}:

$$\xi_{sp} = \xi'_{sp} + \xi''_{sp} = \frac{A'_{sp}}{A'}\,\frac{K'}{\sqrt{z'}} + \frac{A''_{sp}}{A''}\,\frac{K''}{\sqrt{z''}} .$$

It depends primarily on the ratio of the clearance area, A_{sp}, to the grid transverse area, A, and on a factor K, which essentially depends on the design and the inclination of the seal.

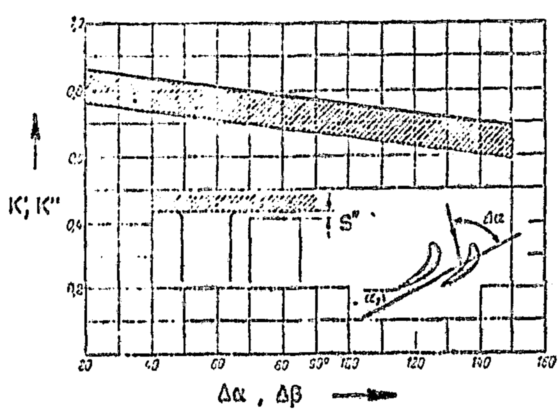

Figure 2.6 Clearance loss coefficient ("buckets" without shroud band)

For blades or "buckets" without shroud band, according to Figure 2.6, above, K' or, respectively, K", depend only on the angle $\Delta\alpha$, or respectively, $\Delta\beta$, on flow deflection. For buckets with shroud bands and stator bases a dependency results on the already mentioned inclination of the stator, $2\Delta h'_s/C_1^2$, or the rotor, respectively, $2\Delta h''_s/w_2^2$, according to Figure 2.7, below. Here

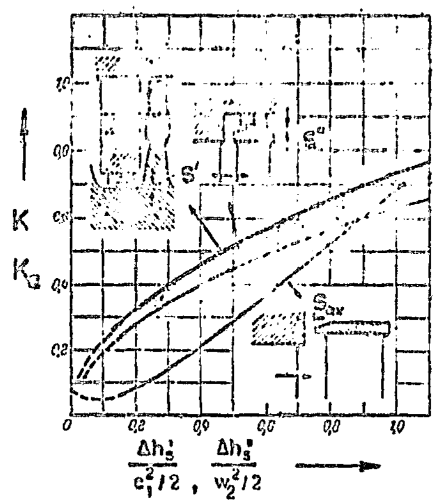

Figure 2.7 Clearance loss coefficient ("buckets" with shroud band)

we must appropriately use the inclination at the base of the blade for the stator, and for the rotor that at the blade head. For labyrinth seals, the clearance loss is reduced depending on the number of clearance peaks, z', or respectively, z". For the areas, in the general case of a chamber step according to Figure 2.5, we shall have

$$A' = \pi\, d_m\, l' \sin\alpha_1, \quad A'' = \pi\, d_m\, l'' \sin\beta_2,$$

$$A'_{sp} = \pi\, d_n\, s', \qquad A''_{sp} = \pi\, d_i\, s''.$$

We thus obtain, for the clearance loss,

$$\zeta_{sp} = \frac{K'}{\sqrt{z'}\,\sin\alpha_1}\,\frac{d_n}{d_m}\,\frac{s'}{l'} + \frac{K''}{\sqrt{z''}\,\sin\beta_2}\,\frac{d_L}{d_m}\,\frac{s''}{l''} \,. \qquad (2.13)$$

Consequently, the clearance loss at the stator and at the rotor depend linearly on the clearance width. If we assume - neglecting compensating flows - that the dependence is applicable also to local clearance widths

$$\left.\begin{aligned} \tilde{s}' &= s' - e\cos\varphi, \\ \tilde{s}'' &= s'' - e\cos\varphi \end{aligned}\right\} \qquad (2.14)$$

according to Figure 2.5, then we obtain, from equation (2.10)

/14

$$\left.\begin{aligned} Q_{1s} &= 0, \\ Q_{2s} &= \frac{1}{2}\,U_s\,\frac{e}{l''}\left[\frac{K'}{\sqrt{z'}\,\sin\alpha_1}\,\frac{d_n}{d_m}\,\frac{l''}{l'} + \frac{K''}{\sqrt{z''}\,\sin\beta_2}\,\frac{d_L}{d_m}\right]. \end{aligned}\right\} \qquad (2.15)$$

Because of the direct proportionality between clearance loss and clearance width, the force vanishes in the direction of deflection.

The clearance excitation force, Q_{2s}, depends linearly on the eccentricity e/l" mentioned, the isentropic tangential force, U_s and the coefficient K_{2s}, which basically describes the construction form of the seal.

$$\frac{Q_{2s}}{U_s} = K_{2s}\,\frac{e}{l''}\,, \qquad (2.16)$$

$$K_{2s} = \frac{1}{2}\left[\frac{K'}{\sqrt{z'}\,\sin\alpha_1}\,\frac{d_n}{d_m}\,\frac{l''}{l'} + \frac{K''}{\sqrt{z''}\,\sin\beta_2}\,\frac{d_n}{d_m}\right]. \qquad (2.17)$$

In the dimensionless representation of equation (2.16), K_{2s} indicates the slope of the excitation force mentioned, Q_{2s}/U_s, over the relative eccentricity e/l" and is therefore referred to as clearance excitation coefficient K_{2s}.

In principle, non-linear clearance loss equations could also be used for the integration of the local tangential force, such as those contained in the 2nd edition of [14], for instance. This effect is discussed in section 4.4.2, in connection with a measured efficiency distribution. It is shown there that even with a non-linear approach for $\zeta_{sp}(s)$, forces can develop that depend linearly on the eccentricity $\underline{e}$, just as here.

/15

2.3.1.2. Rotor-to-housing inclination

Forces acting on the rotor can also be caused by an inclination of the rotor with respect to the housing, if the axial sealing effect of the clearance is significant. In general, according to Figure 2.5, the inclination of the rotor along the shaft's bending line is coupled to a certain eccentricity. If we start from the premise that the radial clearance width is large in comparison to the axial sealing clearance, then the clearance loss will be determined only by the axial clearance. For this type of construction clearance loss equations exist, as in [14], conforming to Figure 2.7 that make it possible to calculate the forces acting on the rotor, which in this case will be due only to the inclination. The local axial clearance of the rotor

$$\tilde{s}_{ax} = s_{ax} - a \cos\varphi \qquad \text{with} \qquad a = \frac{d_i}{2} \operatorname{tg}\alpha \qquad (2.18)$$

shroud band towards the housing changes along the perimeter according to Figure 2.5, for an inclination of the disc equal to the bending angle α. The magnitude of the non-uniformity $\underline{a}$ depends on the angle of inclination α, and on the diameter d_i of the seal. The clearance loss is again taken as linear with respect to the ratio of the seal area and the rotor area,

$$\zeta_{sp,a} = \frac{s_{ax}}{l''} \frac{K_a}{\sin\beta_2} \frac{d_i}{d_m} . \qquad (2.19)$$

As was the case for the radial seal, the clearance loss coefficient K_a for the axial rotor seal depends on the already referred to rotor inclination $2\Delta h_s''/w_2^2$ and can be taken from Figure 2.7.

In analogy to an eccentric rotor position, a local tangential force can be formed that depends on the clearance loss, $\zeta_{sp,a}$ and the isentropic tangential force U_s (equation (2.12)). Integration along the perimeter yields the transverse forces acting on the rotor,

$$\left.\begin{aligned} Q_{4s} &= 0, \\ Q_{3s} &= \frac{1}{2}\, U_s \frac{a}{l''} \frac{K_a}{\sin\beta_2} \frac{d_l}{d_m}. \end{aligned}\right\} \qquad (2.20)$$

/16

In accordance with its definition in the deflection matrix, the force Q_{3s} has a destabilizing effect on the rotor. It depends linearly on relative deflection a/l'' and on the isentropic tangential force, and it can be represented by the coefficient K_{3s}, as the slope of the dimensionless exciting force, over the relative deflection.

$$\frac{Q_{3s}}{U_s} = K_{3s} \frac{a}{l''}, \qquad (2.21)$$

$$K_{3s} = \frac{1}{2} \frac{K_a}{\sin\beta_2} \frac{d_l}{d_m}. \qquad (2.22)$$

The exciting force due to the inclination of the rotor disc can be calculated only for a purely axial seal effect, with the clearance loss equations given. However, it would be on the safe side to consider this effect, in addition to the clearance excitation coefficient for a radial seal. For a clearance that shows both a radial and an axial seal effect, in a rotor position as shown in Figure 2.5, due to the inclination a non-uniform clearance loss will occur along the perimeter. For this reason the inlet turbine stages will be subject to greater excitation forces, because of the inclination.

2.3.2 Forces due to the pressure distribution at the sealing clearance

Trutnowsky [15] provides a comprehensive review of the calculations for non-contact seals. While most of the procedures described there determine only the throughput of a clearance that is uniform along the entire perimeter, we are interested here primarily in the effects by means of which transverse forces act on the rotor due to clearance flow.

For an eccentric position of the rotor with respect to the housing, not only the throughput but also the pressure gradient along the direction of flow changes with the local clearance width. Assuming that at the exit the flow will be subject to atmospheric pressure, a characteristic pressure distribution /17
will develop along the perimeter, whose maximum value will coincide with the narrowest clearance. This effect was first described by Lomakin [17] using a smooth clearance with purely axial flow. A similar derivation can be found in [18]. Because of the assumption of a purely axial flow without compensation at the perimeter, the pressure drop is linear. If we apply this to the shroud band of a turbine rotor, as in Figure 2.8, below, we

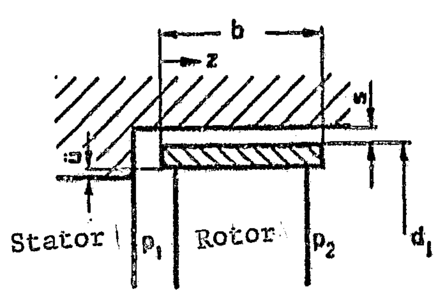

Figure 2.8 Rotor clearance

obtain - for the system of coordinates of Figure 2.5 - the pressure variation $p(z, \psi)$ in axial and tangential direction

$$\frac{p(z,\varphi) - p_2}{p_1 - p_2} = \frac{1 - \frac{z}{b}}{1 + 2\,\frac{s - e\cos\varphi}{b\lambda}} . \qquad (2.23)$$

The friction coefficient λ from pipe hydraulics is assumed constant, here. In addition, entrance losses and a possible pressure recovery at the exit have been neglected.

The integration of a variable pressure variation yields, first, the forces acting on the rotor in general,

$$\left.\begin{aligned} Q_{1D} &= -\int_0^b\int_0^{2\pi} dP\cos\varphi = -\int_0^b\int_0^{2\pi} p(z,\varphi)\cos\varphi\; r\, d\varphi\, dz ,\\ Q_{2D} &= -\int_0^b\int_0^{2\pi} dP\sin\varphi = -\int_0^b\int_0^{2\pi} p(z,\varphi)\sin\varphi\; r\, d\varphi\, dz . \end{aligned}\right\} \qquad (2.24)$$

/18

Using equation (2.23), we obtain the forces

$$\left.\begin{aligned} Q_{1D} &= -(p_1 - p_2)\,\frac{\pi}{8}\left(\frac{b}{s}\right)^2 \frac{\lambda}{\left(1 + \frac{\lambda b}{2s}\right)^2}\, d_i\, e ,\\ Q_{2D} &= 0 . \end{aligned}\right\} \qquad (2.25)$$

The force Q_{1D}, because of its negative sign, acts against the deflection e and at larger pressure differences $p_1 - p_2$ - as they occur, for instance, with boiler feed pumps - have an essential effect on the system's vibration behavior. Because of a simplified integration of the pressure variation, this force depends linearly on the eccentricity, while the dimensions of clearance d_1, b and s occur in some non-linear terms. Since the pressure variation is symmetrical with respect to the deviation,, the force Q_{2D}, perpendicular to it vanishes.

Due to the shaft's rotation, a tangential velocity is generated at the clearance, which in gas bearings, for instance - thoroughly investigated by Stingelin [27] - generates a pressure maximum ahead of the narrowest clearance. Here, too, Q_{2D} forces are developed that could initiate a vibrational system. However, they become important only for sufficiently long clearances with a very small radial clearance width, which in general can no longer be implemented in the blade channel of a turbomachine.

In turbine stages a large velocity component in a tangential direction occurs especially ahead of the rotor's seal clearance, with the consequence that the clearance flow is no longer axial but develops a diagonal flow. With eccentric rotor positioning this leads to variable cross-sections along a stream tube. A problem that can be adapted to ours was treated by Kiesewetter and Wolter [19], who calculated transverse forces acting on a conical piston with longitudinal flow against it, as in Figure 2.9:

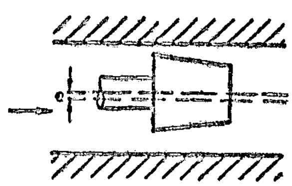

Figure 2.9 Conical piston with longitudinal flow

With the flow as shown, forces act in the deflection direction that can cause hydraulic lock in valves, for instance.

If we apply the basic geometrical relations from [19] to a /19
cylinder eccentrically placed with respect to the housing, with a diagonal flow against it, then the lowest flow will occur already before the narrowest clearance (ψ = 0), causing a pressure maximum according to the qualitative representation in

Figure 2.10 (b), below.

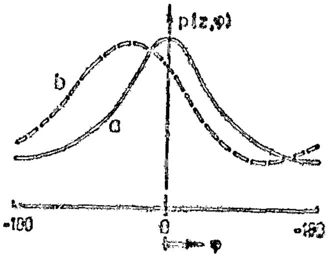

Figure 2.10 Qualitative pressure variation
a: Purely axial flow
b: Flow affected by torsional forces

Integration of this pressure distribution along the perimeter yields, besides the restoring force, also an exciting force. Similar considerations for the flow affected by torsional forces and for purely axial flow can also be transferred to the labyrinth seals regularly used in turbines, if one assumes that the pressure drop caused by the seal peaks depend on the local radial clearance width (cf. also section 3.3.1).

Kostyuk [21], however, starts from the premise that at a seal peak the kinetic energy is completely turbulent. Without the effect of an arriving torsional flow, under this assumption there are no transverse forces to act on the rotor, if it is displaced with regard to the housing in a direction parallel to the axis. If the shaft is inclined with respect to the housing, vibration-causing forces are generated, due to the non-uniform clearance width in the flow direction. Assuming a spiral flow pattern through the clearance, which could be caused either by shaft rotation or an incoming rotational flow, Rosenberg [28] studied a labyrinth seal with two peaks.

He obtained the pressure distribution (b) in Figure 2.10, which agreed well with his own measurements. But since here the flow line pattern is fixed, only qualitative statements may be made about the effect of torsional flow.

According to Alford [20], for a labyrinth seal in which the entrance clearance width is smaller than that at the exit, transverse forces develop due to the displacement effect of the vibrating rotor, which can excite the system to self-generated vibration. While Alford admits no compensating flow in the labyrinth chambers, under these conditions, Spurk and Keiper [21] obtain the opposite result by taking this effect into consideration.

Hochreuther [29] performed a fundamental study on clearance flow, which starts by solving the describing differential equation at a plain clearance, using a difference method. Under the effects of rotation, boundary conditions can be satisfied for both laminar and turbulent flow, according to Lomakin. The procedure was then widened to include labyrinth clearances; here, complete turbulence of the kinetic energy was assumed at the seal peaks.

2.3.3. Processes at the meridian channel and the clearance entrance

If the clearance width is variable along the perimeter, the local throughput will vary, as will the tangential efficiency at the rotor blades of a turbine stage. This was taken into consideration in equation (2.7), in section 2.3.1. For constant pressure blading without shroud band, Piltz [12] investigated both effects, by determining pressure changes in the blades, in addition to changes in the local triangle of velocities. Here - at least for blading without shroud band - pressure-caused forces can act on the rotor. With an occasionally severe simplification of the three-dimensional flow, Piltz calculated all the coefficients for the deflection and velocity matrices in equation (2.3). However, he showed by means of vibration /21
calculations that at least for a central rotor arrangement between the bearings, the additional effects determined by him

are small, in comparison to considering only the excitation force Q_2 according to [1].

If we start from the premise that despite local velocity variations the percentage reaction is constant along the periphery, even for an eccentric rotor position, then - in contrast to [12] - by introducing empirical clearance loss coefficients, all effects that can cause local variations of the peripheral force have been taken into consideration. Disregarding balancing flows, this is valid especially also for an efficiency distribution measured as a function of the clearance width, which was used to calculate local clearance losses.

At constant pressure ahead of and behind the turbine step, a variation in the percent reaction along the periphery - according to section 4.4.1. - caused by the local clearance loss, is conceivable. Here the turbine stage percent reaction is calculated from the pressure gradient and the turbine's throughput. The only quantity variable along the periphery to be considered here is the stator's clearance throughput according to equation (4.13). It turns out that it can very substantially affect the result, if one disregards balancing flows ahead of the stator. Thus, for a large local stator clearance, a larger pressure gradient should be observed at the rotor. This would displace the local stator to rotor clearance loss ratio, which could affect the forces from the variable tangential or peripheral force to very differing degrees. The pressure distribution in the sealing clearances could be affected also. However, a variable percent reaction in the blading's flow channel does not necessarily have to cause compressive forces, since varying pressure distributions could cancel each other, in the case of banded "bucket"-channels.

Since the effect of a percent reaction varying along the periphery is not yet sufficiently established theoretically, nor documented by measurements, we shall have to neglect it, at present. It can in addition be assumed that pressure differences in the meridian channel will cancel out much more readily due to compensating flows in tangential direction, than in radial /22 sealing clearances, since the relative eccentricity - referred to channel height - will be smaller. Only in extreme cases, with high tangential velocities in the meridian channel, compressive forces will be exerted on long, cylindrical rotor parts, such as those observed during flow control in test turbines [5] with standing blading (i.e., large flow-off velocities).

The influx conditions at the clearance entrance are of great importance to the development of a pressure distribution in a radial clearance. La Roche [23] investigated the effect of a point of irregularity in the side-wall of the bladed flow channel, between the stator and the rotor, both theoretically and experimentally. To begin with, he showed that the off-set height $\underline{\ddot{u}}$ (see Figure 2.8) is of substantial significance to the initial pressure at the clearance and hence also to its throughput.

The calculations and basic experimentation were performed by La Roche for a bidimensional model in which the flow was perpendicular to the off-set. Apparently an optimum off-set height could be found, here, for which the losses would be minimized. In contrast to the usual construction, it was characterized by a negative value for the off-set and a well-rounded entrance edge. However, transfer to an off-set with an oblique influx still appears to be somewhat of a problem, even though La Roche obtained good agreement with the bidimensional model, with a uniform-pressure turbine.

Since the overlapping $\underline{\ddot{u}}$ of the rotor "bucket" height, as compared to the stator blading, varies as the local radial clearance width, for an eccentric rotor position, La Roche's equations should be included in the calculations of local clearance losses. It turns out, however, that this loss is very strongly dependent on secondary effects (displacement effect of the rotor blades, wall boundary layer at the stator, form of the shroud band edge), which make a reliable application impossible. While the off-set certainly has an effect, for the above reasons La Roche's results can not be applied to this study.

3 CALCULATION PROCEDURE FOR THE TRANSVERSE FORCES AT TURBINE GRIDS, CAUSED BY THE CLEARANCE FLOW

By introducing the appropriate control surfaces, it is possible to represent a seal clearance of arbitrary geometry as a series of contiguous stream tubes with variable cross-sections. If we consider average velocities, at certain reference points in the clearance, then they can be described by the continuity equation, as a function of the local cross-section. The throughput and the pressure drop along a stream tube can be calculated by means of the energy equation, using empirical loss coefficients; the flow directions are determined with the aid of the theorem of momentum, under special consideration for the torsional effect at the entrance. The application of energy and momentum equations to such stream tubes thus does not require a knowledge of the processes inside the flow domain under consideration. It does, however, assume loss coefficients, to be determined from known empirical laws.

From this view, the separation of clearance flow from the flow along the meridian channel must be possible; this will occur only if the blade ends are fitted with shroud bands or similar features. Free-standing "buckets" or blades, coupled to the loss of volume, also show losses at the blade ends, caused by the energy exchange between the clearance flow and the main flow. For this reason, such constructions shall be precluded, here. For the same reasons we must establish restrictions for blading with discontinuous shroud bands, or for stator bottoms with balance holes, since the continuity equation of a stream tube can not be applied in the manner described, due to a pressure equalizing flow.

In the calculation method below, we study the clearance flow for a stationary displacement of the rotor with respect to the housing, which would allow the determination of all the coefficients for the deviation matrix (2.3). However, because of their much greater significance to the vibration behavior, we shall only determine here the forces relevant to an eccentric rotor position. Since the ratio of the clearance flow to the main flow in the meridian channel is always small, we shall consider the latter independent of the rotor's eccentricity, as a first approximation. In addition, the calculation method shall be limited to cases in which the clearance flow may be considered incompressible. /24

3.1. Definition of the control spaces at the seal clearance

The non-contact seals predominantly used for turbines are shown

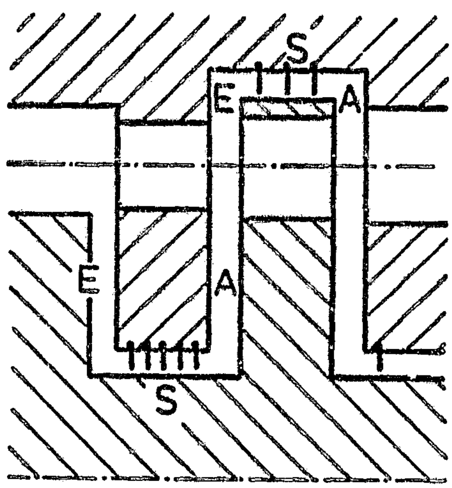

Figure 3.1 Seal clearance at a turbine step

in Figure 3.1, above. For reasons of operating safety the clearance at the radial entrance E and exit A is usually much larger than the radial clearnce S, which in the newer machines is fashioned in labyrinth form.

Some constructions show a plain clearance at the rotor, in which case the sealing effect can also be accomplished by an entrance edge (E). We shall consider, as a general case, the rotor clearance in Figure 3.1, where either a plain or a labyrinth clearance can be used at section S. However, the calculation procedure chosen will also be applicable to the seal clearance at the stator, if the corresponding radii are used. By /25 appropriate modifications to the boundary conditions, it is readily possible to eliminate the radial entrance or exit, which allows for other areas of application, such as shaft seals of the housing.

The flow processes at a seal clearance may be considered unidimensional, provided the control spaces can be varied according to the course of the flow lines. These are described by support reference points which in the entrance and exit lie on constant radii; in the radial clearance they lie on planes perpendicular to the axis of rotation. In the tangential direction the support points are variable and are determined by the local angle of the flow-line tangent to the reference line. The variable cross-sections of a stream tube are then given by the distances between neighboring support points on the perimeter and by the local clearance width. In this procedure, the flow angles are obtained by iteration of the basic equations for a stream tube; they are assumed known, in the following sections.

3.1.1. Location of the support points

The clearance is divided into j stream tubes in the peripheral direction, as shown in Figure 3.2, below, where the selection of their reference points is arbitrary, since the stream tube's width is also defined, thereby. While for certain calculation cases it may be appropriate to arrange the support points locally closer to the perimeter, here we have established a uniform subdivision on the radius r_E of the entrance. The support points located on this radius have the subscript E_1, being characterized by the subscript k in the periphral direction. With the constant step width

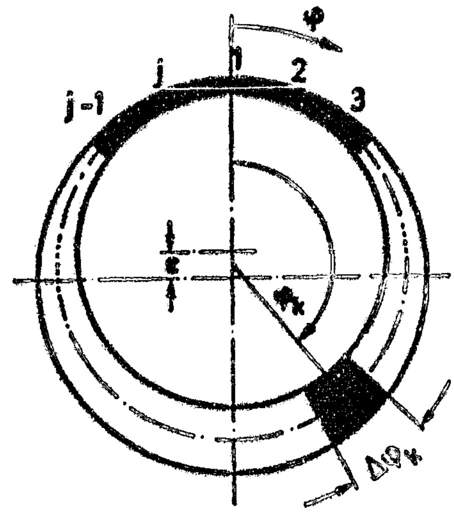

Figure 3.2 Stream tube subdivision along the periphery

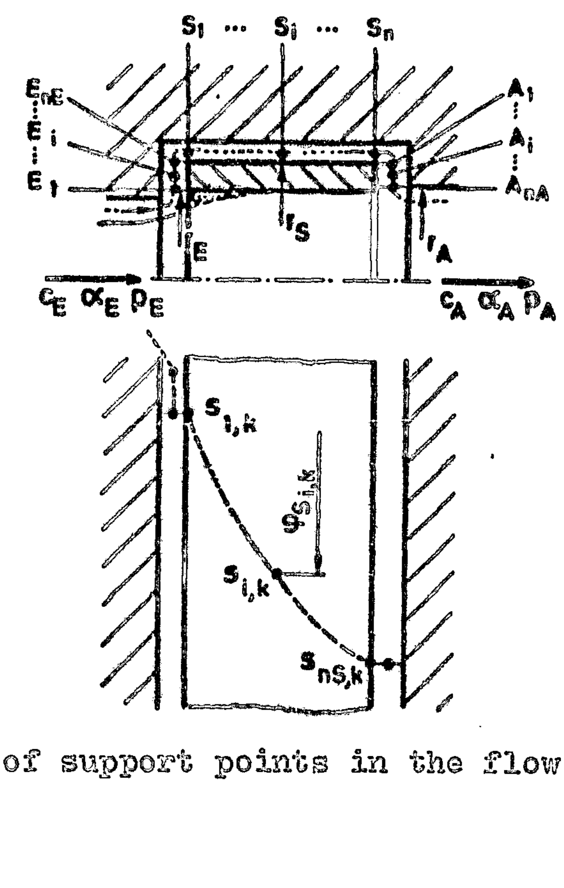

Figure 3.3 Location of support points in the flow direction

$$\Delta\varphi_{E_{1,k}} = \frac{2\pi}{j}, \quad (k = 1, \ldots j)$$

the support points at the entrance are determined by the angle at the center,

$$\varphi_{E_{1,1}} = 0,$$
$$\varphi_{E_{1,k}} = \varphi_{E_{1,k-1}} + \Delta\varphi_{E_{1,k}}, \; (k = 2, \ldots j).$$

/27

Starting with these support point locations the remaining points in the flow direction are determined using only the local flow angles. For this reason, together with the angle at the center, ψ, in the flow direction the corresponding distances, $\Delta\psi$ - more precisely determined in section 3.1.2. - also change.

The clearance (E, S and A) is divided respectively into nE, nS and nA support points, in the flow direction, as shown in Figure 3.3, above, characterized by the subscript i. Using the peripheral angle ψ as an example, the complete indexing is shown for the radial clearance S. We have left it out whenever there is no possibility of confusion. If we require the support points to lie on a flow line, the tangents to the flow lines are given together with the corresponding flow angles. These can be approximated by straight line segments, if appropriate assumptions are made regarding the intersection of two consecutive tangents.

If we subdivide the radial entrance E of radius r_E to r_S into nE support points, as in Figure 3.4, below, then at constant step width,

$$\Delta r_E = \frac{1}{2} \frac{|r_S - r_E|}{nE - 1}$$

/28

the radii

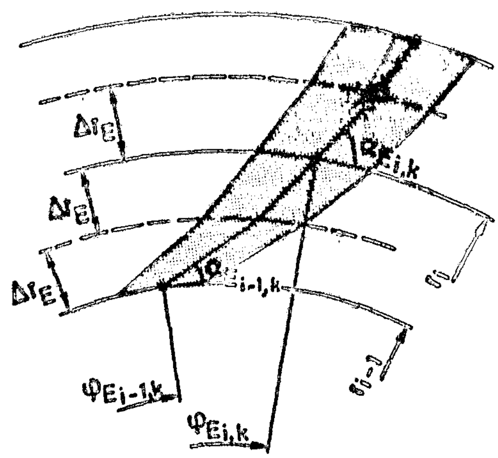

Figure 3.4 Support point location at radial entrance

$$r_{E_1} \hat{=} r_E ,$$
$$r_{E_i} = r_{E_{i-1}} + 2\,\Delta r_E \,\mathrm{sign}\,(r_S - r_E) \,, \quad (i = 2, \dots nE)$$

are fixed. With known flow angles α_E, the location of the support points is then determined by the peripheral angles

$$\varphi_{E_{i,k}} = \varphi_{E_{i-1,k}} + \frac{\Delta r_E}{r_{E_{i-1}}}\,\mathrm{ctg}\,\alpha_{E_{i-1,k}} + \frac{\Delta r_E}{r_{E_i}}\,\mathrm{ctg}\,\alpha_{E_{i,k}} \,, \qquad (3.2)$$
$$(i = 2, \dots nE)\;(k = 1, \dots j)$$

For the angular composition shown in Figure 3.4, this equation is valid only as an approximation, assuming small step width, Δr.

In radial clearances, according to Figure 3.5, below, the same quations are used for plain clearances. However, in order to obtain a better comparison with measurements, a variable subdivision of the support points was chosen. If the peripheral angles remain unchanged as the flow moves around the corners, then we have, for all support points <u>k</u> at the beginning of the radial clearance

$$\varphi_{S_{1,k}} = \varphi_{E_{nE,k}}$$

and further on, /29

$$\varphi_{S_{i,k}} = \varphi_{S_{i-1,k}} + \frac{\Delta z_{i-1}}{r_S} \operatorname{ctg} \alpha_{S_{i-1,k}} + \frac{\Delta z_i}{r_S} \operatorname{ctg} \alpha_{S_{i,k}} \cdot \qquad (3.3)$$

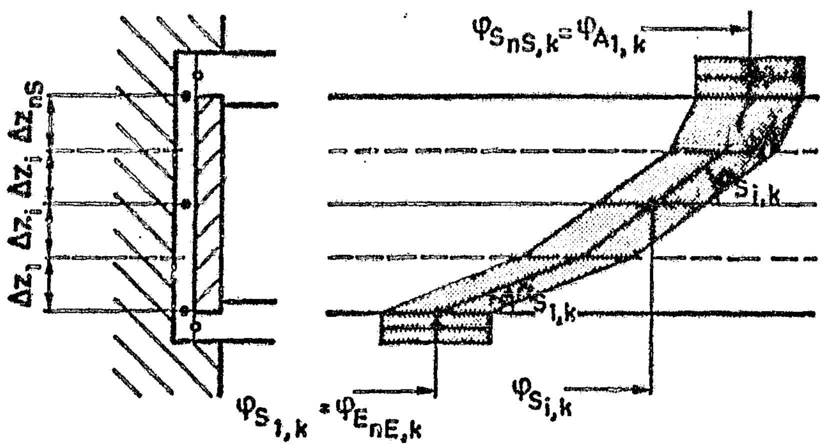

Figure 3.5 Location of support points for a smooth radial clearance

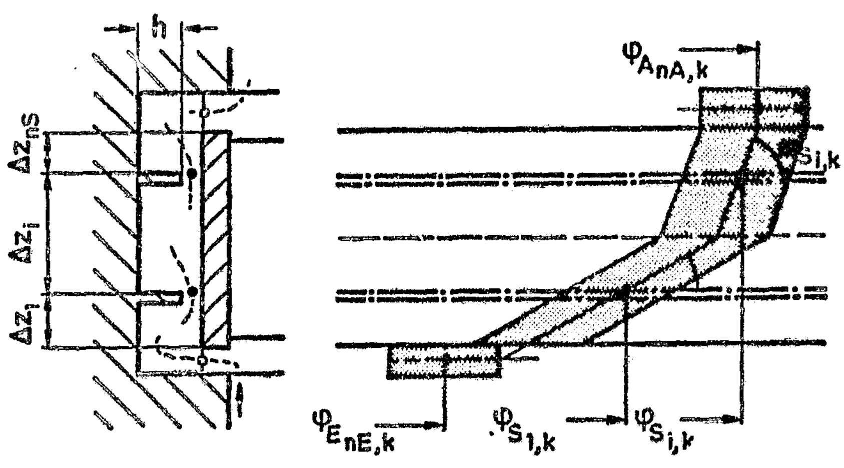

Figure 3.6 Location of support points for a labyrinth clearance

For a labyrinth, support points can be defined only immediately at the peak, since no useful assumptions regarding a velocity distribution can be made in the chambers. Because of this fact, the relationship between the support point location and the flow angles at the peak acquire particular significance. Starting with the last point $E_{nE,k}$ of the entrance, it is assumed, according to Figure 3.6, above, that the flow in the first chamber becomes turbulent, following a path at the perimeter of the labyrinth chamber that is proportional to the height h of the chamber and to the flow angles at the end of the radial entrance.

$$\varphi_{S_{1,k}} = \varphi_{E_{nE,k}} + \frac{h}{r_S} \operatorname{ctg} \alpha_{E_{nE,k}} + \frac{\Delta z_1}{r_S} \operatorname{ctg} \alpha_{S_{1,k}} .$$

/30

According to this, as in the case of the smooth clearance, the flow line is composed of straight line segments, where the point of intersection of the flow lines can be changed by means of the the weighting factor $0 < g_z < 1$, which in Figure 3.6 is drawn for $g_z = 0.5$.

$$\varphi_{S_{i,k}} = \varphi_{S_{i-1,k}} + \frac{\Delta z_i}{r_S} \left[(1 - g_z) \operatorname{ctg} \alpha_{S_{i-1,k}} + g_z \operatorname{ctg} \alpha_{S_{i,k}} \right] . \quad (3.4)$$

In the radial exit, the peripheral angles can be calculated in the same manner as in the entrance. If a smooth radial clearance precedes the exit, than as a first approximation there will be no change in the peripheral angle at the corner to the exit

$$\varphi_{A_{1,k}} = \varphi_{S_{nS,k}} ,$$

while in a labyrinth the width of the last chamber must still be taken into consideration:

$$\varphi_{A_{1,k}} = \varphi_{S_{nS,k}} + \frac{\Delta z_{nS}}{r_S} \operatorname{ctg} \alpha_{S_{nS,k}} .$$

For the remaining peripheral angles we shall have, in analogy to Figure 3.4

$$\varphi_{A_{i,k}} = \varphi_{A_{i-1,k}} + \frac{\Delta r_A}{r_{A_{i-1}}} \mathrm{ctg}\, \alpha_{A_{i-1,k}} + \frac{\Delta r_A}{r_{A_i}} \mathrm{ctg}\, \alpha_{A_{i,k}} . \qquad (3.5)$$

Thus, the path followed by the fluid from the clearance entrance to its exit is determined only by local flow angles and the distances to the reference lines. Obviously, complicated clearance forms can also be studied in this manner, provided an adequate relationship can be found between the flow angles at the support points and the peripheral angles. More precise predictions - especially in the case of labyrinth seals - can be made only when it becomes possible to obtain empirical information from flow lines rendered visible.

3.1.2. Calculation of the control surfaces /31

In order to determine the local flow cross-sections, some assumptions have to be made regarding the corresponding width of the stream tube, $r\Delta\psi$. If, in agreement with Figure 3.7, below,

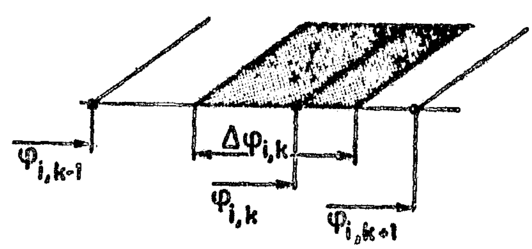

Figure 3.7 Determination of channel width

we place the lateral limit of the control space between two support points, then we shall have, taking into consideration the definition of the peripheral angle as shown in Figure 3.2

$$\begin{aligned}
\Delta\varphi_{i,1} &= \tfrac{1}{2}\left(\varphi_{i,2} - \varphi_{i,j} + 2\pi\right), \\
\Delta\varphi_{i,k} &= \tfrac{1}{2}\left(\varphi_{i,k+1} - \varphi_{i,k-1}\right), \qquad (k = 2,\dots j-1) \qquad (3.6) \\
\Delta\varphi_{i,j} &= \tfrac{1}{2}\left(\varphi_{i,1} + 2\pi - \varphi_{i,j-1}\right).
\end{aligned}$$

Assuming a rotor displacement with regard to the housing parallel to the axis, according to Figure 3.1 the local clearance widths remain constant in the radial entrance s_E and exit s_A, while the radial clearance is dependent on both the peripheral angle ψ and the eccentricity, e. To reduce the formal structure, we desisted at this point from also including an inclination of the rotor with respect to the housing. Because of the bending line of the vibrating turbine shaft, the inclinations in the domain of the steps are small, in any event. For this reason we may neglect the effect, at this point.

The local radial clearance width according to Figure 3.2 can be satisfactorily approximated by

$$\tilde{s} = s - e\cos\varphi$$

/32

where it is assumed that at a support point $\psi_{i,k}$ that width will correspond to the average value of $\Delta\psi_{i,k}$. For a sufficiently narrow subdivision at the perimeter, this approximation has no effect on the final result, in comparison to an exact integration. Thus we have, for the local surfaces of all stream tubes,

$$\left.\begin{aligned}
A_{E_{i,k}} &= \mu_{E_{i,k}}\, r_{E_i}\, \Delta\varphi_{E_{i,k}}\, s_E\,, \\
A_{S_{i,k}} &= \mu_{S_{i,k}}\, r_S\, \Delta\varphi_{S_{i,k}} \left(s - e\cos\varphi_{S_{i,k}}\right), \\
A_{A_{i,k}} &= \mu_{A_{i,k}}\, r_{A_i}\, \Delta\varphi_{A_{i,k}}\, s_A\,.
\end{aligned}\right\} \qquad (3.7)$$

The contraction coefficients μ introduced here make it possible to take into consideration cross-section constrictions that occur due to dead water or stream contractions at the peaks. For plain clearances and turbulent flow with μ = 1, we shall begin by assuming that the reference cross-section is completely filled by the stream; for labyrinth seals, Neumann's [24] measured values can be used. At constant seal peak width Δ, the effective flow cross-section decreases with increasing radial clearance width s, as shown in Figure 3.8.

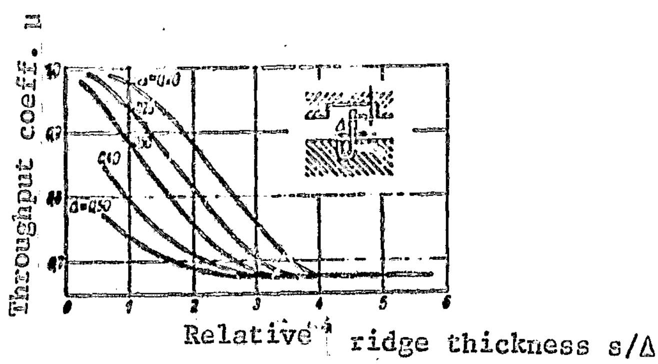

Figure 3.8 Contraction coefficients (from [24])

According to it, taking the stream contraction into account, a clearance that is variable along the perimeter becomes somewhat more uniform. It remains to be established, however, whether this contraction coefficient is irrestrictedly applicable also to a seal peak with a diagonal flow through it.

3.2 Basic stream tube equations /33

An essential advantage of the decomposition into individual stream tubes is that the basic equations of fluid flow mechanics can be satisfied unidimensionally for every control space.

This makes it possible to apply loss coefficients from the labyrinth theory, as well as the laws of tube hydraulics. In principle, one could also calculate compressibly along the stream tube, using procedures already known [15]. However, the context of this study assumes incompressible fluids, which seems particularly permissible, considering the relatively low pressure drop and Mach numbers $Ma < 0.5$ at the clearances considered, especially that of the rotor.

3.2.1. Boundary conditions at clearance entry and exit

The pressures and velocities caused in the blade stream must be known immediately at the clearance entrance and exit. Starting from these conditions, the throughput of each stream tube will result from the losses in the clearance. Once the average cross-section calculations have been performed for a turbine step (cf. section 4.4.1.), it can be generally assumed that the flow will obey the potential vortex law. Through it we obtain, from a tangential component c_{um} at velocity c_m at a radius r_m, the tangential component c_u at radius $\underline{r}$:

$$c_u r = c_{u_m} r_m \quad .$$

If we further assume that the axial velocity $c \sin \alpha$ is constant along the radius, then we have

$$c \sin \alpha = c_m \sin \alpha_m \quad .$$

Let the density be uniform throughout the channel; we can then apply the energy equation

$$\frac{1}{2} c^2 + \frac{p}{\rho} = \frac{1}{2} c_m^2 + \frac{p_m}{\rho}$$

/34

It is thus possible to calculate the velocity $\underline{c}$, the pressure $\underline{p}$ and the angle of flow α at a radius $\underline{r}$.

$$\left.\begin{aligned} c^2 &= c_m^2 \left[\left(\frac{r_m}{r} \cos \alpha_m \right)^2 + \sin^2 \alpha_m \right], \\ p &= p_m + \frac{\rho}{2} c_m^2 \left[1 - \left(\frac{c}{c_m} \right)^2 \right], \\ \alpha &= \arcsin \left(\frac{c_m}{c} \sin \alpha_m \right). \end{aligned} \right\} \qquad (3.8)$$

As a first approximation this yields the pressures and velocities before the clearance, at the radii r_E of the entrance and r_A of the exit.

We may now assume that at the clearance entrance, according to Figure 3.3, a flow line exists that separates the mass stream flowing through the stream tube from the main flow. Thereby the clearance throughput is no longer determined only by the static pressure drop, but also by the energy of the incoming velocities, whose impulse determined the flow direction inside the clearance. By the same token, shearing forces due to mixed friction at the separating flow line could act on the clearance flow, which can be neglected here, however, in comparison to the incoming impulse. The effect of an overlapping in La Roche's sense (cf. section 2.3.3.) shall be neglected, at this point. But it could be described generally by means of the loss coefficients to be introduced later.

At the exit, the clearance flow becomes mixed with the meridian channel flow; here, because of the differences in velocity, mixed friction forces from the main flow will act on the clearance's stream tubes. It is conceivable that during this process part of the kinetic energy of either the clearance flow or main flow is converted into pressure. However, according to the transverse pressure equation of flow mechanics (cf. [16]), it can be assumed - for most seal constructions - that the exiting clearance flow will be subject to the static pressure behind the clearance.

The processes described above for the clearance entrance and exit are expressed below in energy and impulse equations. To this end we must first introduce formal coefficients for the pressure loss and incoming impulse, whose magnitude will be examined more closely only in section 3.3. /35

3.2.2. Continuity equation

For each support point $\underline{i}$ the continuity equation can be satisfied with the throughput of stream tube $\underline{k}$. It may be assumed that in the cross-section, perpendicularly to the flow direction $A_{i,k} \sin\alpha_{i,k}$ there is an average velocity, since in equation (3.7) we already introduced contraction coefficients $\mu_{i,k}$ that take into account a variable velocity distribution within the effective flow cross-section. Therefore the velocities

$$w_{i,k} = \frac{\dot{m}_k}{\varrho A_{i,k} \sin\alpha_{i,k}} \qquad (3.9)$$

can be calculated for all support points in the clearances E, S and A, from the throughput $\dot{m}_k$ of the stream tube and at constant density.

3.2.3. Energy equation

In each stream tube, the energy equations can be set up from one support point to the next. According to section 3.2. we must distinguish here between three basic types of control spaces, which are summarized in Figure 3.9, below. The pressure losses caused by friction against the channel walls or by velocity vortexing can be assumed to be proportional to the kinetic energy of the flow, with a loss coefficient ζ,

$$p_v = \frac{\rho}{2} w_m^2 \zeta. \qquad (3.10)$$

/36

Depending on the definition in the energy equation, this pressure loss can occur ahead of or behind the reference point at which the average velocity is w_m.

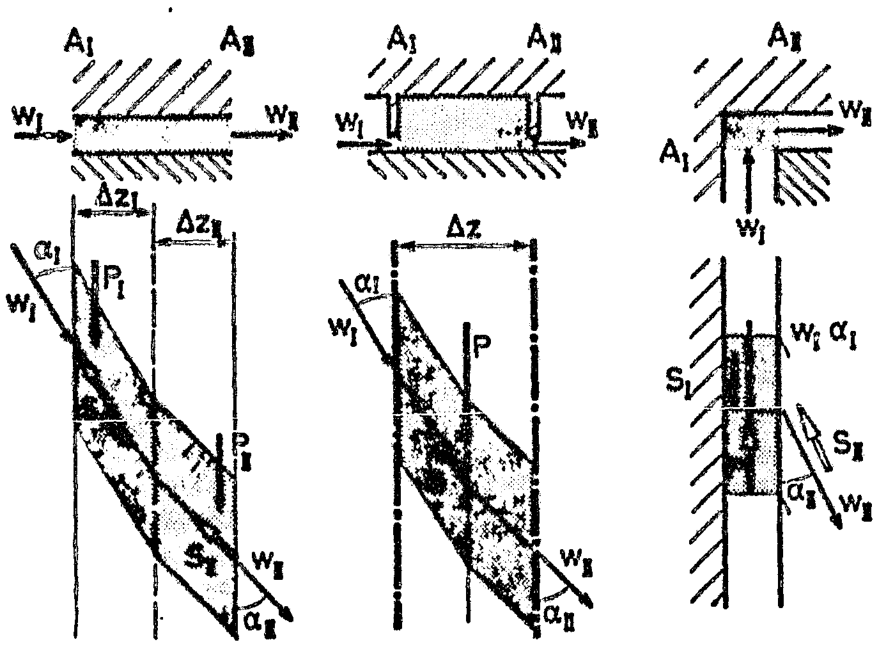

Figure 3.9 Control spaces in a stream tube

The control spaces were selected such that the velocities at locations I and II could be determined with the continuity equation, from the local surfaces and flow angles. The total pressure loss occurring in the control space is composed of two portions, proportional to the kinetic energy of the entrance and exit velocity. Hence the energy equation is

$$\frac{p_I}{\rho} + \frac{1}{2} w_I^2 (1 - \zeta_I) = \frac{p_{II}}{\rho} + \frac{1}{2} w_{II}^2 (1 + \zeta_{II})$$

/37

The loss coefficients ζ depend essentially on the local clearance form and the length of the stream tube under consideration. They are discussed in more detail in section 3.3. For a plain radial clearance, according to Figure 3.5, two neighboring control spaces will have loss coefficients of the same magnitude ahead and behind a support point, because the flow paths are of equal length due to the composition of the flow line. Hence we have

$$\zeta_{II\,i} = \zeta_{I\,i+1}\,, \qquad (i = 1, \dots, n-1). \qquad (3.12)$$

This equation can also be used as an approximation for the clearance in the radial entrance and exit, as in Figure 3.4. In a labyrinth, the loss coefficient ζ_I in energy equation (3.11) describes the portion of kinetic energy that is conserved due to incomplete vortexing. ζ_{II} describes the entrance loss caused by the flow towards the peak. However, since losses are smaller during flow acceleration than they are for flow retardation, in a labyrinth we can generally set $\zeta_{II} = 0$.

With a diagonal or transverse flow around a corner, as in Figure 3.8, the determination of the loss coefficients is particularly problematic. Here we can define coefficients ζ^z and ζ^ψ for the pressure losses, caused by the normal, or respectively, the tangential velocity components. The energy equation then becomes

$$\frac{p_I}{\rho} + \frac{1}{2} w_I^2 \left[\sin^2\alpha_I \left(1 - \zeta_I^z\right) + \cos^2\alpha_I \left(1 - \zeta_I^\psi\right) \right] \qquad (3.13)$$

$$= \frac{p_{II}}{\rho} + \frac{1}{2} w_{II}^2 \left[\sin^2\alpha_{II} \left(1 + \zeta_{II}^z\right) + \cos^2\alpha_{II} \left(1 + \zeta_{II}^\psi\right) \right].$$

The above description makes a simpler estimate of the pressure loss at a corner possible; for $\zeta^z = \zeta^\psi$ we obtain the same relationship of equation (3.11), in which the entire pressure loss in the control room is divided into inflow and outflow velocity components.

With the general energy equations (3.11) and 3.13) we can describe the pressure drop (see Table 3.1, below) along the /38

TABLE 3.1 Energy equations for the stream tube

$p_E - p_{E_1} = \frac{1}{2}\frac{\dot m^2}{\varrho}\frac{1}{A_{E_1}^2}\left[(1+\zeta_{WE}^z) + (1+\zeta_{WE}^\varphi)\,\mathrm{ctg}^2\alpha_{E_1}\right] - \frac{\varrho}{2} c_E^2\left[\sin^2\alpha_E\,(1-\zeta_{CE}^z) + \cos^2\alpha_E\,(1-\zeta_{CE}^\varphi)\right]$	$E - E_1$
$p_{E_i} - p_{E_{i+1}} = \frac{1}{2}\frac{\dot m^2}{\varrho}\left\{\frac{1}{A^2_{E_{i+1}}}(1+\zeta_{E_{i+1}})(1+\mathrm{ctg}^2\alpha_{E_{i+1}}) - \frac{1}{A^2_{E_i}}(1-\zeta_{E_i})(1+\mathrm{ctg}^2\alpha_{E_i})\right\}$	$E_i = 1, \ldots nE-1$
$p_{E_{nE}} - p_{S_1} = \frac{1}{2}\frac{\dot m^2}{\varrho}\left\{\frac{1}{A^2_{S_1}}\left[(1+\zeta^z_{SE}) + (1+\zeta^\varphi_{SE})\,\mathrm{ctg}^2\alpha_{S_1}\right] - \frac{1}{A^2_{E_{nE}}}\left[(1-\zeta^z_{ES}) + (1-\zeta^\varphi_{ES})\,\mathrm{ctg}^2\alpha_{E_{nE}}\right]\right\}$	$E_{nE} - S_1$
$p_{S_i} - p_{S_{i+1}} = \frac{1}{2}\frac{\dot m^2}{\varrho}\left\{\frac{1}{A^2_{S_{i+1}}}(1-f_L\,\zeta_{S_{i+1}})(1+\mathrm{ctg}^2\alpha_{S_{i+1}}) - \frac{1}{A^2_{S_i}}(1-\zeta_{S_i})(1+\mathrm{ctg}^2\alpha_{S_i})\right\}$	$S_i = 1, \ldots nS-1$
$p_{S_{nS}} - p_{A_1} = \frac{1}{2}\frac{\dot m^2}{\varrho}\left\{\frac{1}{A^2_{A_1}}\left[(1+\zeta^z_{AS}) + (1+\zeta^\varphi_{AS})\,\mathrm{ctg}^2\alpha_{A_1}\right] - \frac{1}{A^2_{S_{nS}}}\left[(1-\zeta^z_{SA}) + (1-\zeta^\varphi_{SA})\,\mathrm{ctg}^2\alpha_{S_{nS}}\right]\right\}$	$S_{nS} - A_1$
$p_{A_i} - p_{A_{i+1}} = \frac{1}{2}\frac{\dot m^2}{\varrho}\left\{\frac{1}{A^2_{A_{i+1}}}(1+\zeta_{A_{i+1}})(1+\mathrm{ctg}^2\alpha_{A_{i+1}}) - \frac{1}{A^2_{A_i}}(1-\zeta_{A_i})(1+\mathrm{ctg}^2\alpha_{A_i})\right\}$	$A_i = 1, \ldots nA-1$
$p_{A_{nA}} - p_A = \frac{\varrho}{2} c_A^2\left[\sin^2\alpha_A\,(1-\zeta^z_{CA}) + \cos^2\alpha_A\,(1-\zeta^\varphi_{CA})\right] - \frac{1}{2}\frac{\dot m^2}{\varrho}\left\{\frac{1}{A^2_{A_{nA}}}\left[(1-\zeta^z_{WA}) + (1-\zeta^\varphi_{WA})\,\mathrm{ctg}^2\alpha_{A_{nA}}\right]\right\}$	$A_{nA} - A$

entire seal clearance, in accordance with Figure 3.3. Eliminating the velocities by means of the continuity equation (3.9), we obtain the pressure differences between neighboring support points as a function of the stream tube's throughput, the local flow cross-sections and angles, and the empirically determined pressure loss coefficients. For the angles we introduced the transformation

$$\frac{1}{\sin^2\alpha} = 1 + \mathrm{ctg}^2\alpha$$

we shall need later. The relationships of the loss coefficients for smooth clearances in accordance with equation (3.12) is also taken into consideration. Introducing the control magnitude

$$\left.\begin{array}{lll} f_L = 1 & & \text{Plain clearance} \\ f_L = 0 & & \text{Labyrinth } (\zeta_{II}=0) \end{array}\right\} \qquad (3.14)$$

the equations given can be applied also to a labyrinth with a loss-free afflux to the seal peak. In general the loss coefficients contain the subscript of the support point under consideration; a complete compilation is presented in Table 3.5.

By addition of all the energy equations in Table 3.1, we obtain a single equation that allows us to determine the throughput of a stream tube as a function of the total pressure differential available, provided the areas, angles and loss coefficients are known. Since the kinetic energy (velocity energy) of the tangential components before and after the clearance have no effect on the throughput (cf. section 3.2.6.), we define the total pressure loss without that portion:

$$\Delta p_B = p_E - p_A + \frac{\varrho}{2} c_E^2 \sin^2\alpha_E \left(1 - \zeta_{cE}^{z}\right) - \frac{\varrho}{2} c_A^2 \sin^2\alpha_A \left(1 - \zeta_{cA}^{z}\right). \qquad (3.15)$$

/40

The throughput equation then is of the form

$$\Delta p_B = -\frac{\varrho}{2} c_E^2 \cos^2\alpha_E \left(1-\zeta_{cE}^{\varphi}\right) + \frac{\varrho}{2} c_A^2 \cos^2\alpha_A \left(1-\zeta_{cA}^{\varphi}\right) + \frac{1}{2}\frac{\dot{m}^2}{\varrho}\sum_{x}^{n}\frac{1}{A_x^2}\zeta_x \left(1+\mathrm{ctg}^2\alpha_x\right) . \qquad (3.16)$$

However, since the angles are also a function of the throughput - as we shall see in the following section - some special considerations (see section 3.2.5.) must still be applied to these calculations. Accordingly, Table 3.1 provides the entire pressure distribution through all support points i,k in the seal clearance.

3.2.4. Momentum equation

The change in a momentum entering and leaving a control surface is equal to the sum of all external forces acting on the control space. If the momentum change is to be calculated in this manner, the external forces have to be sufficiently known. On a control space as shown in Figure 3.9 there act - disregarding gravitational and centrifugal forces - compressive forces at the limits as well as supporting forces due to friction against channel walls. Applying the momentum theorem perpendicularly to the entrance and exit surfaces is unfavorable for the control space selected, since it requires knowledge of the pressures acting on the end planes A_I and A_{II}, from the energy equation. If the momentum theorem is applied in the tangential direction, then these compressive forces are eliminated. Then only the much smaller forces acting on the lateral limits of the stream tube must be determined by iteration from a pressure distribution along the perimeter.

If we take into consideration variable radii at the entrance and exit of a control space, as in Figure 3.9, then the momentum equilibrium for the forces acting at the support point is

/41

$$\dot{m}\left[r_I w_I \cos\alpha_I - r_{II} w_{II} \cos\alpha_{II}\right] + r_I P_I + r_{II} P_{II} - r_I S_I \cos\alpha_I - r_{II} S_{II} \cos\alpha_{II} = 0. \quad (3.17)$$

The first term contains the changes in torsional forces from entrance I to exit II, where the differing radii have an effect only in clearances with a radial flow direction. The next term refers to the compressive and supporting forces effective at the control space surfaces, which due to wall friction or kinetic energy vortexing act against the flow direction, in a first approximation. For the momentum equation above it must be assumed that no moments are exerted on the control space due to the forces acting on it, which is plausible if we take into consideration the impulse forces normal to the peripheral direction.

From considerations based on a imple control space, it can be reasoned that frictional forces as well as those that balance the flow during vortexing, must be proportional to the throughput and the velocity defined as reference velocity in the energy equation. Thus, by means of coefficients $\bar{\zeta}$ we can in general encompass the support forces

$$S = \dot{m}\, w_m \bar{\xi} \quad (3.18)$$

that are active due to wall friction. The magnitude of these impulse loss coefficients $\bar{\zeta}$ is determined in section 3.3 in connection with the pressure loss coefficients ζ.

The compressive forces P acting on the control space are determined from clearance geometry and the pressure distribution. Hence, the calculation of the compressive forces is possible only when the pressure distribution in all stream tubes has been determined. The variation of the pressure along the perimeter can be represented at locations $\underline{i}$ by means of the Fourier series /42

$$\begin{aligned} p_i(\varphi) = {} & a_0 + a_1 \cos\varphi + a_2 \cos 2\varphi + \dots + a_m \cos m\varphi \\ & + b_1 \sin\varphi + b_2 \sin 2\varphi + \dots + b_m \sin m\varphi \,. \end{aligned} \qquad (3.19)$$

From $\underline{j}$ known pressures $p_{i,k}$ in a support plane $\underline{i}$ and the corresponding peripheral angles $\psi_{i,k}$, a maximum of $m = (j/2)-1$ coefficients can be determined for the function $p_i(\psi)$, for instance by a least squares fit method. However, since due to their iterative determination (section 3.5.) the pressures are not given exactly, a curve-fitting with fewer coefficients can lead to better convergence of the calculation procedure, especially for labyrinths.

According to Figure 3.10, the resulting tangential compressive

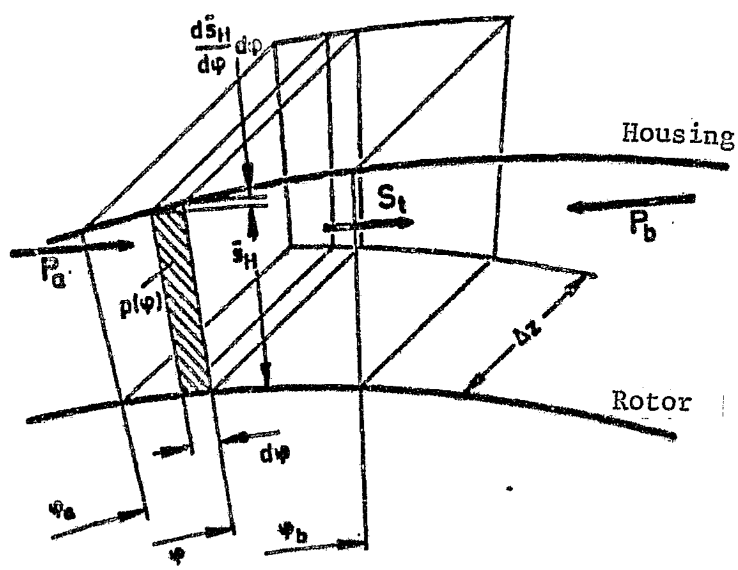

Figure 3.10 Compressive forces acting on the control space

force P is composed of the forces P_a and P_b, acting from both sides on the free portions of the stream tube. To this must be added the supporting force S_t, exerted on the fluid as a consequence of the channel curvature. For a simple calculation of these forces it is assumed that the pressure distribution and the variable clearance width of a support plane $\underline{i}$ are constant over the width Δz_i. For a smooth clearance, it is possible to attain an exact solution with sufficiently narrow spacing of the support points in the flow direction; for a labyrinth, instead, because of the unknown pressure distribution inside the chamber, no more precise considerations are possible. With a variable clearance width

$$\tilde{s}_H = h + s - e \cos\varphi$$

which takes into consideration the height of the labyrinth chamber, the individual forces can be determined across the width Δz.

$$\left.\begin{aligned} P_a &= \Delta z \ \tilde{s}_H(\varphi_a)\, p(\varphi_a)\,, \\ P_b &= \Delta z \ \tilde{s}_H(\varphi_b)\, p(\varphi_b)\,, \\ S_t &= \Delta z \int_{\varphi_a}^{\varphi_b} \frac{d\tilde{s}_H}{d\varphi}\, p(\varphi)\, d\varphi = \Delta z \; e \int_{\varphi_a}^{\varphi_b} p(\varphi) \sin\varphi \, d\varphi\,. \end{aligned}\right\} \quad (3.20)$$

/43

By introducing the coefficients a_m and b_m of the pressure distribution (3.19), these forces can be calculated within the prescribed interval ψ_a to ψ_b in the control space. The determined integrals occurring for the support force S_t are of the form

$$\int_{\varphi_a}^{\varphi_b} a_x \cos x\varphi \sin\varphi \, d\varphi ,$$

$$\int_{\varphi_a}^{\varphi_b} b_x \sin x\varphi \sin\varphi \, d\varphi .$$

Their solution is generally possible, with the usually tabulated formulae, for any number of coefficients and shall be assumed known, here. The resulting tangential compressive force acting on the control space now is /44

$$P_{i,k} = \Delta z_i \Big\{ (h+s) \left[p(\varphi_a) - p(\varphi_b) \right] - e \left[\cos\varphi_a \, p(\varphi_a) - \cos\varphi_b \, p(\varphi_b) \right] + e \int_{\varphi_a}^{\varphi_b} p(\varphi) \sin\varphi \, d\varphi \Big\}_{i,k} . \qquad (3.21)$$

It can be shown that if we assume $p(\psi)$ = constant, the resulting compressive force vanishes. In a labyrinth the effect of the compressive forces increases with increasing chamber height and for variable radial clearance widths is dependent on the local gradient $ds/d\psi$. However, the sum of all the compressive forces along the perimeter must be zero. For the radial entrance E and exit A the calculation performed above for the compressive forces acting on the free portion of the control space is much simpler, since the supportive forces S_t (3.20) vanish, because of the constant clearance width.

Once all external forces in the impulse moment equation (3.18) have been calculated, that equation can be used to calculate the flow angles at a support point II, if that angle is known for the immediately preceding support point I. Since at the entrance the flow angle is given by the main flow in the meridian channel, in conformance to Figure 3.3, the angles at all other support points can be calculated. Using continuity equation (3.9), we obtain the system of equations of Table 3.2 for the angular changes along the stream tube k. The impulse loss coefficients $\bar{\zeta}$ are indexed here in a manner similar to that of

TABLE 3.2 Stream tube impulse equations

$\operatorname{ctg}\alpha_{E1} = \frac{\varrho}{\dot{m}} A_{E1} c_E \cos\alpha_E \frac{1-\bar{\zeta}_{CE}}{1+\bar{\zeta}_{WE}}$	E_1
$\operatorname{ctg}\alpha_{E\,i+1} = \frac{A_{E\,i+1}\, r_{E\,i}}{A_{E\,i}\, r_{E\,i+1}} \frac{1-\bar{\zeta}_{E\,i}}{1+\bar{\zeta}_{E\,i+1}} \operatorname{ctg}\alpha_{E\,i} + \frac{\varrho}{\dot{m}^2} \frac{A_{E\,i+1}}{1+\bar{\zeta}_{E\,i+1}} \left(P_{E\,i} \frac{r_{E\,i}}{r_{E\,i+1}} + P_{E\,i+1}\right)$	$E_{i=1,\dots n_E-1}$
$\operatorname{ctg}\alpha_{S1} = \frac{A_{S1}}{A_{E\,n_E}} \frac{1-\bar{\zeta}_{ES}}{1+\bar{\zeta}_{SE}} \operatorname{ctg}\alpha_{E\,n_E} + \frac{\varrho}{\dot{m}^2} \frac{A_{S1}}{1+\bar{\zeta}_{SE}} P_{SE}$	S_1
$\operatorname{ctg}\alpha_{S\,i+1} = \frac{A_{S\,i+1}}{A_{S\,i}} \frac{1-\bar{\zeta}_{S\,i}}{1+f_L\bar{\zeta}_{S\,i+1}} \operatorname{ctg}\alpha_{S\,i} + \frac{\varrho}{\dot{m}^2} \frac{A_{S\,i+1}}{1+f_L\bar{\zeta}_{S\,i+1}} \left(P_{S\,i} + f_L P_{S\,i+1}\right)$	$S_{i=1,\dots n_S-1}$
$\operatorname{ctg}\alpha_{A1} = \frac{A_{A1}}{A_{S\,n_S}} \frac{1-\bar{\zeta}_{SA}}{1+\bar{\zeta}_{AS}} \operatorname{ctg}\alpha_{S\,n_S} + \frac{\varrho}{\dot{m}^2} \frac{A_{A1}}{1+\bar{\zeta}_{AS}} P_{SA}$	A_1
$\operatorname{ctg}\alpha_{A\,i+1} = \frac{A_{A\,i+1}\, r_{A\,i}}{A_{A\,i}\, r_{A\,i+1}} \frac{1-\bar{\zeta}_{A\,i}}{1+\bar{\zeta}_{A\,i+1}} \operatorname{ctg}\alpha_{A\,i} + \frac{\varrho}{\dot{m}^2} \frac{A_{A\,i+1}}{1+\bar{\zeta}_{A\,i+1}} \left(P_{A\,i} \frac{r_{A\,i}}{r_{A\,i+1}} + P_{A\,i+1}\right)$	$A_{i=1,\dots n_A-1}$
$\operatorname{ctg}\bar{\alpha}_{A\,n_A} = \operatorname{ctg}\alpha_{A\,n_A} + \frac{\varrho}{\dot{m}^2} A_{A\,n_A} R_{MA}$	A_{n_A}

Table 3.2 and contain the conditions (3.12) and (3.14). Since the entrance angle depends on the throughput of a stream tube, this relationship remains applicable to all further angles. At the clearance exit, the flow angle of the last support location increases, due to the mixed friction force R_{MA}, whose magnitude is determined in section 3.3.4. in connection with the loss coefficients.

It can be inferred directly from the momentum equations that /46
for a reduction of the cross-sectional areas A, from one support point to the next, the flow angle must increase. Because of friction or vortexing, $\overline{\zeta} > 0$, of the velocity energy a reduction in the torsional force is obtained also for constant surfaces.

3.2.5. Throughput calculation

The flow angles in Table 3.2 can be represented, for any arbitrary support point, as a function of the stream tube throughput, in the form

$$\mathrm{ctg}\,\alpha_{i,k} = A_{i,k}\left[\cdot\frac{\varrho}{\dot{m}_{t}}\, c_E \cos\alpha_E\, b_{i,k} + \frac{\varrho}{\dot{m}_{t}}\, c_{i,k}\right]. \qquad (3.22)$$

Here, the coefficients b indicate the angular changes due to the support forces, while the coefficients c reflect the effect of external compressive forces. Based on the impulse equations in Table 3.2, these coefficients were calculated for all the support points in a stream tube, as shown in Table 3.3.

If equation (3.22) is replaced in the energy equation in Table 3.1, an equation is obtained for the calculation of the throughput, that in comparison to equation (3.16) contains a combination of the coefficients mentioned above, instead of the angle α:

TABLE 3.3 Coefficients for flow angle calculations from (3.22)

$b_{E1} = \frac{1-\bar{\zeta}_{CE}}{1+\bar{\zeta}_{WE}}$	$c_{E1} = 0$
$b_{Ei+1} = \frac{r_{Ei}}{r_{Ei+1}} \frac{1-\bar{\zeta}_{Ei}}{1+\bar{\zeta}_{Ei+1}} b_{Ei}$	$c_{Ei+1} = c_{Ei} \frac{b_{Ei+1}}{b_{Ei}} + \frac{1}{1+\bar{\zeta}_{Ei+1}} \left(P_{Ei} \frac{r_{Ei}}{r_{Ei+1}} + P_{Ei+1} \right)$
$b_{S1} = \frac{1-\bar{\zeta}_{ES}}{1+\bar{\zeta}_{SE}} b_{EnE}$	$c_{S1} = c_{EnE} \frac{b_{S1}}{b_{EnE}} + \frac{1}{1+\bar{\zeta}_{SE}} P_{SE}$
$b_{Si+1} = \frac{1-\bar{\zeta}_{Si}}{1+f_L \bar{\zeta}_{Si+1}} b_{Si}$	$c_{Si+1} = c_{Si} \frac{b_{Si+1}}{b_{Si}} + \frac{1}{1+f_L \bar{\zeta}_{Si+1}} \left(P_{Si} + f_L P_{Si+1} \right)$
$b_{A1} = \frac{1-\bar{\zeta}_{SA}}{1+\bar{\zeta}_{AS}} b_{SnS}$	$c_{A1} = c_{SnS} \frac{b_{A1}}{b_{SnS}} + \frac{1}{1+\bar{\zeta}_{AS}} P_{AS}$
$b_{Ai+1} = \frac{r_{Ai}}{r_{Ai+1}} \frac{1-\bar{\zeta}_{Ai}}{1+\bar{\zeta}_{Ai+1}} b_{Ai}$	$c_{Ai+1} = c_{Ai} \frac{b_{Ai+1}}{b_{Ai}} + \frac{1}{1+\bar{\zeta}_{Ai+1}} \left(P_{Ai} \frac{r_{Ai}}{r_{Ai+1}} + P_{Ai+1} \right)$
–	$\bar{c}_{AnA} = c_{AnA} + R_{MA}$

$$\Delta p_B = \frac{1}{2} \frac{\dot{m}^2}{\rho} S_g + \frac{\rho}{2} c_E^2 \cos^2\alpha_E \left[S_b - (1-\zeta_{CE}^{\varphi}) \right] + \frac{\rho}{2} \left[\frac{c_E \cos\alpha_E}{\dot{m}} S_{bc} + \frac{1}{\dot{m}^2} S_c \right] + \frac{\rho}{2} c_A^2 \cos^2\alpha_A (1-\zeta_{CA}^{\psi}) . \quad (3.23)$$

The sums S are constructed very similarly to each other and can be simply represented using the format in Table 3.4

TABLE 3.4 Sums to calculate throughput with equation (3.23) /48

$S_g = \frac{\zeta_{WE}^{z}}{A_{E1}^2} + \sum_{i=1}^{nE-1}\left(\frac{\zeta_{Ei}}{A_{Ei}^2} + \frac{\zeta_{Ei+1}}{A_{Ei+1}^2}\right) + \frac{\zeta_{ES}^{z}}{A_{EnE}^2} + \frac{\zeta_{SE}^{z}}{A_{S1}^2} + \sum_{i=1}^{nS-1}\left(\frac{\zeta_{Si}}{A_{Si}^2} + f_L\frac{\zeta_{Si+1}}{A_{Si+1}^2}\right) + \frac{\zeta_{SA}^{z}}{A_{SnS}^2} + \frac{\zeta_{AS}^{z}}{A_{A1}^2} + \sum_{i=1}^{nA-1}\left(\frac{\zeta_{Ai}}{A_{Ai}^2} + \frac{\zeta_{Ai+1}}{A_{Ai+1}^2}\right) + \frac{\zeta_{WA}^{z}}{A_{AnA}^2}$
$S_b \mathrel{\hat{=}} S_y$ with: $y_{Ei} = b_{Ei}^2 \quad y_{Si} = b_{Si}^2 \quad y_{Ai} = b_{Ai}^2$
$S_{bc} \mathrel{\hat{=}} S_y$ with: $y_{Ei} = 2 b_{Ei} c_{Ei} \quad y_{Si} = 2 b_{Si} c_{Si} \quad y_{Ai} = 2 b_{Ai} c_{Ai}$
$S_c \mathrel{\hat{=}} S_y$ with: $y_{Ei} = c_{Ei}^2 \quad y_{Si} = c_{Si}^2 \quad y_{Ai} = c_{Ai}^2$
$S_y = \zeta_{WE}^{\varphi} y_{E1} + \sum_{i=1}^{nE-1}\left(\zeta_{Ei} y_{Ei} + \zeta_{Ei+1} y_{Ei+1}\right) + \zeta_{ES}^{\varphi} y_{EnE} + \zeta_{SE}^{\varphi} y_{S1} + \sum_{i=1}^{nS-1}\left(\zeta_{Si} y_{Si} + f_L \zeta_{Si+1} y_{Si+1}\right) + \zeta_{SA}^{\varphi} y_{SnS} + \zeta_{AS}^{\varphi} y_{A1} + \sum_{i=1}^{nA-1}\left(\zeta_{Ai} y_{Ai} + \zeta_{Ai+1} y_{Ai+1}\right) + \zeta_{WA}^{\varphi} y_{AnA}$

By combining the energy and momentum equations, the throughput is now given by a single equation, readily solved by iteration. It is possible in principle, however, to first calculate the angles from Table 3.2 and then the throughput using equation /49

(3.16). Of course, in that case the calculations required increase considerably, depending on the magnitude of the torsional forces at the entrance. However, the underlying assumption in throughput calculations according to the above equation is a knowledge of the local flow cross-sections and loss coefficients, which can be obtained by iteration from the course of the flow lines.

3.2.6. Discussion of the basic equations using a simple clearance shape

A dimensionless description of the basic equations for a stream tube is possible only if the boundary conditions ahead of and behind the clearance are eliminated, while retaining the effect of the seal geometry. Since as will be shown later, the loss coefficients introduced depend on the local flow angle and Reynold's number, a complete similarity can not be attained for different initial pressures and velocities.

The total pressure differential from equation (3.15) is chosen as the reference magnitude, which besides the static pressure difference contains only the axial components of the velocities ahead of and behind the clearance. To describe the torsional forces, the dynamic pressure of the tangential component of the corresponding velocity is related to this total pressure differential:

$$\zeta_E^* = \frac{\frac{\varrho}{2} c_E^2 \cos^2 \alpha_E}{\Delta p_B} , \qquad (3.24)$$

$$\zeta_A^* = \frac{\frac{\varrho}{2} c_A^2 \cos^2 \alpha_A}{\Delta p_B} . \qquad (3.25)$$

While the magnitudes included above are independent of the clearance form, a reference surface must be defined for the throughput

$$A_B = 2\pi\, r_B\, s_B . \qquad (3.26)$$

/50

For a central rotor position, let s_B be the smallest clearance width at a radius r_B. From the pressure drop Δp_B we can now determine a throughput,

$$\dot{m}_B = A_B \sqrt{2\varrho\, \Delta p_B}\,, \qquad (3.27)$$

which corresponds to a maximum value, if we start from the premise that only the velocity energy at the smallest cross-section A_B is completely turbulent. We thus obtain a reference magnitude to judge the quality of the seal. On the other hand, with the introduction of the reference area mentioned, we can plot the variable throughput $\dot{m}_k$ of the stream pipe, as a function of the seal clearance's perimeter. To obtain a simple description of a stream tube's basic equations, we shall neglect here the compressive forces at the surfaces of the control space, which appears permissible at least for smooth clearances (cf. section 3.6). If we furthermore consider a flow not affected by mixed friction forces at the exit, then in equation (3.23) the sums S_b and S_{bc} are eliminated. With the reference magnitudes introduced earlier, we now have for the throughput

$$\frac{\dot{m}_k}{\dot{m}_B} = \sqrt{\frac{1 + C_E^* \left[(1-\zeta_{CE}^{\varphi}) - S_b\right] - C_A^* (1-\zeta_{CA}^{\varphi})}{S_g\, A_B^2}} \qquad (3.28)$$

Since the sums S_g and S_b in Table 3.4 are quite large, we shall show the essential relationships with the example of a labyrinth with n sealing peaks and without radial entrance or exit. Here we need consider only the coefficients ζ_{CE} and $\overline{\zeta}_{CE}$ of the velocity ahead of the clearance, as well as the pressure loss and impulse loss coefficients ζ, or respectively, $\bar{\zeta}$, at the peaks. We thus have the following conditions:

$$n_E = 0, \qquad n_A = 0,$$
$$A_{E_1} = A_{S_1} \mathrel{\hat=} A_1, \qquad A_{A_{nA}} = A_{S_{nS}} \mathrel{\hat=} A_n,$$
$$\zeta^{\alpha}_{WE} = \zeta^{\varphi}_{WE} = \bar{\zeta}_{WE} = 0, \qquad \zeta^{\alpha}_{WA} = \zeta^{\varphi}_{WA} \mathrel{\hat=} \zeta_n, \quad \bar{\zeta}_{WA} \mathrel{\hat=} \bar{\zeta}_n,$$
$$\zeta^{\alpha}_{CA} = \zeta^{\varphi}_{CA} = 1.$$

/51

For the coefficients of Table 3.3 we now have

$$b_{S_1} = (1 - \bar{\zeta}_{CE}),$$
$$b_{S_{i+1}} = (1 - \bar{\zeta}_{CE}) \prod_{\nu=1}^{i} (1 - \bar{\zeta}_\nu), \qquad (i = 2, \dots, n).$$

From this we obtain the sums of Table 3.4,

$$S_g = \sum_{i=1}^{n} \frac{\zeta_i}{A_i^2},$$
$$S_b = (1 - \bar{\zeta}_{CE})^2 \sum_{i=1}^{n} \left(\zeta_i \prod_{\nu=1}^{i-1} (1 - \bar{\zeta}_\nu)^2 \right),$$

where for i = 1 the product above takes the value

$$\prod_{\nu=1}^{0} (1 - \bar{\zeta}_\nu)^2 = 1$$

If we take the dependence on the peripheral angle into account, described by the subscript of the stream tube k, then we have, using equation (3.28), the referred throughput

$$\frac{\dot{m}_k}{\dot{m}_B} = \sqrt{\frac{1 + C_E^* \left\{ (1 - \zeta^{\varphi}_{CE}) - (1 - \bar{\zeta}_{CE})^2 \sum_{i=1}^{n} \left(\zeta_{i,k} \prod_{\nu=1}^{i-1} (1 - \bar{\zeta}_{\nu,k})^2 \right) \right\}}{\sum_{i=1}^{n} \left(\zeta_{i,k} \frac{A_B^2}{A_{i,k}^2} \right)}} \qquad (3.29)$$

The structure of the equation is maintained even if we take into consideration all the loss coefficients defined in the previous sections for more general clearance forms. In this case, just the sum-terms in the numerator and the denominator will become larger.

If for a central rotor position we assume equally sized flow cross-sections at all peaks, then the throughput - for complete vortexing of the velocity energy - will be proportional to $1/\sqrt{n}$ in the known manner, where n is the number of seal peaks. /52
Assuming equal total pressure differentials, a decrease in throughput could occur due to an afflux affected by torsional forces, if the expression in the rounded bracket of equation (3.29) becomes less than zero. For this, the relationship between the coefficients ζ and $\overline{\zeta}$ - which will be discussed in more detail in section 3.3.2. - is of primary importance.

The local flow angles can be determined, in the example chosen, at an arbitrary support point $1 > x \geq n$ in stream tube k, from Table 3.2

$$\operatorname{ctg} \alpha_{x,k} = c_E \cos \alpha_E \frac{\rho}{\dot{m}_k} A_{x,k} \left(1 - \zeta_{cE}\right) \prod_{\nu=1}^{x-1} \left(1 - \overline{\zeta}_{\nu,k}\right) . \qquad (3.30)$$

In a similar manner it is possible to calculate local pressures in the clearance from the differences for location x,k in Table 3.1

$$p_{x,k} = p_A + \frac{1}{2} \frac{\dot{m}_k^2}{\rho} \left\{ \sum_{i=x}^{n} \left(\zeta_i \frac{1 + \operatorname{ctg}^2 \alpha_i}{A_i^2} \right) - \frac{1 + \operatorname{ctg}^2 \alpha_x}{A_x^2} \right\}_k . \qquad (3.31)$$

With the throughput (3.29) and the flow angles above it is now possible to describe the pressure distribution only in terms of loss coefficients and the local surfaces. As a special case, and as shall be shown yet (cf. equation (3.49)), we can assume a dependence of the momentum loss coefficients $\bar{\zeta}$ on the pressure loss coefficients ζ, of the form

$$(1-\bar{\zeta}_i)^2 = 1-\zeta_i \qquad \text{and} \qquad (1-\bar{\zeta}_{CE})^2 = 1-\zeta_{CE}^{\varphi}$$

In this manner the throughput would be independent of the magnitude of the relative afflux energy C_E^x, and we obtain, from equation (3.29),

$$\frac{\dot{m}_k}{\dot{m}_B} = \frac{1}{\sqrt{\sum_{i=1}^{n}\left(\zeta_{i,k}\frac{A_B^2}{A_{i,k}^2}\right)}} \qquad (3.32)$$

/53

Under these assumptions, the flow angles calculated above (3.30) can be described very simply as a function of the face areas A of the control spaces and the loss coefficients, for a location $\underline{x}$

$$\mathrm{ctg}^2\alpha_{x,k} = C_E^* A_{x,k}^2 (1-\zeta_{CE}^{\varphi}) \prod_{\nu=1}^{x-1}(1-\zeta_{\nu,k}) \cdot \sum_{i=1}^{n}\frac{\zeta_{i,k}}{A_{i,k}^2} . \qquad (3.33)$$

According to this equation, for equal surfaces, with increasing torsional effects at the entrance and larger pressure loss coefficients, there will be smaller flow angles in the clearance. Along the clearance ($x > 1$), however, with complete vortexing ($\zeta = 1$) a purely axial flow will be achieved, with $\mathrm{ctg}\,\alpha = 0$. Pressure at the support points can be rendered in a dimensionless manner with equations (3.31) to (3.33)

$$\frac{p_{x,k} - p_A}{\Delta p_B} = \frac{-\frac{1}{A^2_{x,k}} + \sum_{i=x}^{n} \frac{\zeta_{i,k}}{A^2_{i,k}}}{\sum_{i=1}^{n} \frac{\zeta_{i,k}}{A^2_{i,k}}} \quad (3.34)$$

Here the effect of torsional influx can no longer be directly recognized, since now it is limited to changes in the local surfaces (3.7), which depending on the course of the flow lines (3.3) are a function of the angles (3.33). It can be shown, however, that for stream pipes with decreasing cross-sections there is a pressure increase, compared to those in which the cross-sections increase in the flow direction. If, for an eccentrically positioned rotor, we start from the premise that the flow through the clearance proceeds in the same direction anywhere along the perimeter, then there will be a higher pressure ahead of the narrowest clearance than behind it, due to the surface ratios. For the rest, equation (3.34) applies to any clearance form, provided the local flow cross-sections and loss coefficients are known. This equation is hence particularly well suited to qualitative studies unaffected by a balancing flow (cf. section 2.3.2.)

If one assumes that the flow through the clearance is purely axial, then for equal radial clearance widths, the cross-sections along a stream tube become constant, and we /54
obtain the pressure distribution

$$\frac{p_{x,k} - p_A}{\Delta p_B} = \frac{-1 + \sum_{i=x}^{n} \zeta_{i,k}}{\sum_{i=1}^{n} \zeta_{i,k}} . \quad (3.35)$$

For constant vortexing coefficients ζ, there hence will be no pressure differences along the perimeter even for eccentric rotor positions. However, if the pressure loss coefficient is inversely proportional to the clearance width - as in the plain clearance - then a pressure maximum will occur at the narrowest clearance, as in Lomakin's case (cf. section 2.3.2.). Further pressure distribution tendencies in a seal clearance with afflux affected by torsional forces can be derived from the sample calculation in section 3.6.

3.3. Coefficients to describe flow processes within the clearance

Table 3.5 is a compilation of all the coefficients introduced to describe the clearance flow. The first column lists the pressure

TABLE 3.5 Characterization of loss coefficients

Pressure loss coeff.		Impulse loss coeff.	Refer. veloc. geschwindigkeit	Location Bild 3 3
ζ^{z}_{CE}	ζ^{φ}_{CE}	$\bar{\zeta}_{CE}$	c_E	Entrance
ζ^{z}_{WE}	ζ^{φ}_{WE}	$\bar{\zeta}_{WE}$	$w_{E\,1}$	
$\zeta_{E\,i}$		$\bar{\zeta}_{E\,i}$	$w_{E\,i}$	Radial entrance
ζ^{z}_{ES}	ζ^{φ}_{ES}	$\bar{\zeta}_{ES}$	$w_{E\,nE}$	1st bend
ζ^{z}_{SE}	ζ^{φ}_{SE}	$\bar{\zeta}_{SE}$	$w_{S\,1}$	
$\zeta_{S\,i}$		$\bar{\zeta}_{S\,i}$	$w_{S\,i}$	Radial clearance
ζ^{z}_{SA}	ζ^{φ}_{SA}	$\bar{\zeta}_{SA}$	$w_{S\,nS}$	2nd bend
ζ^{z}_{AS}	ζ^{φ}_{AS}	$\bar{\zeta}_{AS}$	$w_{A\,1}$	
$\zeta_{A\,i}$		$\bar{\zeta}_{A\,i}$	$w_{A\,i}$	radial exit
ζ^{z}_{WA}	ζ^{φ}_{WA}	$\bar{\zeta}_{WA}$	$w_{A\,nA}$	Exit
ζ^{z}_{CA}	ζ^{φ}_{CA}	R_{MA}	c_A	

loss coefficients, while the second displays the magnitudes responsible for angular changes according to the momentum theorem. From the corresponding reference velocities it is possible to readily recognize the significance of the individual subscripts, in conjunction with the location designations shown in Figure 3.3.

Below we shall determine the pressure loss coefficients ζ along the stream tube with equations from the literature, while the momentum loss coefficients $\bar{\zeta}$ can be determined only by means of analogy considerations. Since the relation between these two magnitudes is very essential to the throughput of the stream tube, an additional condition at the clearance entrance must be satisfied, which establishes the relation between the incoming velocity energy and the entrance momentum (cf. section 3.3.2.3.)

/56

3.3.1 Pressure loss coefficients

3.3.1.1. Plain clearance

The loss coefficient ζ, already introduced for the energy equation (cf. equation 3.10), can be determined - in the case of a plain clearance - according to the laws of hydraulics: from the length $\underline{l}$, the htdraulic diameter d_{hydr} and the tube's friction coefficient λ. According to [16], the hydraulic diameter

$$d_{hydr} = \frac{4A}{U_{ben}} = 2s$$

is defined as the ratio of four times the flow cross-section to the wetted perimeter, and corresponds here to twice the clearance width. The tube's friction coefficient depends on the tube wall roughness and on Reynold's number

$$Re = \frac{w\,2s}{\nu}$$

For hydraulically smooth walls, measured values as those in Figure 3.11 (cf. Truckenbrodt [16]) can be used. At the seal

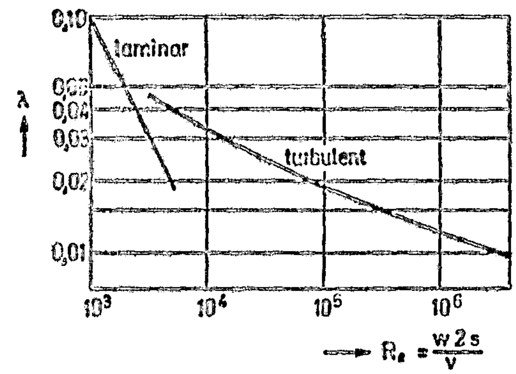

Figure 3.11 Tube friction coefficients for hydraulically smooth walls

clearances in turbine stators, we shall assume here, without restrictions, the calculation procedure for turbulent /57
flow. Thus we have, for the friction coefficient in von Karman's form

$$\frac{1}{\sqrt{\lambda}} = 2{,}0 \; \lg\left(Re\sqrt{\lambda}\right) - 1{,}0 \; . \qquad (3.36)$$

Since the flow lines in the clearance can be represented sectionally by straight lines, the flow paths l can be represented (see Figure 3.12, below) as a function of the flow angle and the distance a to the reference line. We then obtain, for the loss coefficients in the case of plain clearances

$$\zeta_{i,k} = \lambda(Re) \frac{a}{2\,\bar{s}\,\sin\alpha_{i,k}} \; ,$$

Entrance: $\bar{s} \hat{=} s_E$; $a \hat{=} \Delta r_E$

Radial clearance: $\bar{s} \hat{=} s - e \cos\varphi_{Si,k}$; $a \hat{=} \Delta z_i$

Exit: $\bar{s} \hat{=} s_A$; $a \hat{=} \Delta r_A$

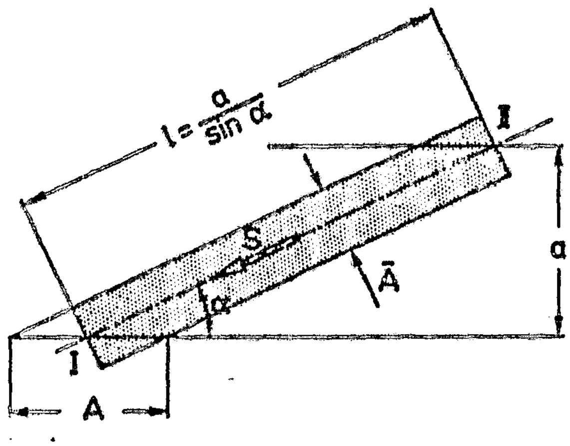

Figure 3.12 For the calculation of loss coefficients in a plain clearance

/58

In the considerations above it was assumed that both channel walls were at rest. In order to take into consideration the modified pressure loss for rotating channel walls, we start from the premise - as we did before - that the velocities w and their directions α represent average values across the clearance. Thus, the relative motion will then affect only the direction of the stream tube and the pressure drop. The resistance forces - which in a friction bearing, for instance, cause the characteristic pressure build-up ahead of the narrowest clearance - are disregarded here, because of the considerations in section 2.3.2.

According to Figure 3.13, below, at the wall rotating with a tangential velocity u, the relative velocity v will exist, as opposed to the absolute velocity at a fixed wall, w. If we consider only a wetted surface of the clearance, then the

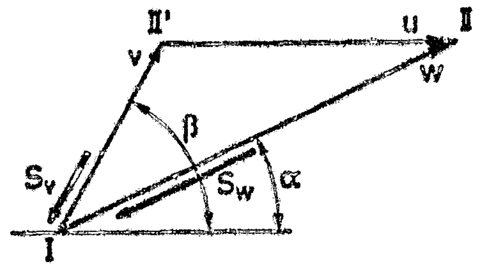

Figure 3.13 Velocities during channel wall rotation

hydraulic diameter becomes $d_{hydr} = 4$ s. Accordingly, the friction coefficient moving along the fixed wall from I to II will be only half that of equation (3.36). At the rotating surface, the fluid traverses the path from I to II' at relative velocity v and suffers the pressure drop

$$p_{v_{rot}} = \frac{\rho}{2} v^2 \frac{\lambda l}{4 s \sin\beta} .$$

in the process, as a first approximation.

If we assume an average friction coefficient λ for the pressure loss of both clearance surfaces, then the total pressure loss - using the definition in equation (3.10) - will be /59

$$\zeta_R = \frac{1}{2} \zeta \left(1 + \frac{\sin\alpha}{\sin\beta} \frac{v^2}{w^2}\right). \qquad (3.37)$$

The coefficient ζ to be used for the pressure loss at a fixed channel wall is that of equation (3.36). The local relative velocities v and their angles β are easily calculated, from the geometry in Figure 3.13, as a function of the absolute velocity w, its angle α and the tangential velocity u. At least for flows with a strong torsional effect, the equation above will provide an estimate of the modified pressure loss.

3.3.1.2. Labyrinth clearance

The processes taking place in a labyrinth chamber with incomplete vortexing of the velocities were investigated in detail by Groddeck [26]. Using an expression for the mixed friction between the fluid flowing away from the seal peak and that at rest in the chamber, while taking into account the friction against the fixed channel wall, the impulse equation was satisfied with the stipulation that the pressure remained constant during vortexing. By means of a friction coefficient λ_L - which contains both the wall friction and the mixed friction - it is possible to calculate the velocity reduced along the length t in the chamber,

$$w_K = w_I \frac{1}{1 + \lambda_L \frac{t}{2s}}$$

as a function of the velocity w_I at the preceding peak. Taking this residual velocity into account, the energy equation becomes

$$p_I + \frac{\rho}{2} w_K^2 = p_{II} + \frac{\rho}{2} w_{II}^2 .$$

With the definition of equation (3.11), we obtain Groddeck's loss coefficient

$$\zeta_G = 1 - \left(\frac{1}{1 + \lambda_L \frac{t}{2s}} \right)^2 . \qquad (3.38)$$

/60

By applying the impulse equation normally to the flow, Groddeck also obtains a dependency on the pressure increase in the labyrinth chamber, due to the broadening of the stream upon leaving the peak. This causes an additional increase in the throughput, which according to Groddeck, however, can be neglected in most practical cases. The effect of wall rotation could be handled by Groddeck's equation as in the case of the plain clearance. We shall disregard it here, however, since a separation between the losses caused by friction and those due to vortexing is possible only with difficulty.

In an analogous consideration, Neumann [24] took into account - in a dioptric labyrinth - the portion of flow energy, (which in contrast to a true labyrinth is retained) for which the velocity energy is completely turbulent. When he applied it to a seal with a number z of peaks, he obtained a so-called excess pressure factor, which can be described by means of the loss coefficient ζ, defined in equation (3.10):

$$k_{ü} = \sqrt{\frac{z}{\zeta z + 1 - \zeta}} \ .$$

For a large number of seal peaks $z \to \infty$, according to [24] this excess pressure factor is a linear function of the ratio between clearance width and distance t of the peaks

$$k_{ü} = 1 + m \frac{s}{t} \ ,$$

where the proportionality factor m can be determined from comparative studies between dioptric and true labyrinths. We then obtain as loss coefficient for a seal peak,

$$\zeta_N = \left(\frac{1}{1 + m \frac{s}{t}}\right)^2 . \qquad (3.39)$$

This pressure loss coefficient after Neumann is shown in Figure 3.14, below, in comparison to Groddeck's equation (see equation (3.38)). With the ratio t/s, both equations [illegible] a function only of the seal's geometry, while at least for the hydraulically /61
smooth tube there is always the additional influence of the Reynolds number. For the resistance coefficient λ_L, Groddeck

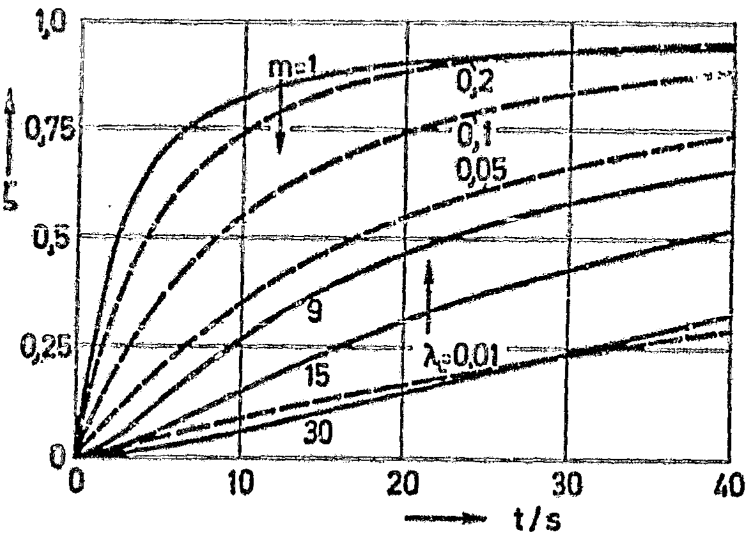

Figure 3.14 Loss coefficient for a labyrinth seal
__ after Neumann [24]; --- after Groddeck [26]

gives a value of 0.1. Neumann, using Egli's method (cf. also [15]) finds a proportionality factor of m = 16.6; from his own calculations [25], it is m = 8.9. At small clearance widths s or respectively, large distances t between the seal peaks, the limiting value $\zeta = 1$ is attained, corresponding to complete vortexing. Equations of this kind can be used also, as approximations, for flow affected by torsional forces, if instead of the chamber width we use the length of the local flow line, in accordance with Figure 3.12. Using a local clearance width $\tilde{s}$ at a seal peak, according to [24] the pressure loss coefficient for a labyrinth will be

$$\zeta_{s_{i,k}} = \frac{1}{\left(1 + m_i \frac{s - e \cos \varphi_{s_{i,k}}}{\Delta z_i / \sin \alpha_{s_{i,k}}}\right)^2} \quad . \qquad (3.40)$$

Hence, a more marked vortexing of the velocity is achieved for small flow angles.

/62

3.3.1.3. Entrance, bend and exit losses

According to Figure 3.3, the flow changes course four times, perpendicularly to the reference edges. While at the entrance and the exit the flow through the turbine stators is of importance to the loss coefficients defined here, at the flow around edges in the radial clearance (bend loss) only the local geometry can be of significance.

If we assume that at the clearance entrance the available velocity energy is fully used, then the loss coefficients will be taken as $\zeta^z_{CE} = \zeta^\psi_{CE} = 0$ (cf. equation (3.50)). In addition, we must take an entrance loss into account, relative to the velocity at the first support plane. Since the tangential component does not change direction in space, we can set the loss coefficient $\zeta^\psi_{WE} = 0$, while the loss coefficient for the normal component is assumed to be approximately $\zeta^z_{WE} = 0.2$, although much larger values are also possible. In principle, loss coefficients could occur here that are dependent on, say, clearance throughput or, according to section 2.3.3., on local overlapping.

If two plain clearances follow one another, then we can start by applying the bend losses from tube hydraulics. It must be remembered though, that the flow around such a bend is diagonal and additionally, that it can show very variable entrance and exit surfaces. However, with the energy equation given in (3.15), the possibility exists to consider separately the losses in tangential and in normal direction; here the total pressure loss at a bend can be expressed as a function of influx and outflow velocities. The pressure losses caused by the peripheral or tangential component of the velocity can be disregarded as $\zeta^\psi = 0$, following the same considerations as earlier. This means that if the control space's entrance and exit surfaces are equal, the peripheral velocity is fully maintained. Considering only the normal component, we can use conventional bend losses, although according to [16] these strongly depend on the construction form. For application to seal clearances, we could use constant values $\zeta^z = 0.2$ to 1.0, at the periphery, where /63 the effect of variable surface characteristics can be described at least approximately by a corresponding subdivision into local influx and outflow velocities.

If a labyrinth seal follows a radial entrance, then the velocity vortexing at support location E_{nE} can be expressed in a manner similar to that used for a seal peak. If we assume the pessure loss coefficients to be the same for the tangential and the axial components of that velocity,

$$\zeta_{ES}^{z} = \zeta_{ES}^{\varphi} = \zeta_{ES} ,$$

then, in analogy to equation (3.40), we should have

$$\zeta_{ES} = \frac{1}{\left(1 + m_{ES} \dfrac{s_E}{s - e \cos \varphi_{E,nE,K}}\right)^2} . \qquad (3.41)$$

In addition, it would be possible here to provide loss coefficients ζ_{SE} for the entrance loss at the first peak. However, with $\zeta_{SE}^{z} = \zeta_{SE}^{\psi} = 0$ we shall have to assume that the pressure loss occurring here is negligible compared to the vortexing of the flow-off velocity at support location E_{nE}. An analogous procedure is possible if a plain seal (outlet) follows a labyrinth seal. In this case we describe the vortexing at the last peak by

$$\zeta_{SA}^{z} = \zeta_{SA}^{\varphi} = \zeta_{SA}$$

where the coefficient ζ_{SA} is to be calculated using equation (3.40). With $\zeta_{AS}^{z} = \zeta_{AS}^{\psi} = 0$, any loss at the entrance to the radial exit can be neglected, once again.

Behind the seal clearance, the flow in the meridian channel transfers no velocity energy ($\zeta_{CA} = 0$) to the clearance flow. Hence the static pressure of the main stream will be imposed on the exiting flow. Under certain conditions, which depend very strongly on the geometry of the clearance exit, a portion of the exiting flow energy can be transformed into pressure. This is taken into account by means of exit losses $\zeta^{z}_{WA} = \zeta^{\psi}_{WA} < 1$, which very significantly affect the pressure distribution within the clearance. In the normal case, however, with $\zeta_{WA} = 1$, we have to assume that the velocity is completely turbulent, at the exit. /64

3.3.2. Impulse-loss coefficients as a function of pressure loss

3.3.2.1 Analogy with a straight stream tube

The coefficients $\overline{\zeta}$ (equation (3.18)) introduced in the impulse equation for the support forces S, which act on the control space due to friction, can be determined - in a straight stream tube - with the length l, from Figure 3.12. From the impulse equation for the direction of flow

$$\dot{m}\,(w_I - w_{II}) + p_I \overline{A}_I - p_{II} \overline{A}_{II} - S = 0$$

and the energy equation

$$(p_I - p_{II})\frac{1}{\varrho} = \frac{1}{2} w_{II}^2 - \frac{1}{2} w_I^2 + p_v \frac{1}{\varrho}$$

we obtain, considering a constant flow cross-section $A_I = A_{II} = A \sin\alpha$, the frictional force

$$S = p_v \overline{A}$$

as a function of the pressure loss

$$p_v = \frac{\rho}{2} w^2 \zeta .$$

A different derivation is possible, using the loss-energy E_v, obtained from the decrease in the specific kinetic energy $p_v(1/\rho)$ multiplied by the mass inside the stream tube under consideration,

$$E_v = \frac{1}{\rho} p_v \cdot \rho \bar{A} L = S L .$$

/65

Since this loss-work must, in turn, be equal to the product between the frictional force and the friction path length, we obtain the same result above. Using the continuity equation (3.9) and the pressure loss from equation (3.10), we now obtain the frictional force

$$S = \dot{m} w \frac{1}{2} \zeta \qquad (3.42)$$

at any arbitrary support point. A comparison with the expression chosen for equation (3.18) provides a simple relationship between the impulse loss coefficient $\bar{\zeta}$ and the friction coefficient ζ after equation (3.36)

$$\bar{\zeta}_{i,k} = \frac{1}{2} \zeta_{i,k} . \qquad (3.43)$$

It is assumed here, however, that both channel walls are at rest. The support force generated by the friction against the rotating wall is determined similarly to the previous derivation, from a stream tube with an inclination angle β,

$$S_{rot} = p_{v\,rot} \bar{A} = \frac{\rho}{2} v^2 \frac{\lambda L}{4 \bar{s} \sin\beta} A \sin\beta , \qquad (3.44)$$

where the relative velocity $\underline{v}$ is calculated from Figure 3.13. The frictional forces against the direction of flow - described by the angle α - are described by means of equation (3.18), in the impulse equations for the tangential direction. The above frictional force on the rotating part, however, according to Figure 3.13 acts at the support point at an angle β. In order to determine an impulse loss coefficient $\bar{\zeta}_R$ which corresponds to definition (3.18) at both channel walls, we must hence introduce a correction factor. As a function of the pressure loss coefficient ζ for two walls at rest (equation (3.36)) we then obtain

$$\bar{\zeta}_R = \frac{1}{4} \zeta \left(1 + \frac{v^2}{w^2} \frac{\cos\beta}{\cos\alpha}\right). \qquad (3.45)$$

For large tangential velocities and small torsional effect, the iterative consideration of any rotation, using the impulse loss coefficient above, can fail for numerical reasons. In calculations for such cases, the frictional force from equation (3.44) would have to be introduced directly in the impulse equation.

/66

3.3.2.2. Considerations based on the energy equation

Especially in the application to flow around bends, we may assume - certainly for a central rotor position - that in the tangential direction there is no pressure loss, but merely a decrease in that velocity component. Consequently, the energy equation (3.16) can be divided into two partial equations, for the pressure loss in normal direction and the velocity decrease in tangential direction.

$$\begin{aligned} \frac{1}{\rho}(p_I - p_{II}) &= \frac{1}{2} w_{II}^2 \sin^2\alpha_{II}(1 + \zeta_{II}^z) - \frac{1}{2} w_I^2 \sin^2\alpha_I (1 - \zeta_I^z), \\ 0 &= \frac{1}{2} w_{II}^2 \cos^2\alpha_{II} (1 + \zeta_{II}^\varphi) - \frac{1}{2} w_I^2 \cos^2\alpha_I (1 - \zeta_I^\varphi). \end{aligned} \qquad (3.46)$$

The second equation yields the same result as the impulse equation (3.17) if external compressive forces are neglected, i.e., if we set

$$\left.\begin{aligned} 1-\zeta_I &= \sqrt{1-\zeta_I^2}\ , \\ 1+\zeta_{II} &= \sqrt{1+\zeta_{II}^2}\ . \end{aligned}\right\} \qquad (3.47)$$

These relationships can also be applied to a plain clearance, and for small clearance widths - i.e., large pressure loss coefficients - yields more precise results, there. Increasing the number of support locations, for the same clearance length, the flow paths in a control space will be shorter, and hence the pressure loss coefficients will be smaller. Test calculations show that using equation (3.47), the number of support locations has no noticeable effect provided $\zeta < 1$ is maintained. In contrast, this is not valid for equation (3.43), obtained from a simplified description, on a straight stream tube. Nevertheless, it will lead to the same result, provided the pressure loss coefficients are sufficiently small.

3.3.2.3. Considerations on a labyrinth clearance /67

The support forces that cause a decrease in the torsional effect in a labyrinth have already been taken into consideration by impulse equation 3.17). Since the afflux from the labyrinth chamber to an immediately subsequent seal peak was assumed to occur without losses, the support force acting on the entire control space (cf. Figure 3.9) can be determined by a consideration of only the processes of velocity energy vortexing inside the chamber. If it is assumed that in a labyrinth chamber as that in Figure 3.15 there is no pressure change due to the turbulence of velocity w_I, then the

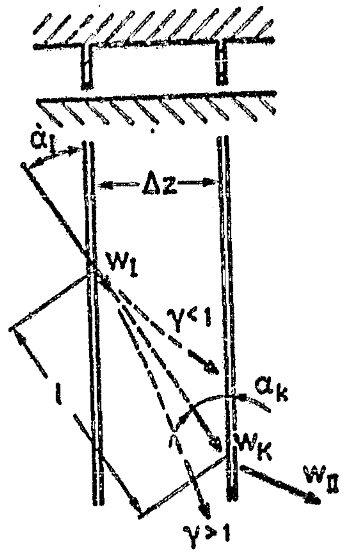

Figure 3.15 Direction change in the labyrinth chamber

residual velocity w_K can be determined by the energy equation

$$\frac{\varrho}{2}\, w_I^2\,(1-\zeta_I) = \frac{\varrho}{2}\, w_K^2$$

independently of the pressure loss coefficient ζ. Eliminating the chamber velocity, the impulse equations in the tangential direction and perpendicularly to it will be - provided that for a concentric rotor position and constant chamber pressure we disregard the compressive forces on the control space's surfaces -

$$\dot{m}\, w_I \left[\cos\alpha_I - \cos\alpha_K \sqrt{1-\zeta_I}\,\right] - \bar{S}\cos\alpha_S = 0\,,$$
$$\dot{m}\, w_I \left[\sin\alpha_I - \sin\alpha_K \sqrt{1-\zeta_I}\,\right] - \bar{S}\sin\alpha_S = 0\,.$$

The angle α_K depends on the processes in the labyrinth chamber and can be determined precisely only from measured flow line courses. It is possible to determine - depending on this angle - the supporting force $\bar{S}$ and its angle α_S, /68

$$\left.\begin{aligned} \operatorname{ctg} \alpha_S &= \frac{\cos \alpha_I - \cos \alpha_K \sqrt{1-\zeta_I}}{\sin \alpha_I - \sin \alpha_K \sqrt{1-\zeta_I}} , \\ \bar{S} &= \dot{m} w_I . \sqrt{1 - 2\sqrt{1-\zeta_I} \cos(\alpha_I - \alpha_{II}) + (1-\zeta_I)} . \end{aligned}\right\} \qquad (3.48)$$

Since impulse equation (3.17) already includes the assumption that the support force works against the velocity w_I at the seal peak, it is necessary to introduce a correction factor γ that will take into account the redirection of flow inside the labyrinth chamber. With the definition of the support force by equation (3.18) and the direction established in equation (3.17), using the impulse equation for the tangential direction, we obtain the impulse loss coefficients

$$\xi = 1 - \gamma \sqrt{1-\zeta} \quad \text{where} \quad \gamma = \frac{\cos \alpha_K}{\cos \alpha_I} . \qquad (3.49)$$

According to Figure 3.14, for $\gamma > 1$ the stream tube would be redirected in a peripheral direction, for instance, through rotation of the channel wall; for $\gamma < 1$, larger afflux angles to the next seal peak would be attained. The latter is conceivable if the vortexing of the tangential component were enhanced, for instance by building special devices, such as crossbars, into the labyrinth chambers. On the one hand, this would improve turbulence within the labyrinth chamber. On the other hand, in this manner the velocity becomes only partially turbulent, which corresponds to redirection without pressure loss. This effect is more thoroughly studied in section 3.6, using a calculation example.

For a total loss of the velocity energy $\zeta = 1$, equation (3.49) always provides, with impulse equation (3.17) - independently of the correction factor γ - a flow that is normal to the next seal peak; in contrast, without redirection and without velocity turbulence ($\gamma = 1$, $\zeta = 0$) the same flow angle as that at the previous peak will be repeated. Thus, the effect of the redirection factor introduced increases with lower turbulence coefficients ζ. For the usual seal constructions, however, it /69 should be $\gamma \approx 1$; then the same impulse loss coefficient is obtained as was found from energy considerations, in the previous section.

Figure 3.16, below, shows the effect of the redirection factor on a stream tube. For the same afflux angle and the same velocities at the seal peaks, we calculated the outflow angles and the magnitude and direction of support force $\bar{S}$, from the

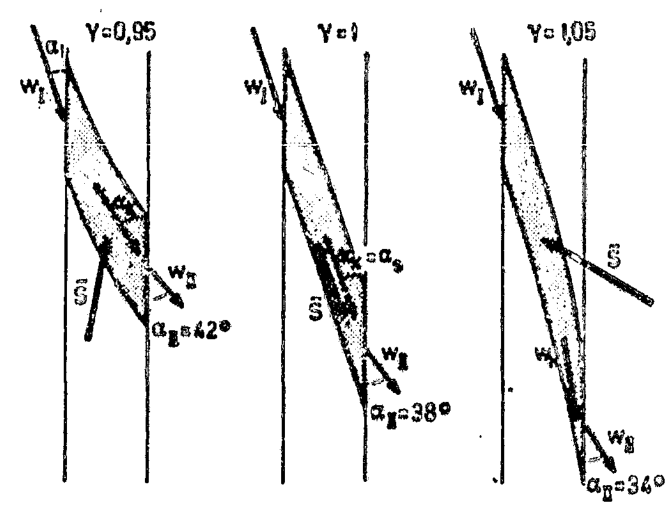

Figure 3.16 Stream tube changes due to the constant γ (ζ=0.3; α_1=20°; A_I=A_{II})

above relationships. Due to redirection within the chamber, the stream tube is changed considerably. However, as a first approximation we shall assume that the flow-line course -

strictly speaking valid only for $\gamma = 1$ – can be calculated as outlined in section 3.1.1. Due to the partial velocity turbulence, the outflow angle always becomes larger and depends on the redirection γ. Through the impulse equation, an angular change is coupled to the stream tube throughput which, on the other hand, depends substantially on the flow angle within the clearance. This relationship is described by the discharge equation (3.29).

/70

For a relative afflux energy $C_E^{\times}$, the round brackets contain a combination of the pressure and impulse loss coefficients, which we simplified here for the case of two seal peaks ($n = 2$, $\zeta_2 = \zeta_A = 1$):

$$D = \left\{ (1 - \zeta_{CE}^{\varphi}) - (1 - \bar{\zeta}_{CE})^2 \left[\zeta_1 + (1 - \bar{\zeta}_1)^2 \right] \right\}.$$

Using the impulse loss coefficient of equation (3.49), we obtain for the case, for instance, that the afflux energy and the torsional force can be used completely, for $\zeta_{CE} = \bar{\zeta}_{CE} = 0$,

$$D = \left\{ 1 - \left[\zeta_1 + (1 - \zeta_1)\, \varphi_1^2 \right] \right\}.$$

Since $\zeta_1 < 1$ must be, a redirection to the tangential direction $\gamma > 1$ with $D < 0$ would bring a throughput decrease, as a consequence, according to equation (3.29), and viceversa. The cause for this lies in the modification of the outflow angle which occurs (see Figure 3.15)) due to the throughput-related redirection. For $\gamma = 1$, with $D = 0$ we obtain the special case already mentioned in section 3.2.6. Physically, an effect of the afflux torsion on the throughput is not meaningful, since it must be assumed that an additional support force, acting on the stream tube due to the redirection, is balanced by correspondingly changed boundary conditions at the clearance entrance. If, in analogy to equation (3.49), we assume the relationship

$$1 - \bar{\xi}_{CE} = \gamma_{CE} \sqrt{1 - \xi_{CE}^{\varphi}} \, ,$$

then for D = 0 (i.e., no effect of the afflux torsion on the throughput), we can define the factor

$$\gamma_{CE} = \frac{1}{\sqrt{\sum_{i=1}^{n} \left(\xi_i \prod_{\nu=1}^{i-1} (1 - \bar{\xi}_\nu)^2 \right)}} \, .$$

for the labyrinth clearance considered in equation (3.29).

/71

For $\gamma_{CE} < 1$, the torsional effect supplied at the clearance is less than the flow before the entrance makes possible; hence the impulse coefficient has to be corrected by

$$\bar{\xi}_{CE} = 1 - \gamma_{CE} \sqrt{1 - \xi_{CE}^{\varphi}}$$

In contrast, . " the flow is redirected in an axial direction in the labyrinth chamber, with $\gamma < 1$, then it may be assumed that at the entrance a smaller proportion of the velocity energy will be supplied to the tangential component. The equation

$$\xi_{CE}^{\varphi} = 1 - \frac{1}{\gamma_{CE}^2} (1 - \bar{\xi}_{CE})^2$$

takes this into account. The condition (3.50), above, must be satisfied for each of the stream tubes variable along the perimeter, which is readily possible, in connection with the iterative determination of the loss coefficients, also for the more general clearance form with radial entrance and exit.

3.3.3. Mixed frictional force at the channel exit

Past the stator seal clearance, the tangential velocity in the meridian channel is relatively large. It is conceivable that here a mixed frictional force acts on the clearance flow. Using Fluegel's equations (cf. also [26]) this force can be described by a mixed friction coefficient $_A$, as a function of the exit surface area and the kinetic energy of the difference between the local tangential velocities,

$$R_{MA} = \bar{\lambda}_A A_{A_{mA}} \frac{\rho}{2} \left(c_A \cos \alpha_A - w_{A_{mA}} \cos \alpha_{A_{mA}} \right)^2 . \qquad (3.51)$$

The differences between the tangential velocities is determined iteratively for each stream tube, according to section 3.4, simultaneously with the loss coefficients. To begin with, the force above only acts to modify the outflow angle of the last control space, since due to the fluid's viscosity the frictional forces were disregarded in the remaining control spaces. With /72 a torsion-free afflux and eccentric rotor position, an equalizing flow occurs, which along the perimeter is symmetrical to the position of the narrowest clearance width. Taking this modified outflow angle into consideration, larger mixed frictional forces in the tangential direction are generated in front of the narrowest clearance than behind it. Due to the outflow angles corrected by these additional forces, the pressure losses at the exit now change, as does the pressure distribution within the radial clearance. Due to this, in spite of a torsion-free afflux and without considering rotation, a transverse force now also acts perpendicularly to the deviation (cf. section 3.6.)

This simplified description at least permits a qualitative evaluation of the mixed friction beyond the clearance; according to [26], for the mixed friction coefficient we can use $_A$ 0.1. According to Table 3.2, the outflow angle caused by the mixed friction force is a function of the throughput. Since it, in turn, depends strongly on the exit loss (and hence, also on the outflow angle), at the exit a similar condition ought to be satisfied as that for the entrance, in the previous section, by means of which it is assumed that the throughput remains constant under the effect of mixed friction.

3.3.4. Determination of loss coefficients from a measured pressure distribution

If the pressure distributions are known from measurements, for a few essential reference planes, then it should be possible to determine the loss coefficients from these in such a manner that there is agreement between measurements and theory. However, knowledge of the course of the flow lines is assumed, here, since small changes in the torsional forces can decisively affect the pressure drop in the stream tube. If one makes assumptions regarding the impulse loss coefficients or their relationship to the pressure loss coefficients, then it must be possible to determine them from the measured pressure distributions, by means of the existing theory. To this end we can apply the same iterative calculation procedure we use in section 3.5, in which we calculate the loss coefficients from /73
Table 3.1, by means of the pressure differences obtained from measurements. In this manner, we obtain the pressure loss coefficients for each measurement plane or, in conjunction with Table 3.2, also the impulse loss coefficients. The two quantities can be determined simultaneously only if, for instance, the flow lines are rendered visible so that the angle change becomes known, and the losses become known by pressure measurements. In a labyrinth, however, the assumptions made on the composition of the flow lines from flow angles are additionally of importance, as are those made about stream contraction.

3.4. Calculation of the transverse forces acting on a rotor

In addition to the transverse forces discussed below, there are also moments that act on the eccentrically located rotor, due to the clearance flow. They are generated especially by the compressive forces on the seal's front side, while moments due to differences in the pressure drop are relatively small, within the radial clearance. Because of the mode of construction of turbine steps, such moments can occur especially in the case of the so-called recess steps, which have large frontal areas at the clearance entrance and exit. Since at these surfaces the pressure distribution still strongly depends on the estimated values for the bend-losses, and because the effect of such moments presumably is only small, we shall forego their numerical evaluation, in the context of this study.

3.4.1. Transverse forces from the pressure distribution

The general integrals for the forces due to the variable pressure p(z,), acting along the perimeter and the length of a cylinder were indicated in equation (2.24). Since the calculated pressure distribution is given only at support points, an appropriate interpolation procedure must be found to solve these integrals. For the longitudinal direction $\underline{z}$, as an approximation the pressure calculated for the support point should be constant across the control space's width, Δz. Hence the forces acting on the rotor can be expressed as sums that result from the integration of the pressure distributions $p(\psi)_i$ for each support plane, /74

$$\left.\begin{aligned} Q_{1D} &= -\sum_{i=1}^{n}\left(\Delta z_i\, r_S \int_0^{2\pi} p(\varphi)_i \cos\varphi \, d\varphi\right), \\ Q_{2D} &= -\sum_{i=1}^{n}\left(\Delta z_i\, r_S \int_0^{2\pi} p(\varphi)_i \sin\varphi \, d\varphi\right). \end{aligned}\right\} \qquad (3.52)$$

The pressure distributions can be described by means of a Fourier series, to be determined for the support points given in analogy to equation (3.19). If we select a dimensionless description of the pressure distribution, according to equation (3.34), then we have

$$\frac{p(\varphi)_i - p_A}{\Delta p_B} = A_0 + A_1 \cos\varphi + A_2 \cos 2\varphi + \dots A_m \cos m\varphi + B_1 \sin\varphi + B_2 \sin 2\varphi + \dots B_m \sin m\varphi \hat{=} \frac{p_{i,k} - p_A}{\Delta p_B}. \qquad (3.53)$$

For j support points, the number of coefficients is $m = (j/2)+1$, to maintain the functions $p(\psi)_i$ as exactly as possible. If we herewith integrate equation (3.52) along the perimeter, the Fourier terms of higher order cancel o· , as is readily shown. Thus the compressive forces acting on a rotor are obtained as a sum of the first Fourier coefficients A_1 or respectively, B_1 of each support plane i of a radial clerance, multiplied by the widths Δz_i of their control spaces,

$$\left.\begin{aligned} Q_{1D} &= -\Delta p_B \, r_S \, \pi \sum_{i=1}^{nS-f_L} \left(A_{1_i} \Delta z_i + f_L A_{1_{i+1}} \Delta z_{i+1} \right), \\ Q_{2D} &= -\Delta p_B \, r_S \, \pi \sum_{i=1}^{nS-f_L} \left(B_{1_i} \Delta z_i + f_L B_{1_{i+1}} \Delta z_{i+1} \right). \end{aligned}\right\} \qquad (3.54)$$

/75

Because of the different definitions for the control space in a labyrith and a plain clearance, we again introduced the control quantity f_L, as in equation (3.14). Because of the dimensionless description of the compressive forces, the above transverse forces are a linear function of the total pressure drop and also of the shroud band radius, while the effect of the total width, $b = \Sigma \Delta z_i$, is coupled to the amplitudes of the pressure distributions.

For full rotor eccentricity $e = s$, in general the pressure differences at the clearance entrance can amount only to Δp_B, making a double amplitude $2A \leq 1$ possible. Assuming a linear pressure decrease in axial direction we then obtain a force

$$Q_B = \frac{\Delta p_B}{2} r_S \pi \frac{b}{2} \frac{e}{\delta} . \qquad (3.55)$$

This maximum attainable compressive force - in which the relative eccentricity has been assumed to be linear - can be taken as a reference magnitude for the above transverse forces, from the pressure distribution.

3.4.2. Transverse forces from the clearance loss

The local tangential force changes with the variable clearance throughput at the entrance to the rotor blading. The integral of the components of this force along the perimeter yields the transverse forces acting on the rotor, as indicated in general in equation (2.10). This requires a knowledge of the local clearance loss, which can also be calculated from the ratio

$$\bar{\mu} = \frac{\dot{m}_{sp}}{\dot{m}_0} \qquad (3.56)$$

of the clearance throughput to the total mass flow, if we introduce a correction factor

$$\zeta_{sp} = \bar{\mu}\, g(\bar{\mu}) . \qquad (3.57)$$

The function $g(\bar{\mu})$ takes into account that the decrease in the tangential force included in ζ_{sp} is not directly proportional to the throughput ratio $\bar{\mu}$. Any indication on this - also available in [14] - can be made only based on efficiency measurements for the entire turbine step. It must be assumed, however, that the function $g(\bar{\mu})$ is different for stator and rotor clearance losses, since the tangential force at the /76 blading is affected in one case by the approaching mass flow and in the other, by the outgoing one.

With the above definition of the clearance loss, we obtain for the integral of equation (2.10), bearing in mind the quantities that are constant along the perimeter,

$$\left.\begin{aligned} Q_{1s} &= \frac{U_s}{\dot m_0}\int_0^{2\pi} g(\bar\mu)\,\sin\varphi\, d\dot m_{sp}\,,\\ Q_{2s} &= -\frac{U_s}{\dot m_0}\int_0^{2\pi} g(\bar\mu)\,\cos\varphi\, d\dot m_{sp}\,.\end{aligned}\right\} \qquad (3.58)$$

The local throughput per arc length can be described by means of a Fourier series

$$\begin{aligned}\frac{d\dot m_{sp}}{d\varphi} &= C_0 + C_1\cos\varphi + C_2\cos 2\varphi + \ldots C_m\cos m\varphi\\ &\quad + D_1\sin\varphi + D_2\sin 2\varphi + \ldots D_m\sin m\varphi \\ &\mathrel{\hat=} \frac{\dot m_k}{\Delta\varphi_k}\,,\end{aligned} \qquad (3.59)$$

whose coefficients are determined by the calculated throughputs $\dot m_k/\Delta\psi_k$ per arc length of the stream tubes. While at the rotor clearance we must use the channel widths $\Delta\psi$ and the tangential angles ψ of the first support location, $E_{1,k}$, at the stator it is appropriate to use values for the last support location, $A_{nA,k}$. If in equation (3.58) as a first approximation we set $g(\bar\mu) = 1$, then its integration will yield the transverse forces acting on the rotor, with the higher-order Fourier coefficients canceling out, again:

$$\left.\begin{aligned} Q_{1s} &= \frac{U_s}{\dot m_0}\,D_1\,\pi\,,\\ Q_{2s} &= -\frac{U_s}{\dot m_0}\,C_1\,\pi\,.\end{aligned}\right\} \qquad (3.60)$$

The clearance throughput for the entire seal can also be obtained by integration of equation (3.59), with the sum of the throughputs of all stream tubes of course yielding the same result,

$$\dot{m}_{sp} = \int_0^{2\pi} d\dot{m}_{sp} = C_0 2\pi = \sum_{k=1}^{i} \dot{m}_k \,. \qquad (3.61)$$

In principle, the above transverse forces can also be determined as the sum of the individual forces at each support location, although this could lead to larger errors, depending on their number. For the description of the transverse forces due to clearance loss referred to, the ratio of the isentropic tangential force to the turbine step's throughput must be known; for test calculations it may be assumed to be proportional to the tangential component of the afflux velocity.

3.4.3. Forces due to friction on the rotor surface

The frictional forces at the rotor surface also cause a resulting transverse force; however, for the usual cases of calculation, it is two orders of magnitude smaller than those mentioned previously. Equation (3.18) shows an expression for the frictional force acting on any arbitrary support point on the rotor surface, defined as positive in the direction contrary to that of rotation. If the components of this force are added for all support points in the entrance, the radial clearance and the exit, then we obtain the resulting transverse forces

$$Q_{1R} = -\sum_{k=1}^{i} \left(\sum_{i=1}^{nE} S_{E_{i,k}} \sin\varphi_{E_{i,k}} + \sum_{i=1}^{nS} S_{S_{i,k}} \sin\varphi_{S_{i,k}} + \sum_{i=1}^{nA} S_{A_{i,k}} \sin\varphi_{A_{i,k}} \right),$$
$$Q_{2R} = \sum_{k=1}^{i} \left(\sum_{i=1}^{nE} S_{E_{i,k}} \cos\varphi_{E_{i,k}} + \sum_{i=1}^{nS} S_{S_{i,k}} \cos\varphi_{S_{i,k}} + \sum_{i=1}^{nA} S_{A_{i,k}} \cos\varphi_{A_{i,k}} \right). \qquad (3.62).$$

/78

The frictional moment to which the rotor is subjected because of these forces can be calculated in a similar manner,

$$M_R = \sum_{k=1}^{j} \left(\sum_{i=1}^{nE} S_{E_{i,k}} \tau_{E_i} + \sum_{i=1}^{nS} S_{S_{i,k}} \tau_S + \sum_{i=1}^{nA} S_{A_{i,k}} \tau_{A_i} \right) . \quad (3.63)$$

The efficiency decrease for the turbine step resulting thereby is negligibly small, at least for the rotor.

3.5. Iterative solution to the problem

The solution of the equations in the preceding sections requires the extensive iteration outlined in Figure 3.17, which also follows the steps of the calculation program. The first inputs are the number of subdivisions n in the flow direction and j in tangential direction, as well as the seal geometry, including all radii, clearance widths, length and recess or chamber heights. Next come the pressures, velocities and angles for the main flow ahead of and behind the seal, as well as the average density and kinematical viscosity. In addition, the input must include the bend loss coefficients and the constants for the calculation of the turbulence or vortexing coefficients in the labyrinth.

The calculation itself starts with the estimated average flow angles α, established for each stream tube with its support points at peripheral locations ψ, channel widths $\Delta\psi$ and surfaces A. In a first iteration step, the loss coefficients along each flow line are determined. According to section 3.3., they depend on the flow paths and hence, both on the angles and the local Reynold's number. Once the loss coefficients have been

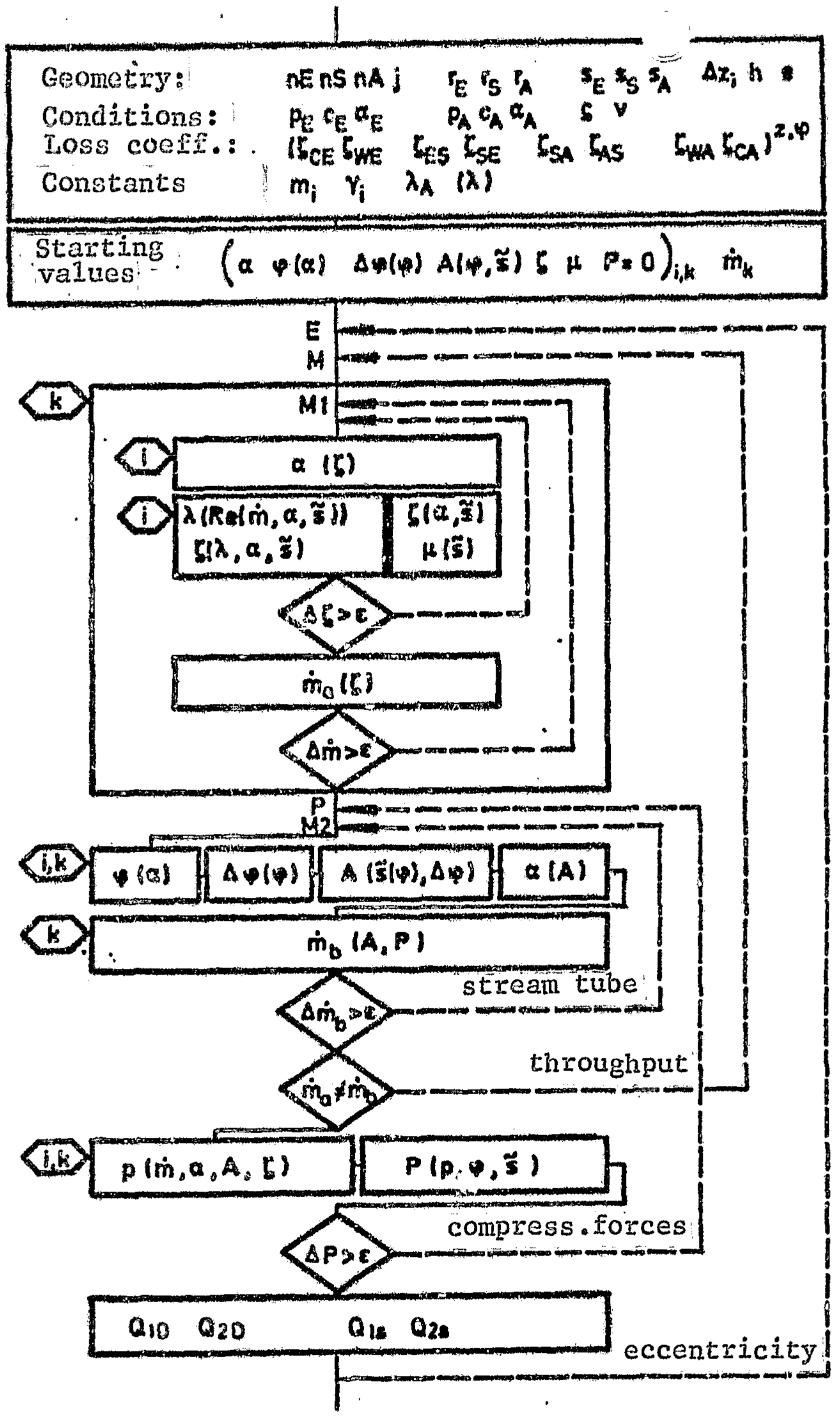

Figure 3.17 Iteration plan

determined - initially for constant throughput - with sufficient precision, the throughput of the stream tubes is calculated and iteratively improved beyond the defined level M1, already taking into account the changes in the flow angle, in accordance with section 3.2.5. This process is performed independently for all stream tubes k, as indicated in Figure 3.17, above, by the subscript field.

/80

In a further block, the geometry of the stream tube is calculated in accordance with section 3.1 and subsequently the throughput is corrected (to level M2). Since through the channel width the stream tubes affect each other, the calculation must be performed each time for all stream tubes. If the difference between the new throughput $\dot{m}_b$ and old throughput $\dot{m}_a$ of a stream tube is too large, then the loss coefficients must be recalculated, beyond level M.

Once the throughputs, angles, loss coefficients and surfaces of all stream tubes are precisely known, the pressure distribution is calculated. Once the Fourier coefficients have been obtained, this allows the determination of the compressive forces acting at each support location on the control space surfaces. These primarily change the geometry of the stream tubes; for this reason the iteration need not start from the beginning, but from index P. Subdividing throughput calculations into two partial iterations, starting at index M1 or respectively, M2, was chosen only to save calculation time, since the loss coefficients appparently only change very little.

For normal application cases the convergence is very good. However, for large torsional effects at the entrance and large eccentricities, the flow angles vary considerably along the perimeter, causing significant changes in the channel widths. It is recommended not to perform further iterations directly with the new value, but with a weighted average of the old and the new iteration values. While the end result will be attained somewhat more slowly, a divergence caused by excessive changes in the individual values will be avoided thereby. A similar procedure may also be necessary in the iterative calculation of the compressive forces, especially for large labyrinth chambers.

At the end of the overall iteration, the compressive forces Q_D acting on the rotor can be calculated from the pressure distribution, and the forces Q_S caused by the variable tangential force, from the variations in the clearance throughput. No new initial values need be set to calculate further eccentricities.

Based on the similarity of conditions, favorable initial values are obtained rather by increasing the eccentricity gradually. Since the course of the forces in general is only weakly non-linear, a few individual forces can cause an increase beyond the deviation as required for the vibration calculations in section 2.1. /81

3.6. Testing the calculation procedure using simple clearance forms

The essential parameters describing the clearance flow affected by torsional forces can be studied in Figure 3.18, using simple clearance forms. The clearance's diameter and length were chosen for their similarity to a test turbine, but without radial entrance or exit. Besides the radial clearance width and the chamber height h, the geometry of the seal remains unchanged and is supplemented only in Figure 3.37 with a radial entrance and exit.

Table 3.6 clarifies the most important equations for the

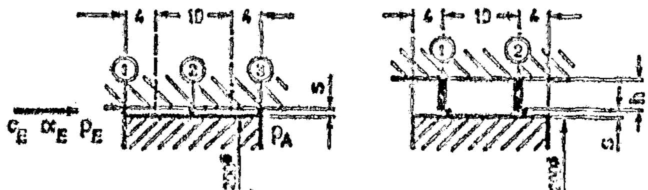

Plain clearance (nS=3, j=20)

Labyrinth clearance (nS=2, j=20)

Figure 3.18 Calculation examples of clearance forms

TABLE 3.6 Loss coefficients, afflux conditions and dimensionless quantities for calculation examples

$\zeta^{z}_{CE} = \zeta^{\varphi}_{CE} = 0$ $\zeta^{z}_{WE} = \zeta^{\varphi}_{WE} = \zeta_E$ $\zeta^{z}_{CA} = \zeta^{\varphi}_{CA} = 1$ $\zeta^{z}_{WA} = \zeta^{\varphi}_{WA} = \zeta_A$	Plain clearance: $\zeta_S(\lambda)$ from eq.(3.36) $\bar{\zeta}_S(\zeta_S)$ from eq.(3.43)(3.47) Labyrinth clear.: $\zeta_S(m)$ from eq.(3.40) $\bar{\zeta}_S(\zeta_S, \gamma)$ from eq.(3.49) μ ($\bar{S}$) from Fig. 3.8
$\varrho = 1{,}2 \frac{kg}{m^3}$, $\nu = 15\ 10^{-6} \frac{m^2}{s}$, $c_n = 41 \frac{m}{s}$, $c_E = \frac{c_n}{\sin\alpha_E}$, $c_A = c_n$, $\Delta p_B = p_E - p_A + \frac{\varrho}{2} c_n^2$, $\frac{U_S}{\dot{m}} = \frac{\Delta h_S^*}{u} = \Delta c_u = c_n \operatorname{ctg} \alpha_E$, 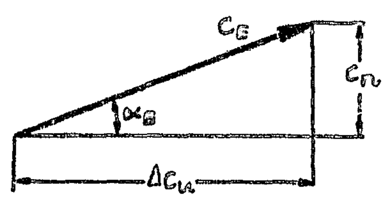	
$C_E^x = \frac{\frac{\varrho}{2} c_n^2 \operatorname{ctg}^2 \alpha_E}{\Delta p_B}$ $Q^x = \frac{Q}{Q_B} = \frac{Q}{\Delta p_B \frac{\pi}{4} r_S b \frac{e}{S}}$	$\dot{m}^x = \frac{\dot{m}}{\dot{m}_B} = \frac{\dot{m}}{A_B \sqrt{2\varrho\,\Delta p_B}}$ $M^x = \frac{\dot{m}_K}{\dot{m}_B}$, $P_i'' = \frac{p_i(\varphi) - p_A}{\Delta p_B}$

calculation of loss coefficients, and the boundary conditions given by a main flow unaffected by the clearance flow. A constant velocity component c_n is assumed ahead of the clearance, in normal direction, which is fully used with the assumed coefficients ζ_{CE}. Behind the clearance, only a normal velocity exists; however, because $\zeta_{CA} = 1$, it has no effect on the clearance flow. By changing the afflux angle, it is now possible to describe conditions such as they may occur ahead of the rotor clearance of a turbine step. Under these conditions, for a constant static pressure drop, the available total pressure drop Δp_B according to equation (3.15) also remains constant. To calculate the transverse forces that act on the turbine rotor due to the clearance loss, we set the ratio between the isentropic tangential force in equation (2.12) and the throughput equal to the velocity difference Δc_u. It corresponds to the tangential component of the afflux velocity, since the tangential or periferal velocity disappears, beyond the clearance. The relative afflux energy $C_E^{\times}$ can be modified by either the angles α_E or the pressure decrease Δp_B. /82 /83

For dimensionless descriptions $Q^{\times}$, the transverse forces acting on the rotor are expressed in terms of the force Q_B as the unit, according to equation (3.55). This also reflects in a qualitatively correct manner the ratio between the compressive forces Q_D and the forces Q_S from the clearance loss. To clarify the results, we have in part also provided the dimensionless pressure distributions $p_i^{\times}$ along the perimeter, at support locations i, according to Figure 3.18. Next to these pressure distributions, the throughput of the stream tubes, $M^{\times} = \dot{m}_K/\dot{m}_B$ has also been recorded, here referred to the total throughput according to equation (3.27).

The examples of calculations, below, are intended to illustrate the effect of the afflux conditions as well as that of the pressure and impulse loss coefficients on the transverse forces acting on the rotor. Initially, in a dimensioned description, we investigate the dependence of the forces on the eccentricity and the pressure difference, since they are included in the reference quantity. For a purely axial afflux, Figure 3.19 shows

ORIGINAL PAGE IS
OF POOR QUALITY

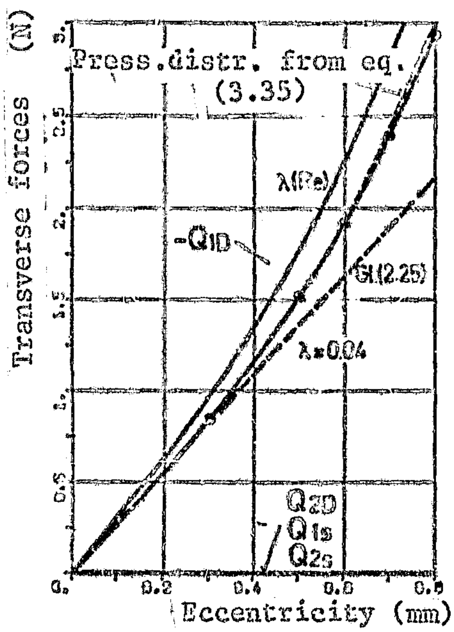

Figure 3.19 Plain clearance, s=1mm, α_E=90 , Δp_b=50mbar, ζ_E=0 ζ_A=1

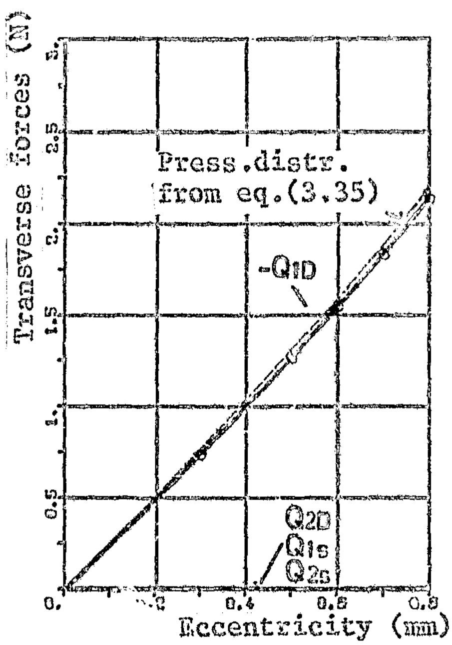

Figure 3.20 Labyrinth, s=1mm, H=4mm, α_E=90 , Δp_B=50 mbar, ζ_E= =0, ζ_A=1, $\zeta_1(m_1=9)$, $\mu(\bar{s})$ =1

the variation of the restoring force $-Q_{1D}$ (cf. definition in Figure 2.5) across the eccentricity. Since the compressive force Q_{2D} vanishes perpendicularly to the deviation due to a symmetrical pressure distribution, the forces Q_S caused by the variable tangential force at the turbine blading must be anulled, because of the assumption regarding the velocity increase Δc_u in Table 3.6. The approximate integration of the pressure variation in equation (2.25) yields a linear dependence on the eccentricity, which in comparison to complete calculations is valid only for small deviations. Due to the relatively small clearance length the effect of a balancing flow is negligible, in comparison to the calculation of the pressure variation from equation (3.35), for which a purely axial flow was assumed. Taking into account a variable tube friction coefficient $\lambda(Re)$, larger restoring forces are obtained, whose /84 dependence on the eccentricity is also non-linear. The same calculations were performed for the labyrinth clearance, in Figure 3.20, above. Due to the incomplete velocity vortexing in the labyrinth chamber, a restoring force $-Q_{1D}$ acts on the rotor, which varies nearly linearly across the eccentricity. Here too, the effect of the equalizing flow is only slightly larger than for the plain clearance. In accordance with equation (3.35), taking into consideration a contraction coefficient μ that varies with the local clearance width does have en effect, for a purely axial flow, since the surfaces at all seal peaks are reduced in the same manner.

/85

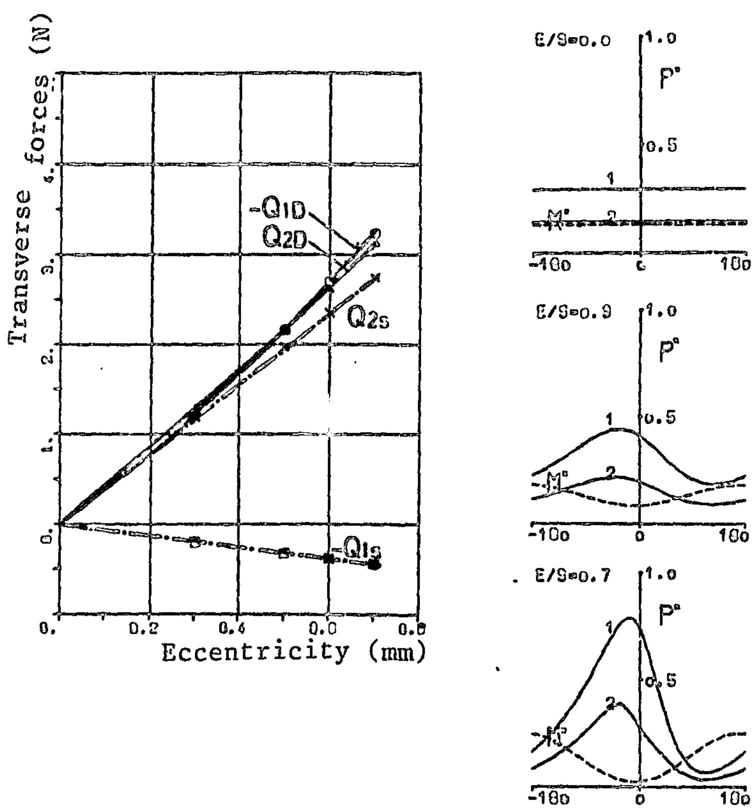

Figure 3.21 Plain clearance, s = 1 mm

C-2

For a flow affected by torsional forces, Figure 3.21, above, shows that there are transverse forces acting on the rotor, in the direction of the deviation, Q_1 and perpendicularly to it, Q_2. The cause for these forces can be seen from the pressure variations, next to the figure. For a central positioning, $e/s = 0$ and the throughput and the pressure along the perimeter are constant. The strongest pressure decrease occurs between the conditions ahead of the clearance, $p^{\times} = 1$, and the first support location, $p_1^{\times}$ (cf. also Figure 3.18), while pressure losses along the clearance and to the end state, $p^{\times} = 0$, are relatively small. For an eccentric rotor position, this pressure decrease varies in an inversely proportional manner with the local clearance width, which is smallest for $\psi = 0$. Due to the torsional effect, there is a spiral flow in the clearance, which results in variable cross-sections along the stream tubes, and causes the characteristic pressure maximum ahead of the narrowest clearance, as seen in the direction of torsion. As a /86
consequence, compressive forces arise, Q_{2D}, perpendicular to the deviation, which for a plain clearance are of the same magnitude as the restoring forces $-Q_{1D}$. The local throughput (broken line) modifies the tangential forces at the rotor blading, whose resultant generates a force Q_{2s}, perpendicular to the deviation, and the much smaller force Q_{1s}, which acts in the direction of the deviation. If the variations in the throughput were symmetrical around $\psi = 0$, then according to equation (2.15) that force would have to vanish. Across the eccentricity, the transverse forces are linear, with a small departure at Q_{1D}. This is also true of the flow with torsional effect, in a labyrinth clearance. Because of this it is possible to build dimensionless increases $Q^{\times}$ of the forces across the deviaition e, using the reference quantity of equation (3.55), and in accordance with Table 3.6. In all further calculations, this increase is determined from this force only for a relative eccentricity $e/s = 0.5$. We thereby also obtain an approximately

average value for a minimally linearized increase.

The effect of the radial clearance width is shown - with a view towards a vibration calculation - on the basis of an increase $q = Q/e$ of the force Q, assumed linear across the deviation $\underline{e}$. Qualitatively this also corresponds to the representation of transverse forces for equal rotor eccentricity. As Figure 3.22

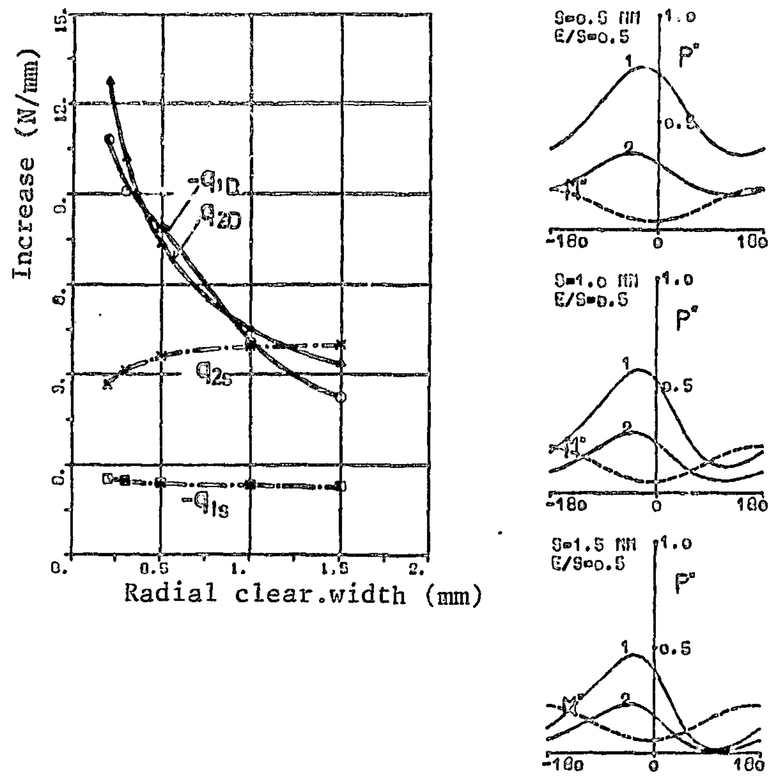

Figure 3.22 Plain clearance

shows, for a plain clearance the forces from the pressure distribution increase steeply for smaller radial clearance widths. The amplitudes of the pressure variations depicted are approximately equal, since they are valid, in each case, for half the maximum eccentricity, e/s = 0.5. For smaller clearance widths, the pressure loss increases along the clearance, thus increasing the pressure level at the entrance, $p_1^{\times}$.

As already explained in section 3.3.2.2., in a plain clearance and with decreases in the radial clearance width, under some circumstances inadmissibly large values can arise for the pressure loss coefficient ζ in a control space. Since the pressure losses depend on the flow paths within the control space, if necessary the number of support locations in the flow direction may have to be increased. Using equation (3.47), the calculations here were performed for all clearance widths with nS = 11 support points. However, no deviations worth mentioning /87 were observed for radial clearance widths $s \geq 0.5$ mm, even for nS = 3. The determination of impulse loss coefficients from sectionally straight stream tubes in accordance with equation (3.43) is also valid only for correspondingly short flow paths. However, the use of this relationship yields the same result - for a sufficiently large number of support locations - and was applicable, in particular and without restrictions, to nS = 3 and s = 1 mm.

For labyrinth clearances the number of support locations is determined by the number of seal peaks. In addition, only pressure loss coefficients $\zeta < 1$ can occur. As Figure 3.23 shows, the increase in the forces due to the pressure distribution, with small radial clearance widths is very much less than with a plain clearance. While the exciting force Q_{2S} is independent of the /88
radial clearance width, in accordance with equation 2.15, this results in a change based on the variable pressure loss coeficient. By disregarding the flow contraction $\mu = 1$, the exciting force Q_{2S} is proportionally increased to the throughput. However, the pressure distribution forces are not similarly altered, as the cross-sections along the flow tube become more equal because of the flow contraction μ (s), which is dependent on the local clearance width (c.p. fig. 3.8). A flow contraction which is constant along the perimeter would therefore cause an increase in the exciting force from the pressure distributor.

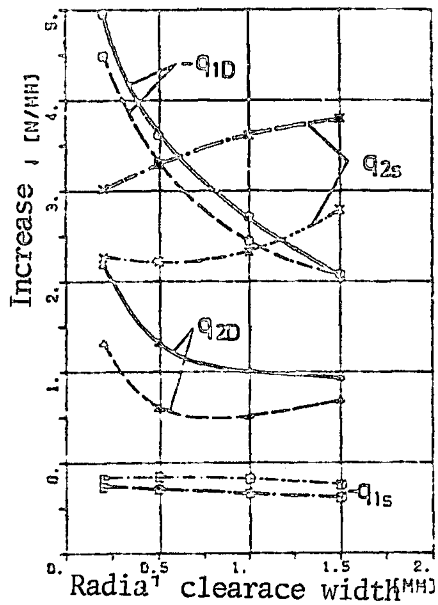

Figure 3.23 LABYRINTH H=4 MM

$\alpha_E = 20^\circ$ $\Delta p_B = 50$ mbar $(e/s = 0{,}5)$

$\zeta_E = 0$ $\zeta_A = 1$ $\zeta_1 (m_1 = 9), \gamma_1 = 1$

$\}\mu = 1$ $\}\mu(\bar{s})$

For a flow affected by torsional forces, the influence of a pressure drop on a plain clearance is shown in fig. 3.24, while fig. 3.25 shows the influence on a labyrinth. The lateral forces Q_s from the asymmetrical tangential force at the turbine blading indicate a parabola-shaped curve, as they are solely dependent on the throughput (which represents the square root of the pressure drop), based on the assumptions of tangential force according to table 3.6 (c.p. equation 3.27). Calculation of the exciting force Q_{2s} with a calculation of clearance loss according to Traupel (equation 2.15), results in reduced forces, as complete vorticity at both seal peaks is assumed.

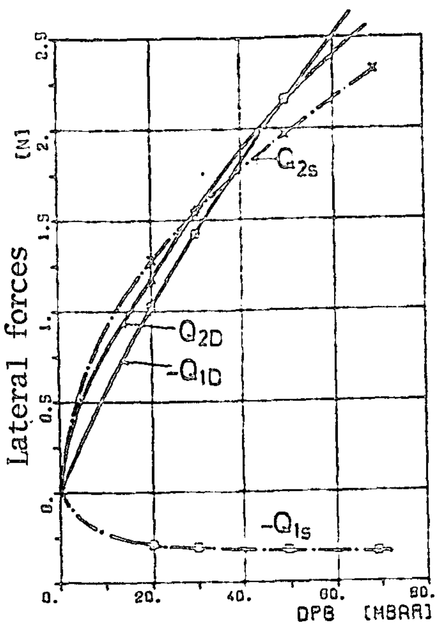

Figure 3.24 Plain clearance $s=1$ MM
$\alpha_E = 20°$ $e = 0{,}5$ mm
$\zeta_E = 0$ $\zeta_A = 1$ $\lambda(Re)$

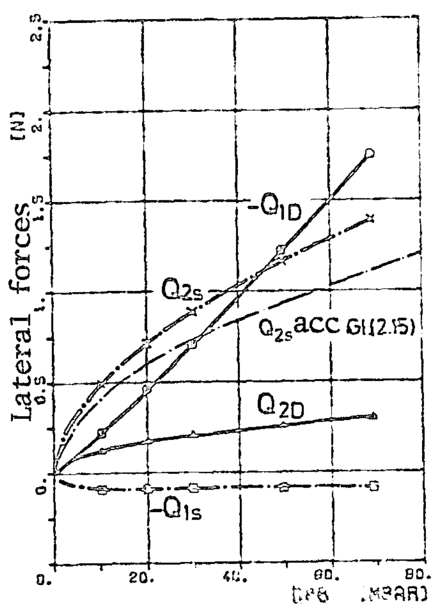

Figure 3.25

Assuming a purely axial flow, the restoring force [illegible] nearly /89
according to the pressure distribution shown in equation [illegible] with a pressure drop of Δp_B. This dependence also seems to be valid for a flow affected by torsional forces, at least for a labyrinth. However, the exciting force Q_{2D} at the two clearance dividers is non-linearly dependent on the pressure loss, as the relative afflux energy changes simultaneously, for which the significant influence is shown in the following figures. The pressure drop Δp_B = 50 mbar, which could be chosen from the weak reaction stage at the rotor clearance, was chosen as the initial value for further sample computations.

As all parameters contained in the reference values were changed, an additional dimensionless representation according to table 3.6 may
be selected, in which the forces Q^x and the throughput m^x is plotted on the /90
same scale. The relative afflux energy C_E^x was varied (see Figure 3.26) with the angle α_E ahead of the clearance, and with the pressure drop Δp_B, starting from the average value marked. The pressure distributions depicted next to the figure show the effect of the

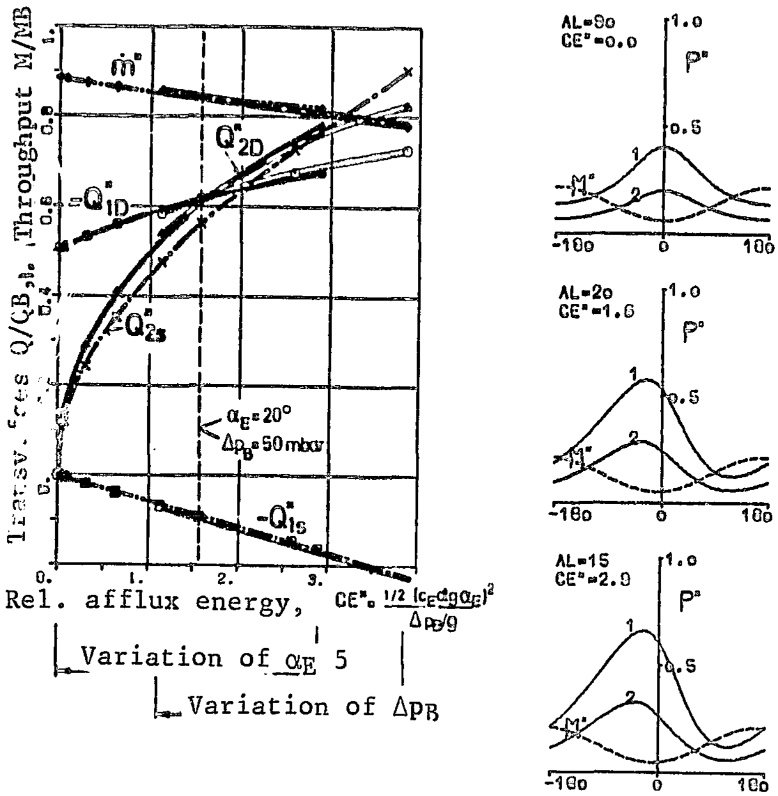

Figure 3.26 Plain clearance, s = 1 mm

afflux angle, due to which the location of the pressure maximum is displaced towards the direction of torsion, with a simultaneous increase in amplitude.

The local throughput changes in the same manner, with increasing torsional effects at the entrance. Because of the spiral flow within the clearance, the flow paths become longer, which leads to a slight decrease in the throughput of reference, $\dot{m}_x$, as a function of the relative afflux energy, C_E^x. Variations in the /91
angle or the pressure gradient do not yield the same results here either, for the transverse forces, since Reynold's number and hence the friction coefficient λ changes somewhat with the throughput's absolute quantity. However, within the range

depicted, the relative afflux energy $C_E^\times$ is characteristic for the generation of the compressive forces that act on the rotor. On the other hand, this also follows from the calculation of flow angles using equation (3.33), which for a given geometry and pressure loss coefficients are only a function of $C_E^\times$. It follows that exciting forces Q_{2D} from the pressure distribution are generated only in turbine steps with small reaction. Thus, besides a high tangential velocity ahead of the clearance, a relatively low pressure gradient must exist simultaneously. In contrast, the restoring forces Q_{1D}, due to the changed friction values depend only on the relative afflux energy.

The exciting force Q_{2s}, acting in the same direction as the compressive force Q_{2D}, also increases with the relative afflux energy, on the basis of our assumptions regarding the tangential force at the turbine blading, in accordance with Table 3.6. As the angle α_E varies, this increase is caused by the velocity difference, Δc_u, for an approximately constant clearance loss. In contrast, as the pressure difference Δp_B changes, the velocity difference Δc_u remains constant, while the clearance throughput changes. Obviously, both effects cause the force Q_{1s} - which acts in the direction of the deviation - to follow the same course.

In a similar representation, Figure 3.27 shows the effect of the afflux energy in a labyrinth clearance. Here, variations in the afflux angle and the pressure gradient yield exactly the same results, since the loss coefficients depend only on the geometry. Thus, at the clearance, for different throughputs but the same relative afflux energy, the flow angles will be the same. Due to stream contraction, the throughput (for the same reference quantity $\dot{m}_B$) is smaller than it is for a plain clearance, and hence the transverse forces Q_s generated are smaller. Since according to equation (3.40) the turbulence /42
coefficients ζ depends on the flow angle, the throughput becomes

Constant flow angle $\alpha_{i,k}=\alpha_E$, Δp_B=50mbar

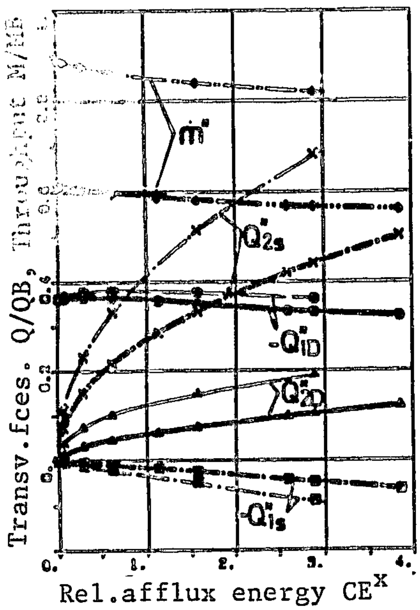

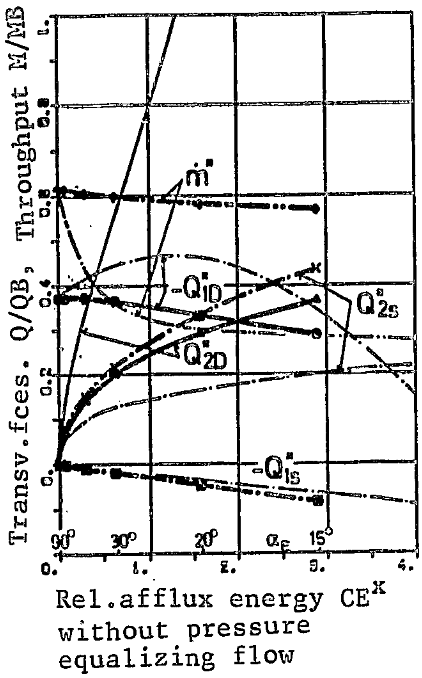

Figure 3.27 Labyrinth, s=1 mm H=4mm, ζ_E=0, ζ_A=1, $\zeta_1(m_1=9)$, γ_1=1

Figure 3.28 Labyrinth, s=1 mm H=4mm, ζ_E=0, ζ_A=1, $\zeta_1(m_1=9)$, γ_1=1, $\mu(\overline{s})$

smaller with C_E^x. Compared to the restoring force $-Q_{1D}$, the excitation force Q_{2D} from the pressure distribution is relatively small. However, Figure 3.28 shows that this changes considerably, if it is assumed that no compressive forces are acting on the surfaces of the control spaces (cf. Figure 3.10). Because of the chamber height, these forces are much larger for a labyrinth than for a plain clearance. They act at the perimeter, in the direction of the lower pressure and modify the stream tubes in such a way that not only does a pressure equalization take place, but there also is a phase displacement. This effect shall be further elucidated with the variation of chamber height. Because of the unordered flow in the labyrinth chamber, we could assume that the compressive forces acting on the stream tubes are much smaller than indicated by equation /93 (3.21). On the other hand, it is conceivable that the effect is balanced by a corresponding change in the local loss coefficients. If we neglect the pressure equalization flow in the labyrinth chamber, as above, the transverse forces acting on the rotor are of approximately the same magnitude as in the plain clearance, in accordance with Figure 3.26.

Figure 3.28 shows a strongly simplified calculation, under the assumption that all flow angles in the clearance are constant and correspond to the afflux velocity angle. This allows a closed solution for the pressure variation with equation (3.34), since the local surfaces for all stream tubes are given. The excitation force from the pressure distribution, Q_{2D}, increases considerably as the angle decreases. In fact, the maximum of the pressure distribution could be displaced so far, by prescribing the flow angle, that the force Q_{1D} will act in the direction of the deviation. Such a calculation could be very illuminating, qualitatively (cf. Rosenberg [28]). However, the excitation forces it yields from the pressure distribution, Q_{2D}, are too large unless one assumes an average flow angle that is considerably larger than the afflux velocity angle. It is possible to perform an approximated calculation for this average flow angle, as a function of the relative afflux energy, in accordance with equation (3.33), for instance assuming constant flow cross-sections and loss coefficients.

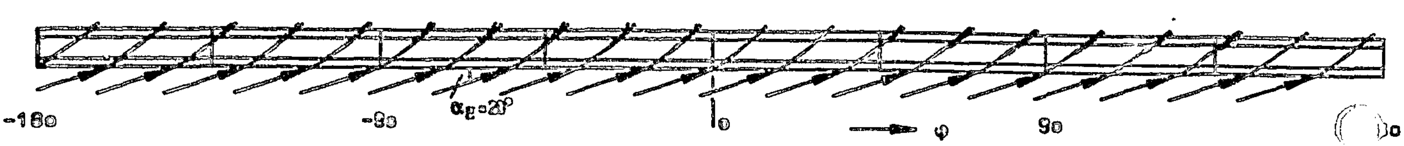

Flow-line course in a rolled out (to scale) seal clearance (Figure 3.18)

——— without pressure equalization flow
------ with pressure equalization flow for h=12mm

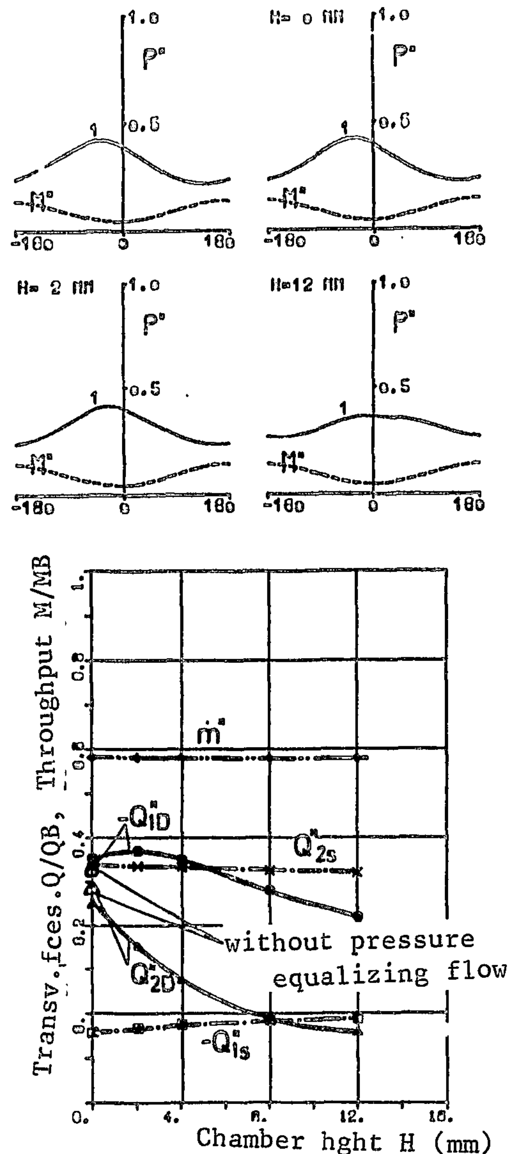

Figure 3.29 Labyrinth, s=1 mm, H=4 mm

In Figure 3.29, above, the height of the labyrinth chamber was varied (cf. Figure 3.18). While the forces related to the clearance loss, Q_s, were only marginally affected, especially the excitation force, Q_{2D}, related to the pressure distribution, decreased very markedly with increasing chamber height. An explanation for this arises out of the course of the flow-lines in a rolled-out, true to scale representation of the clearance as that shown at the bottom of page 102, above, for a large chamber height, in comparison to a calculation without pressure equalizing flow. Due to the lateral forces acting on the free portion of the control spaces, the flow lines are deflected somewhat more strongly just ahead of the narrowest clearance location ($\psi = 0$). Based on this minimal variation in the outflow angle and the channel width of the stream tubes, the pressure /95 variations in the labyrinth chamber are substantially affected, since the cross-sections normal to the direction of flow appear squared in the energy equation. Viewed in the tangential direction, ahead of the narrowest clearance are generated smaller exit velocities, and hence smaller pressure losses, whereby the characteristic pressure maximum in the labyrinth chamber is weakened with increasing chamber height. For very large chamber heights, even negative excitation forces Q_{2D} may occur. The calculation with a chamber height $h = 0$ corresponds to the same assumptions made for a plain clearance; taking the pressure equalizing flow into consideration changes the transverse forces by a maximum of 5%.

In subsequent test calculations, we shall now investigate the effect of changes in the loss coefficients. Starting from the standard case, Figures 3.30 and 3.31, below, show the variation in entrance and exit losses for both clearance forms. With increasing entrance loss ζ_E, the throughput and the transverse /96 forces acting on the rotor become smaller. Maintaining the exit loss $\zeta_A < 1$, the static pressure at the end of the clearance is lowered, since a part of the velocity energy is used as pressure again. This increases the throughput, which may become larger than the reference throughput ($\dot{m}^\times > 1$), since the latter is calculated only for a loss $\zeta_A = 1$. With increasing throughput, the average flow angles in the clearance also become larger (cf. equation (3.30)). This, in turn, displaces the maximum in the pressure distribution, peripherally to the location of the narrowest clearance, causing an increase in the restoration force $-Q_{1D}$, while the excitation force Q_{2D} becomes smaller.

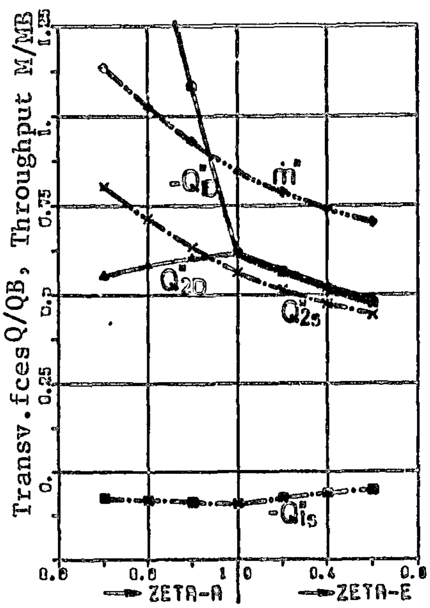

Figure 3.30 Plain clearance, $s = 1$ mm, $C_E^{\times} = 1.6$ $\lambda(Re)$

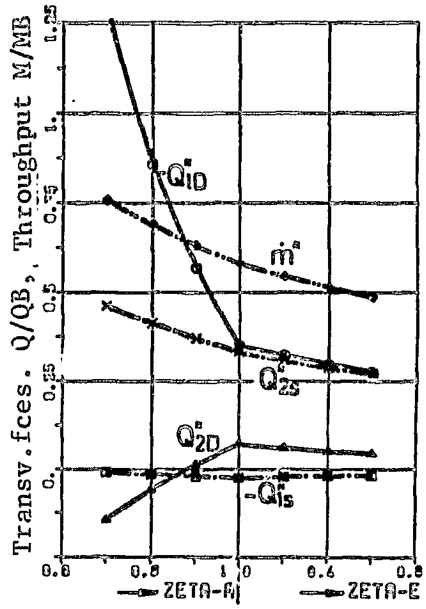

Figure 3.31 Labyrinth clearance $s=1$mm, $H=4$mm, $C_E^{\times}=1.6$, $\zeta_1(m_1=9)$, $\gamma_1 = 1$, $\mu(\bar{s})$

Assuming similar effects as in Figure 3.29, this could become negative for the labyrinth.

/97

Figure 3.32, below, shows the effect of the friction coefficient λ, which in the normal case is calculated from the local Reynold's number. For the restoring force a maximum is obtained, which also occurs with a purely axial flow. At low friction, the throughput increases, and at $\lambda = 0$ it takes the value of the reference quantity, $\dot{m}^{\times} = 1$, in which only the exit loss was taken into consideration. The pressure distributions chosen show very clearly that at lower friction coefficients, the decrease in the torsional effect in the clearance also is smaller, whereby the compressive force Q_{2D} increases. In Figure 3.33, below, the pressure loss or, respectively, the impulse loss

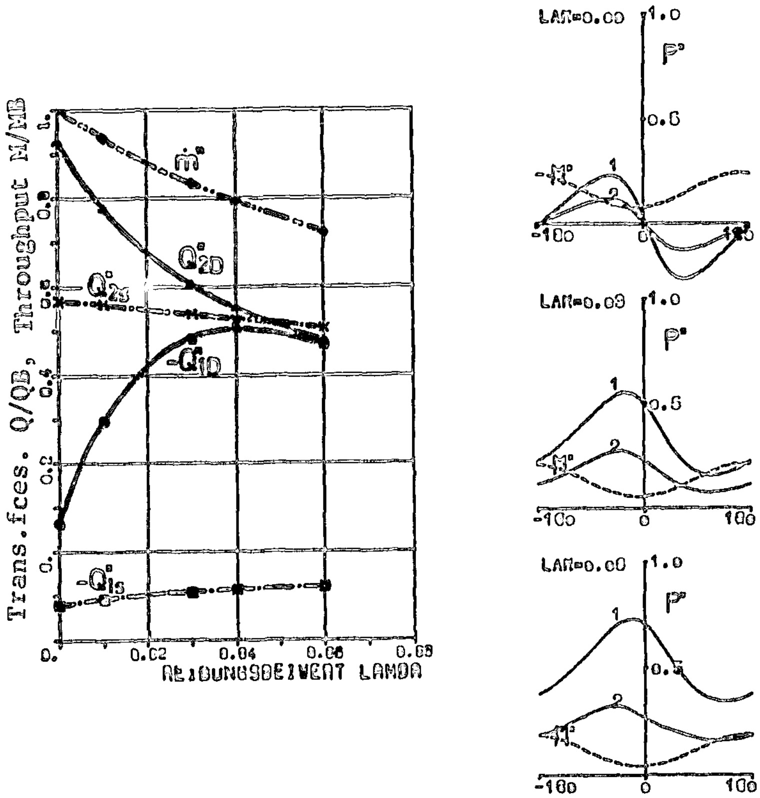

Figure 3.32 Plain clearance
s=1mm, C_E^x=1.6, ζ_E=0, ζ_A=1

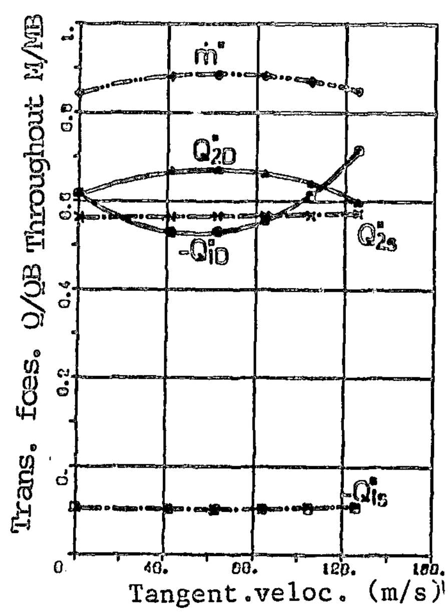

Figure 3.33 Plain clearance, s=1mm

coefficients are calculated from equations (3.37), or respectively, (3.45), to investigate the effect of a rotating channel wall. The throughput has a flat maximum at a tangential velocity of 60 m/s, which can be attributed to changes in the loss coefficients caused by the friction path (cf. Figures 3.12 and 3.13). Correspondingly, the compressive forces acting on the rotor are affected in a manner similar to the effect caused by a change in the friction coefficient λ.

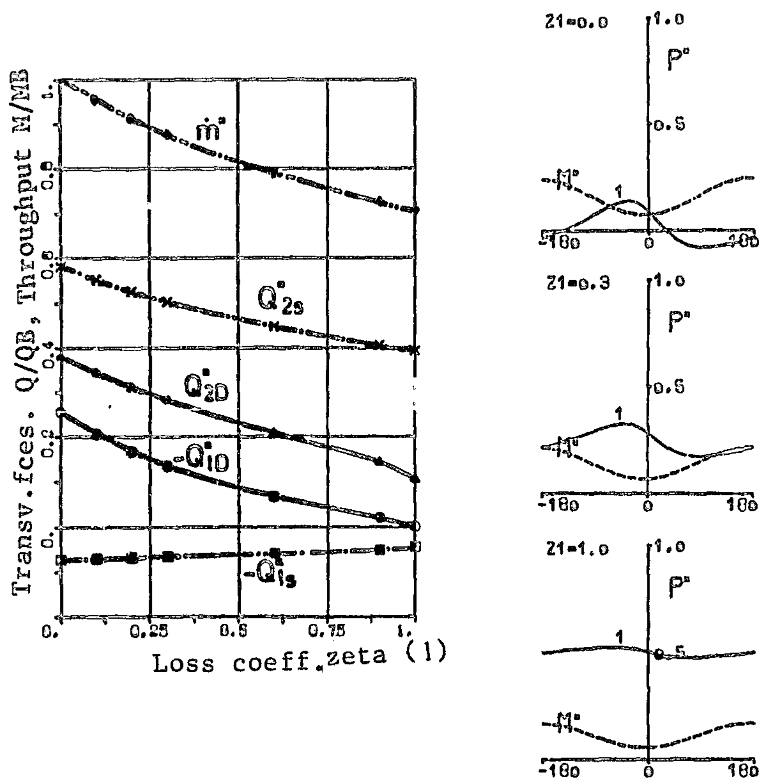

Figure 3.34 Labyrinth, s=1 mm, H=4mm

In Figure 3.34, above, a loss coefficient ζ_1 constant along the perimeter was assumed, at the first seal peak. In contrast to purely axial flow, because of the variable flow cross-sections, different pressure distributions occur within the clearance. For a flow without loss (ζ_1 = 0) the throughput attains its limiting value, $\dot{m}^{\times}$ = 1, since the stream contraction was disregarded, here. While the restoration force $-Q_{1D}$ disappears completely for ζ_1 = 1, the excitation energy Q_{2D} retains a finite value.

However, this value can increase no further with larger numbers of seal peaks, since due to complete turbulence, the flow with an impulse loss coefficient of $\bar{\zeta}_1 = 1$ runs normal to the second seal peak - i.e., purely axial flow. The pressure level in the labyrinth chamber is significantly affected by the loss coefficient and attains the values, approximately, that would be expected for purely axial flow (cf. equation (3.35)). Assuming a pressure loss coefficient constant along the perimeter, the excitation force from the pressure distribution is larger, here, than the restoring force, which also substantially changes the relations in Figure 3.27 or 3.28, respectively.

For a variable pressure loss coefficient ζ_1 (from equation (3.40)), Figure 3.35 shows the effect of the coefficient m_1.

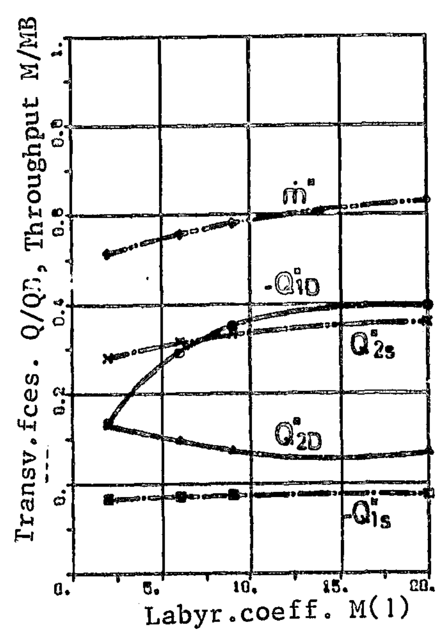

Figure 3.35 Labyrinth, s=1mm, H=4mm

It is inveresely proportional to the loss coefficient, as can already be seen from the behavior of the throughput. In a manner

similar to that of the friction coefficient for the plain /99
clearance (Figure 3.32), the restoration force $-Q_{1D}$ has a maximum that can be displaced with changing afflux torsion. Due to the pressure equalizing flow, the excitation force Q_{2D} is considerably smaller than for the plain clearance.

In Figure 3.36, below, the factor γ was modified, which in

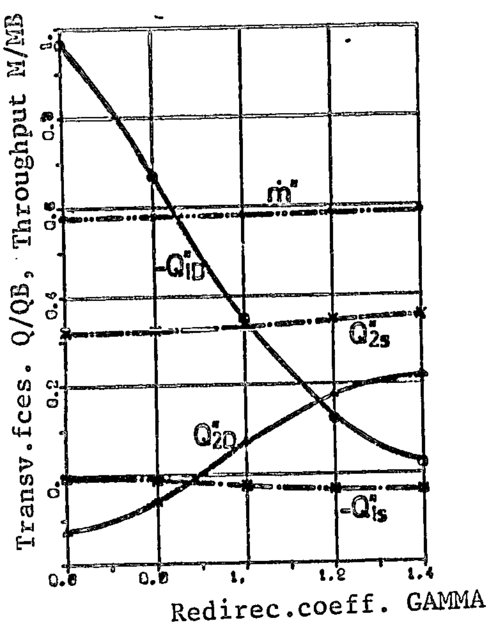

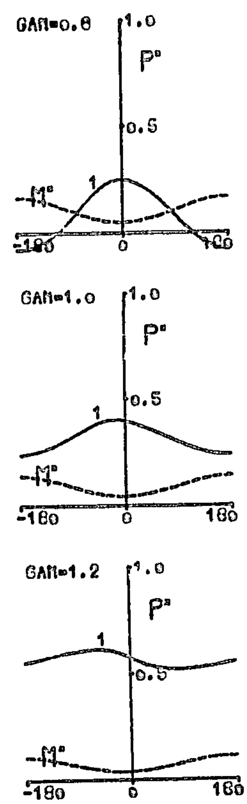

Figure 3.36 Labyrinth,
s = 1 mm, H = 4 mm

equation (3.49) describes the relationship between the pressure loss and the impulse loss in the labyrinth chamber. Starting from the standard value $\gamma = 1$, it was assumed that the flow, for instance due to the shaft's rotation, suffers a small decrease in the torsion ($\gamma > 1$). The pressure level in the chamber is thereby raised, since the pressure loss at the second seal peak increases because of the increased velocity (cf. Figure 3.16).

Because of the changed pressure distribution, somewhat larger excitation forces Q_{2D} are generated. If the velocity is redirected, in the labyrinth chamber, without further pressure losses ($\gamma < 1$), then only a little of the velocity energy can be destroyed at the clearance exit. This causes a lowering of the pressure level in the labyrinth chamber, with a simultaneous displacement in the location of the pressure maximum. A strong reduction in the torsional effect on the flow, caused for instance by crossbars within the labyrinth chamber, leads to a considerable reduction in the excitation force Q_{2D}, taking into consideration the lateral compressive forces acting on the free portions of the control spaces. This force can even adopt negative values, as has been observed during tests with these fittings [30]. The calculations above were performed, as a first approximation, with the composition of flow-lines from the /100 tangents to the flow angles, with a weighting factor $g_z = 0.5$, described in equation (3.4). Changes in this factor, even in extreme cases, caused no deviation worth mentioning in the remaining calculation examples. Taking into account the pressure equalizing flow in the application case described ($\gamma < 1$) is also only approximately valid, since by adding features in the chamber, additional compressive forces act on the stream tube.

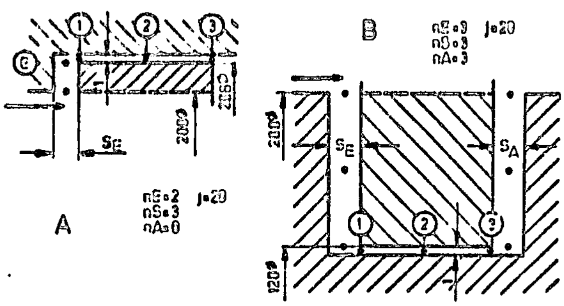

Figure 3.37 Plain clearance with radial entrance and exit (cf.Figure 3.18)

Figure 3.37, above, shows two further clearance forms, in which the flow's radius remained as in Figure 3.18. Form A approximately corresponds to the shroud band on a rotor, while /101 form B could be used as the stator clearance of a turbine step in chamber construction. The effect of the radial entrance in form A is shown in Figure 3.38, below. With a modification to the entrance clearance - to correspond to the axial clearance between stator and rotor blading - the forces due to the pressure distribution, Q_D, remain nearly constant, even though very large pressure differences occur in the entrance clearance, due to the higher velocities. In contrast, the forces Q_S decrease, due to the lower clearance loss in a smaller axial clearance, something confirmed also by measurements to be discussed later.

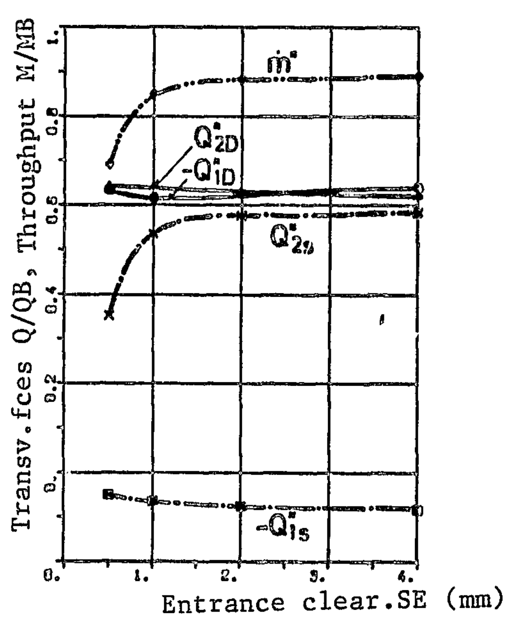

Figure 3.38 Clearance as in Fig. 3.37(A)

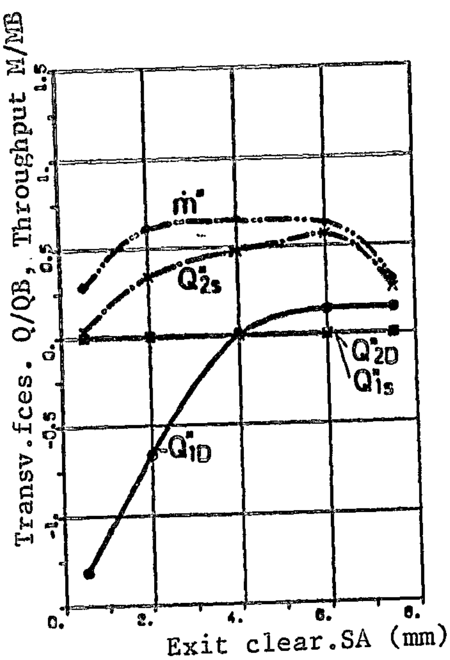

Figure 3.39 Clearance as in Fig. 3.37(B)

/102

In the case of clearance form B, the clearance of the radial exit - which in a turbine corresponds to the axial clearance - was changed simultaneously with the entrance clearance, as shown in Figure 3.39, above. The velocity difference Δc_u, which according to Table 3.6 determines the transverse forces arising out of the rotor blading's variable tangential force, is caused here by the tangential velocity behind the clearance. If the entrance or exit clearance is reduced, the clearance throughput will be lowered and this will lead to a decrease in the excitation force Q_{2s}. Because the afflux is parallel to the axis, the forces Q_{1s} and Q_{2D} vanish, since the pressure equalizing flow occurs in peripheral or tangential direction, symmetrically to the deviation. The transverse force Q_{1D} acts in the direction of the deviation for small exit clearances, since here the pressure distribution depends very strongly on the exit velocity. Assuming even larger pressure loss coefficients ζ^z at the elbows, a decrease in the restoration force occurs, which eventually disappears completely, if only pressure losses occur that are independent of the local clearance width.

While we have assumed, so far, that the tangential velocity of the main flow behind the clearance has no effect on the clearance flow, in Figure 3.40, below, we took into account a

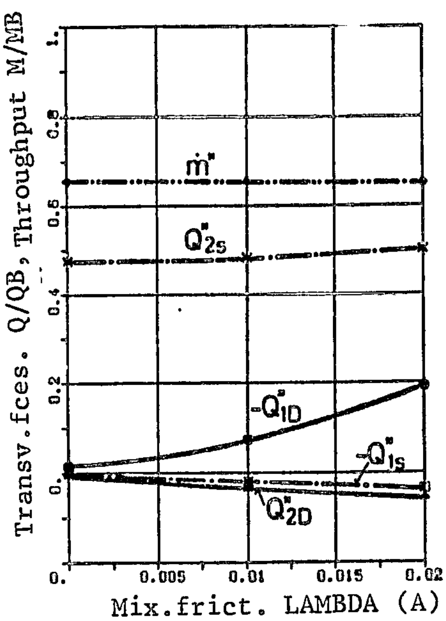

Parameters as in Figure 3.39
$s_E = s_A = 4$ mm
Figure 3.40 Clearance as in Fig. 3.37(B)

mixed friction force in the sense of section 3.3.4. It increases proportionally to the coefficient λ_A and causes an asymmetry in the clearance flow.

/103

Because of it, the force Q_{1s} and the excitation force Q_{2D} are additionally generated from the pressure distribution. Since under the assumptions stated the mixed friction force affects the clearance flow significantly only at the exit, its effect is relatively small. From this we may conclude that the excitation forces related to the pressure distribution are mainly generated at the rotor clearance of a turbine step. At the stator clearance, besides the excitation forces caused by the clearance loss, transverse forces are generated by the pressure distribution that may act against or even in the direction of the deviation, if we take a radial entrance or exit into account.

4 EXPERIMENTAL DETERMINATION OF THE TRANSVERSE FORCES ACTING ON THE ROTOR

In agreement with their definition, the individual coefficients of the matrix $\mathfrak{C}_S$ proportional to the deviation (see equation 2.3) can be determined by means of the measurement of the transverse forces acting at the turbine rotor, as a function of its static displacement. In contrast, the forces proportional to the velocity, in matrix $\mathfrak{D}_S$ can be determined only from a predetermined vibratory rotor movement. Kinetic tests (cf. Wohlrab, [30]) make it possible to study the simultaneous effect of all the coefficients of the matrices proportional to the deviation and to the velocity, from the fading of the disturbing vibration for known system damping. This study focuses only on the static method, which has the advantage - besides the separate determination of the forces proportional to the deviation - that the effect of a pressure distribution inside the seal clearance is relatively easy to investigate.

4.1. Test assembly

4.1.1. Installation construction

The transverse forces caused by the flow medium at a turbine stop are many times smaller than the rotor's inertia, representing at most 10% of the tangential force acting on the rotor. Since the clearances between rotor and housing are very small, special problems arise in the exact positioning of the rotor. The force measuring apparatus is arranged around the rotor in its stationary position; an eccentric positioning can be simulated by moving the housing.

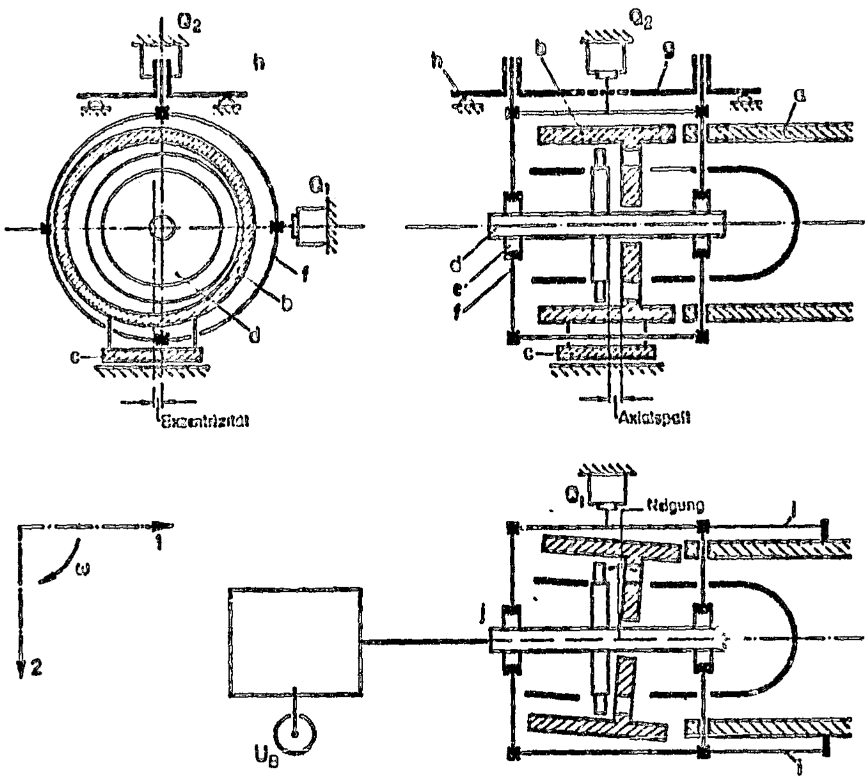

Figure 4.1 Test assembly schematic

Figure 4.1, above, shows a schematic representation of the arrangement chosen. From the fixed piping a, the fluid (air) streams into the housing b. This is placed on a twofold support c in such a manner that it can be displaced both in axial and in horizontal direction in relation to the stationary rotor. This makes it possible to vary the axial clearance between the /105 bladings, and the eccentricity of the rotor with respect to the housing. In an expansion of this arrangement, the housing b can also be rotated in the horizontal plane, making it possible to adjust the rotor's inclination with respect to the housing. The rotor d is held in the bearings e, whose retaining rings are fixed to the bar structure f. The latter connects the two bearing brackets and exits the housing without contact.

By means of pressure gauges Q_1 and Q_2, which in principle

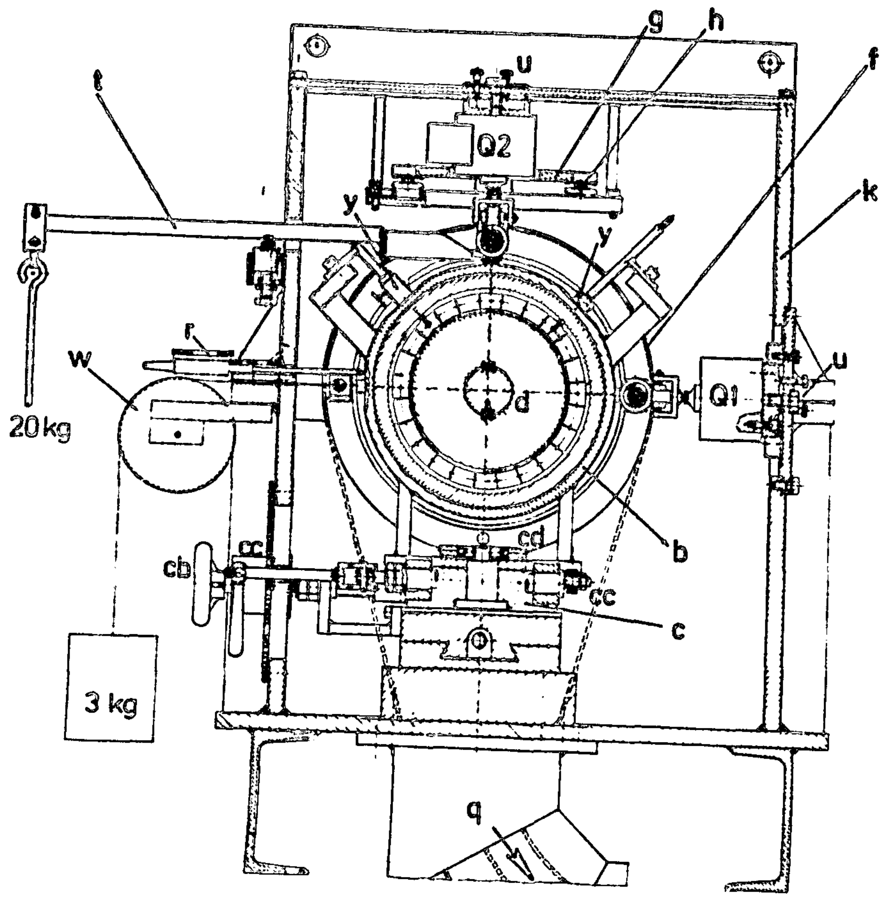

a Tubing b Movable housing c Moving mechanism: ca Axial clearance cb Eccentricity cc Inclination cd Clamping arrangement d Rotor e Bearings f Rod arrangement g Guide h Ball rollers i Axial prestressing j Coupling k Housing l Rubber grommet m Sealing for rod arrangemnt n Turbine step o Sheetmetal guide p Flow guide q Spent air r Dial gauge (housing position) s Longitudinal guide (Ball boxes) t Balance beam (Q2) u Dynamometer adjustment x Tachometer w Deviating roller y Position plane of housing z Measuring surfaces on rotor

Figure 4.2 Test installation

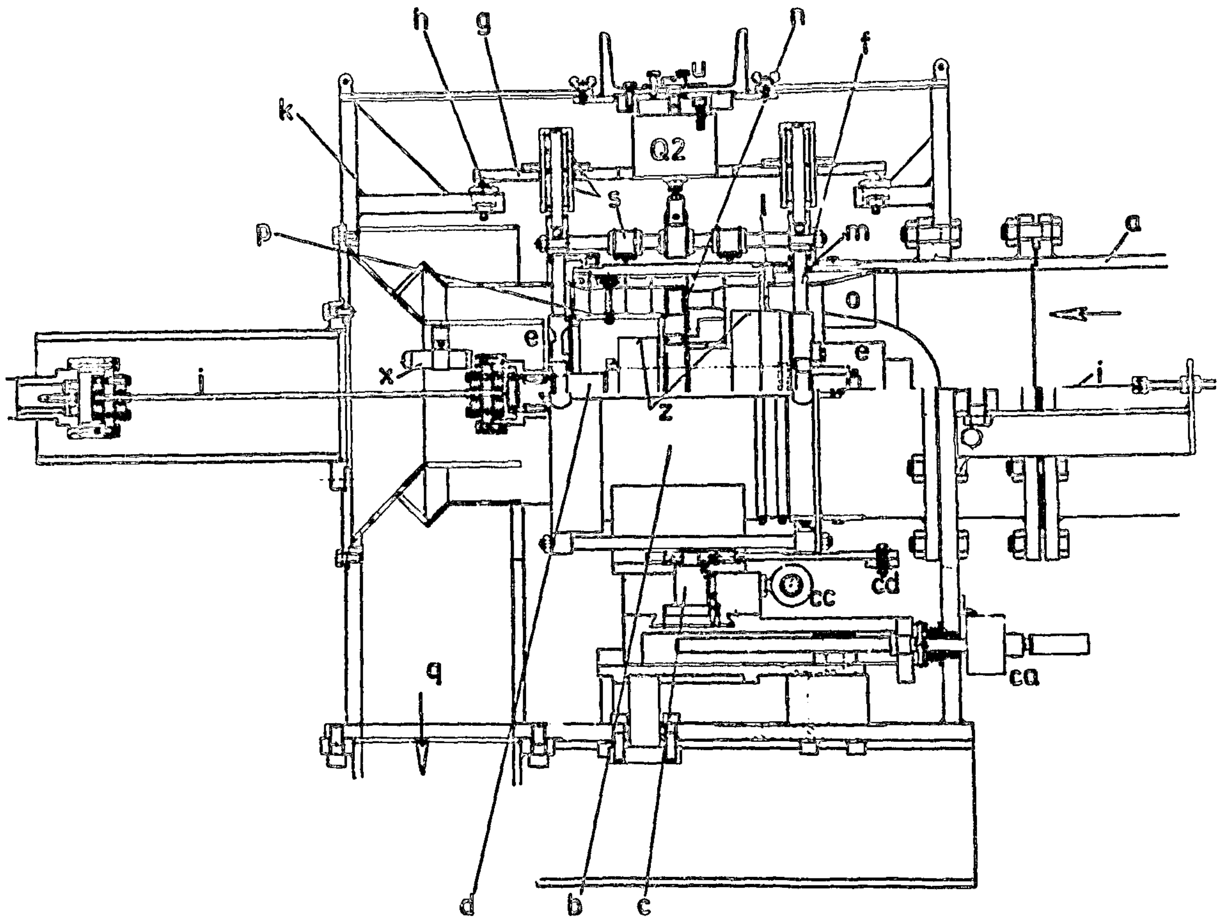

(to Figure 4.2, above)

are very rigid spring dynamometers, the bar structure is horizontally and vertically fixed. Moments acting through the bearing on the structure, on the one hand are picked up by the guide g, which is freely movable over ball rollers h. On the other hand, cables i, prestressed at location j, prevent rotation in the horizontal plane. In the coordinate system referred to the test apparatus, for a turbine rotating to the right, the excitation force is indicated at gauge Q_2 and the restoration force at Q_1. Through a bending coupling j, the rotor d is connected to a vibration generator, at which the tangential force U_B is measured. Force measurements at Q_1 and Q_2 are not affected by the coupling, since its spring rigidity is very low. In addition, such side effects are eliminated by calibration of the pressure gauges under actual conditions. The frictional moment of the turbine bearings is transferred to the guide g via the rod structure and hence can affect only the tangential force U_B, but not the force measurements at Q_1 and Q_2.

Figure 4.2, above, shows the test assembly built, with the construction elements a through j corresponding to the schematic on page 117. In order to relieve the vertical pressure gauge from a part of the rotor weight, a balance beam t provides a counterweight, through two ball-bearings, at the rod arrangement f. The pressure gauges are fixed to the rod arrangement through cross guides of two ball boxes each. The distance and the angle of the pressure gauges can be adjusted - by means of a tightening screw and three lifting screws u - in such a manner that all guide elements are perpendicular to each other. The longitudinal guides used permit a nearly frictionless rotor suspension, which is also free of play due to the prestressing applied. The central rotor d positioning with respect to the housing and that parallel to the axis, is established prior to assembly by means of four dial gauges and can be reproduced after assembly.

/109

4.1.2. Installation operation

The test turbine was operated on an open circuit, with the air supply being provided through the compressed air pipeline of the Technical University of Munich's heating power plant. Figure 4.3, below, shows a diagram of the plant, approximately to scale, with a schematic of the air supply lines.

A two-stage cell compressor a transfers the air through filter b into pressure tank c. From there, a pipeline (nominal diameter 80) leads through a restrictor d to the quick-acting gate valve e. After a long diffusor g with subsequent straightener, the air reaches the afflux tube (nominal diameter 230) to the turbine h. Together with the vibration generator k, they are mounted on a

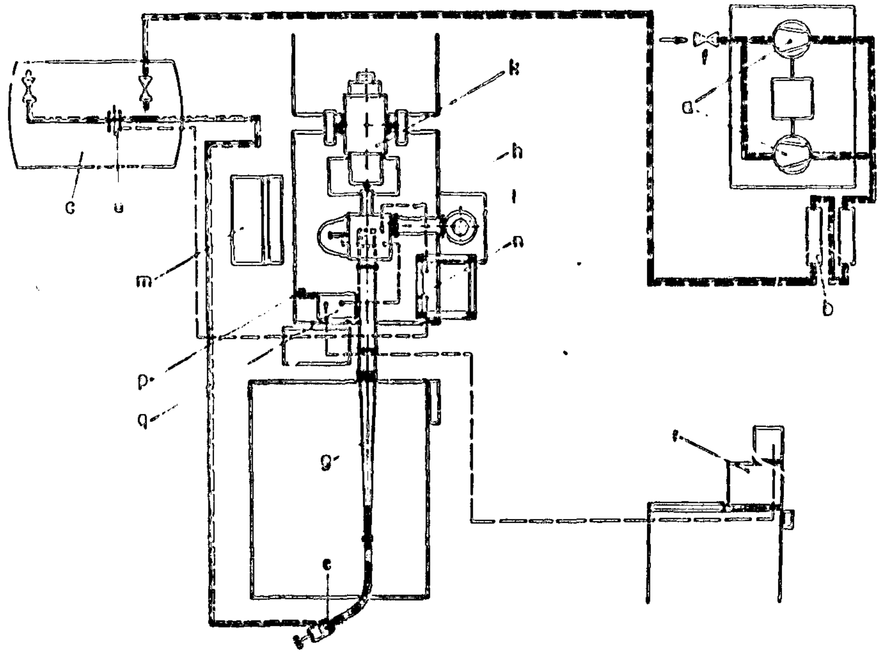

Figure 4.3 Arrangement of the installation

baseplate. The spent air is blown into the machine room via a /110 silencer. On one side of the control panel m are mounted the essential control elements for the test turbine h. The pressures are recorded at a U-tube wall n, and can be fotographed with a camera p, from the measuring site. The measurement amplifying and indicating instruments are located approximately at q. Shielded cables lead from there to a recording facility r equipped with selector switch, digital voltmeter and printer.

4.1.3. Measurement instruments and test method

The forces were determined by means of Hottinger pressure gauges, whose spring elements are outfitted with wire strain gauges. The table below provides a review of the gauges used and their spring rigidity, the possible measurement ranges - which are much larger than the forces actually measured at the facility. The precision is not affected hereby, since a

Force	Measurement range	Spring rigidity
Q_1	20 kp	800 kp/cm
Q_2	10 kp	350 kp/cm
U_B	50 kp	1600 kp/cm

calibration is always performed in the range indicated by the prestressing. Because of the relatively high pressure gauge spring rigidity a path change due to force interference can be disregarded. The wire strain gauges were balanced with a Wheatstone bridge and recorded on the indicator of a carrier frequency amplifier. Since due to the eccentric rotor vibration high frequency oscillations with large amplitudes are superimposed on the signals to be measured, the working range chosen for the amplifiers had to be very large. With a low-pass filter in line behind them and digital readout, it was possible to attain the required measurement precision.

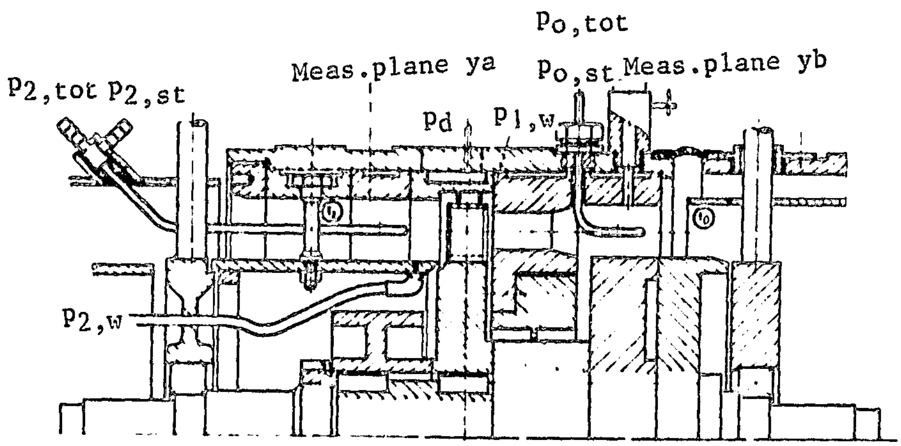

Figure 4.4 Test turbine longitudinal section with measurement points

Figure 4.4, above, shows the pressure measurement points on a longitudinal section of the turbine. The static pressure $p_{o,st}$ and the total pressure $p_{o,tot}$ ahead of the step are measured with two Prandtl-tubes, arranged rotated by 90°. The pressures $p_{2,st}$ and $p_{2,tot}$ behind the step are measured in the same /111 manner. For control purposes, several drill holes $p_{2,w}$ are made on the inside of the outflow channel wall. For standing blades, large underpressures were observed at this flow guide, due to the high exit velocity, which depending on the rotor's eccentricity, showed an uneven distribution along the perimeter. In order not to affect the measurement of the transverse forces with this additional effect, the flow guide was bolted to the housing. During some of the measurement series, an attempt was made to measure the pressure p_{1w} between the stator and the rotor, in a ring chamber above the rotor's covering. However, this was in part very imprecise, since the corresponding housing portions could not be sealed off in the manner desired. During tests with shroud band, the pressure distribution in the rotor clearance was measured using a maximum of 24 wall holes, $p_{d,1-24}$; their exact location and size is described in section 4.2.

All pressure measurements are performed with U-tubes, which are fotographed for fast and reliable recording. Figure 4.5, below, shows such a fotograph, for instance one taken in measurement sequence 115 (e = 0.7 mm). At the extreme left are the mercury columns for the restrictor pressures p_{B1}, p_{B2} and the pre-step /112 pressure $p_{o,st}$ of the turbine. Next to these, to the right, appear the pressure differentials in the two Prandtl tubes ahead and behind the turbine step. The pressure p_{1w} (center) had to be measured with a mercury column, here. To the right are collected the pressures p_d along the shroud band, whose single-arm manometer shows different levels for the labyrinth chambers K1, K2 and K3. The barometric pressure is recorded from an aneroid barometer b. Asides from this method of evaluation, the most important pressures were also recorded by means of the pressure sensors of the data acquisition system used, whose code number (at bottom) appears on every fotograph. However, because the

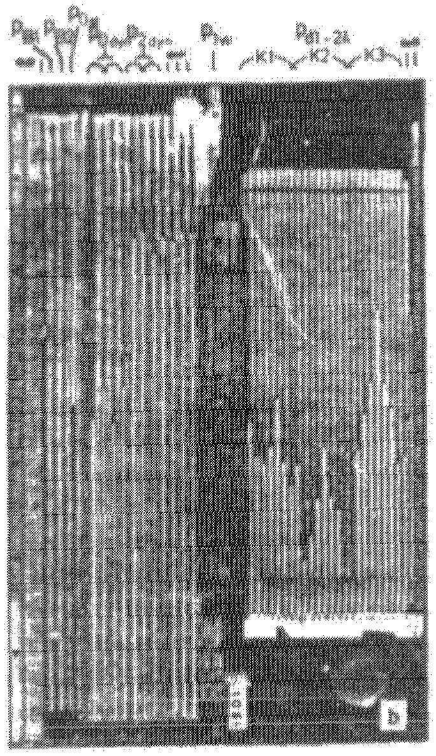

Figure 4.5 Pressure recording

measurement range of the pressure sensors was unsuited to the test facility, the evaluation was performed primarily with the photographic data.

The temperatures were measured by means of the corresponding iron-constantan thermoelements at the measurement orifice t_{B1}, as well as ahead and behind the turbine step - t_o, t_2 - and read on the digital voltmeter of the recording equipment. Since only stationary displacements are studied with the test installation, all paths could be measured with ordinary dial gauges at fixed housing parts; hence the precision of adjustment was usually of less than 0.01 mm. The arrangement of the measurement sites to determine the rotor position as either central or parallel to the axis, with respect to the housing - in pairs, displaced by 90° with respect to each other - was shown in Figure 4.4.

At the beginning of a test sequence, the static rotor was placed in the desired position with respect to the fixed housing parts, and the arrangement checked for freedom from friction. For a precise adjustment of the central position with respect to the movable housing, airflow was established across the step without rotation; hereby it was possible to reduce measurement errors caused by arrangement elasticity to a minimum. Once the dial gauges were removed, the rotor was brought to operating speed and the pressure gauges were calibrated using weights. It was then possible to change the housing position without modifying the operating conditions and record all forces, temperatures and pressures for each position. Thus a measurement sequence yields the variations in the transverse forces across the deviation and on the basis of repetitive measurements provides relatively precise average values for all turbine data. Within the precision of the measurements, these were independent of the eccentricity - or respectively, inclination - of the rotor.

4.2 Test program

The constant-pressure step represented in Figure 4.6, below, was used primarily to investigate the effect of the seal form on the clearance excitation forces. With the rotor suspension chosen, it was possible to measure simultaneously the forces acting in the direction of the deviation and perpendicularly to it; because of the test arrangement, the moments acting on the rotor were not included. Because of the non-variable compressor, the turbine throughput was fixed at approximately 0.4 kg/s. For an operating speed of 8,000 rpm, the pressure coefficient ψ was 5.2 to 6.2. The Reynold's numbers calculated from the afflux velocity and the blades' chord length was approximately $8 \cdot 10^4$.

From measurements performed with standing blades - listed completely in one report [5] - it was possible to derive

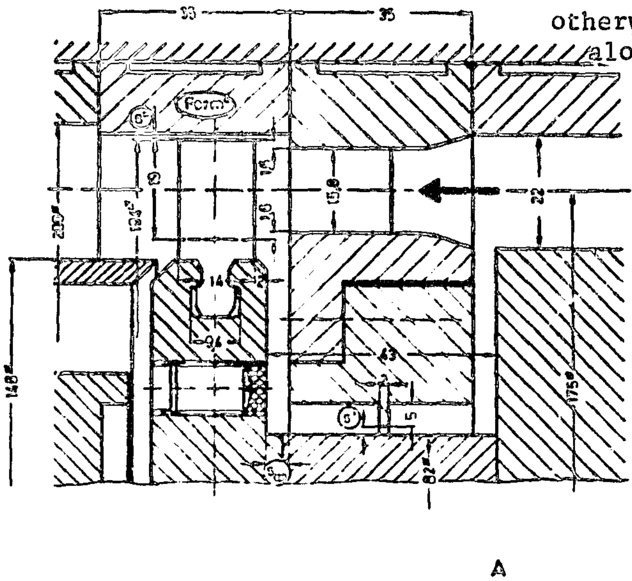

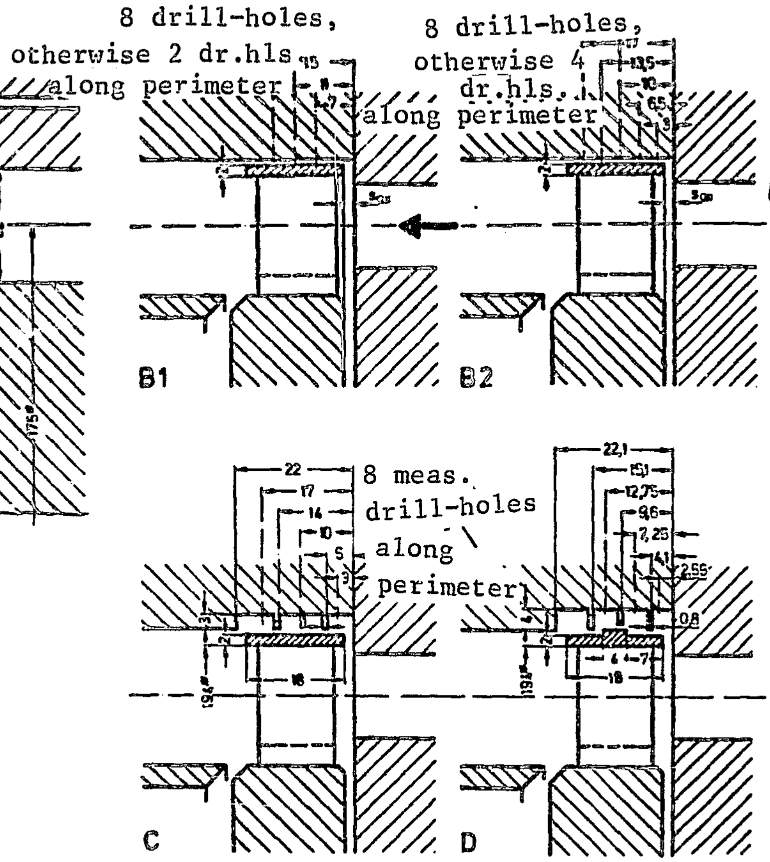

Figure 4.6 Constant pressure step geometry

Figure 4.7 Variations in the form of the seal

essential trends in the clearance excitation forces, which also served as orientation for the remainder of the test program. Because they are more applicable, we shall mention here only tests with rotating blading, which are in agreement with the /115 measurements above, once differences in operating conditions are taken into account.

The seal geometry was varied by placing certain inserts in the turbine housing, shown in Figure 4.7, above, for blading with shroud band. Table 4.1, below, provides an overview of the sequentially numbered insert conditions, indicating the characteristic magnitudes. The variations in the radial

TABLE 4.1 Test program

Insertion condition EB		Geometry s'	s"	Form"
21	w/o shroud-band	1,1	1,0	A
22	w/o shroud-band	1,55	1,5	A
23	w/o shroud-band	0,55	0,5	A
24, 25	plain shroud-band	1,1	1,0	B1
28	plain shroud-band			B2
26, 27	two seal peaks	1,1	1,0	C
29	three seal peaks	1,1	1,0	D

clearance widths were performed only for blading without shroud band (form A); for reasons of tolerances, the stator clearance was slightly larger than that for the rotor. Since distinct pressure differences could already be observed along the rotor shroud band for standing blading, special attention was paid to banded blading. First, the plain clearance was investigated with a simple gauge ring B1, for different operating speeds. However, the pressure drop in axial direction could be measured more accurately only after adding a second gauge ring, B2. To conclude the test program, two labyrinth seals commonly used with turbines (C and D) were installed at the rotor. In addition, this made it possible to study the effect of rotor inclination with respect to the housing.

/116

4.3. Measurement evaluation

4.3.1. Turbine data and force measurements

The turbine's mass flow is determined from the temperature at the measurement orifice, t_{B1}, and the pressures p_{B1} and p_{B2}, according to DIN* 1952

$$\dot{m} = \alpha \, \varepsilon \, m \frac{\pi}{4} D^2 \sqrt{2 \varrho (p_{B1} - p_{B2})}. \qquad (4.1)$$

The pipe diameter is given as D = 80 mm and the opening ratio of the orifice as $m = d^2/D^2 = 0.366$. The density ρ can be calculated from the gas equation, as a function of temperature at the orifice. The expansion coefficient $\varepsilon(p_{B2}/p_{B1}, m)$ and the throughput coefficient $\alpha(Re, m)$ were determined from DIN 1952, taking into consideration the temperature dependence of the kinematical viscosity for Reynold's number. Because of the dependence of Reynold's number on the mass flow, iteration is necessary.

The turbine's isentropic gradient is obtained from the pressures $p_{o,st}$, $p_{2,st}$ and the temperature T_o, by

$$\Delta h_s = c_p T_o \left[1 - \left(\frac{p_2}{p_0}\right)^{\frac{\kappa-1}{\kappa}}\right] \qquad (4.2)$$

The force U_B at the brake's lever arm l_b is first recalculated using the calibration factor of the gauge, then the turbine step's tangential force

$$U = \frac{l_b}{d_m/2} U_B \qquad (4.3)$$

is determined. With the angular velocity ω at the rotor, we obtain the effective efficiency

$$\eta_e = \frac{U \omega \, d_m/2}{\Delta h_s \, \dot{m}}. \qquad (4.4)$$

DIN = Deutsche Industrie-Norm = German Industrial Standards

Correspondingly, the internal efficiency can be calculated from the temperatures T_0 and T_2 (ahead of and behind the step):

$$\eta_i = \frac{c_p(T_0 - T_2)}{\Delta h_s} \qquad (4.5)$$

/117

From the tangential velocity $u = \omega \cdot r$ we can now calculate the reference quantity U_s - from equation (2.12) - for the measured excitation forces. To determine the theoretical excitation forces requires knowledge of the step's triangle of velocities. From the mass flow $\dot{m}_0$, the surface A_0 and the density ρ_0, we obtain the afflux velocity at the stator blading,

$$c_0 = \frac{\dot{m}}{A_0 \varrho_0}. \qquad (4.6)$$

According to Traupel [14], the blading efficiencies can be taken as $\eta' = 0.89$ and $\eta'' = 0.82$ for the existing step. From the energy equation we obtain the stator exit velocity

$$\frac{c_1^2}{2} = \eta'\left(\Delta h_s' + \frac{c_0^2}{2}\right) \qquad (4.7)$$

as a function of the stator blading's isentropic gradient

$$\Delta h_s' = c_p T_0 \left[1 - \left(\frac{p_1}{p_0}\right)^{\frac{\varkappa - 1}{\varkappa}}\right]. \qquad (4.8)$$

An iterative solution is possible for the pressure p_1, if the stator's exit surface $A_1 \sin \alpha_1$ has been very precisely determined, for instance through measurements of the individual channel widths. From the continuity equation we now calculate the velocity

$$c_1 = \frac{\dot{m} - \dot{m}_{sp}'}{A_1 \sin\alpha_1 \varrho_1}, \qquad (4.9)$$

and the density from the gas equation, as a function of the turbine condition

$$\frac{\rho_1}{\rho_0} = \frac{p_1}{p_0}\,\frac{T_0}{T_1}. \tag{4.10}$$

The temperature T_1 can be calculated from the energy equation for the stator blading,

$$\Delta h' = c_p(T_0 - T_1) = \Delta h_s'\,\eta' + \frac{c_0^2}{2}(\eta' - 1) \tag{4.11}$$

From (4.10) we now obtain the density ratio

$$\frac{\rho_1}{\rho_0} = \frac{p_1}{p_0}\,\frac{1}{1 - \frac{1}{c_p T_0}\left(\Delta h_s'\,\eta' + \frac{c_0^2}{2}(\eta' - 1)\right)}. \tag{4.12}$$

/118

If herefrom we now calculate the velocity c_1 from equation (4.9) and replaces this value in the energy equation (4.7), then we obtain, with (4.8), the initial equation for the pressure p_1,

$$\frac{1}{2}\left(\frac{\dot m - \dot m'_{sp}}{A_1 \sin\alpha_1\,\rho_0}\right)^2 \left(\frac{p_0}{p_1}\right)^{\frac{2}{\varkappa}} \left[(1-\eta')\left(1 + \frac{c_0^2}{2 c_p T_0}\right)\left(\frac{p_0}{p_1}\right)^{\frac{\varkappa-1}{\varkappa}} + \eta'\right]^2 = \eta'\left[c_p T_0\left[1 - \left(\frac{p_1}{p_0}\right)^{\frac{\varkappa-1}{\varkappa}}\right] + \frac{c_0^2}{2}\right]. \tag{4.13}$$

If we solve the right-hand side for p_1, an estimated value $\bar{p}_1$ can be improved by iteration. We then obtain the step's percentage reaction

$$r = 1 - \frac{\Delta h_s'}{\Delta h_s}. \tag{4.14}$$

However, the result of this calculation strongly depends on the surface $A_1 \sin\alpha_1$ and the stator's exit angle contained in it.

Disregarding the stator clearance loss in equation 4.9 yields a much lower percentage reaction for the existing test step, while for loss-free flow ($\eta' = 1$) there is an increase again. Since the two effects approximately cancel each other, all further measurements - considering the possibility of further sources of error - were performed assuming $\eta' = 1$ and $\dot{m}_{sp} = 0$. It was observed, in addition, that even small changes in the throughput or the turbine's pressure gradient had a large effect on the percentage reaction, following the above calculations. However, the latter is needed in the theoretical determination of the pressure distribution across the shroud band and hence also impairs the comparison between theory and measurements.

With the known pressure p_1 we obtain the velocity c_1 from equation (4.7) and the complete triangle of velocities

$$\left.\begin{aligned} w_1^2 &= c_1^2 + u^2 - 2uc_1\cos\alpha_1 ,\\ w_2^2 &= \eta'(2\psi\Delta h_s + w_1^2) ,\\ c_2^2 &= w_2^2 + u^2 - 2uw_2\cos\beta_2 ,\\ \alpha_2 &= \arctan\frac{w_2\sin\beta_2}{w_2\cos\beta_2 - u} , \end{aligned}\right\} \qquad (4.15)$$

/119

as a function of the tangential velocity and the angles indicated in Figure 4.6. We thus obtain the peripheral efficiency

$$\eta_u = \frac{u(c_1\cos\alpha_1 - c_2\cos\alpha_2)}{\Delta h_s} \qquad (4.16)$$

for the step, assuming $c_0 = c_2$. Furthermore, the abscissa values for Figure 2.7 can be given, to facilitate calculation of the theoretical excitation constants from equation (2.15). Since no equations are given in [14] for the clearance loss for plain clearances, as an approximation to it we used the value for a single seal peak.

In each measurement sequence, the calibration factors for the pressure gauges were determined first, by linear regression on the electrical readings obtained for different calibration weights. After recalculation of the measured transverse forces, their increases $\underline{q}$ across the deviation $\underline{e}$, or respectively, $\underline{a}$ were calculated by linear regression. For better applicability of these results, in conformance to the theory (see equation (2.16)), these increases are related to the ratio between the isentropic tangential force and the rotor "bucket" length. We thereby obtain the so-called clearance excitation and restoration coefficients K_1 through K_4, which describe the step's transverse forces, in a dimensionless form. The most important operating parameters and measurement results here discussed for the test turbine, are compiled for selected measurement sequences in tables in the Appendix.

4.3.2. Relationship between excitation forces and efficiency measurements

The measurement of the clearance loss can be accomplished indirectly, via the efficiency $\eta_i = \eta_u - \zeta_{sp}$, where the peripheral efficiency is determined neglecting the additional losses due to extrapolation to radial clearance width s = 0. Since the excitation forces are very sensitively affected by efficiency variations, exact measurements are necessary, for many radial clearance widths. It hence seems appropriate to proceed inversely, i.e., to establish comparisons to efficiency variations based on the many excitation force measurements available. It can be shown at least for blading without shroud band that the efficiency varies non-linearly with the radial clearance width. This can be taken into account by means of a polynomial of the clearance loss

$$\zeta_{sp} = a_1 s + a_2 s^2 + a_3 s^3 \qquad (4.17)$$

as a function of the clearance width. If we assume, disregarding equalizing flows, that this clearance loss is valid also for local radial clearance widths $\tilde{s}$ according to equation (2.14), then the integration of equation (2.10) yields the transverse forces acting on the rotor,

$$\left.\begin{aligned} Q_{1s} &= 0, \\ Q_{2s} &= \frac{U_s}{2}\left[\left(a_1 + 2a_2 s + 3a_3 s^2\right) e + \frac{3}{4} a_3 e^3\right]. \end{aligned}\right\} \qquad (4.18)$$

Since the clearance loss was assumed proportional to the local clearance width, the force in the direction of deviation vanishes. While for a linear equation $a_2 = a_3 = 0$ - as we already established - the force is independent of the radial clearance width $\underline{s}$, this effect can already be noticed for a parabolic equation $a_3 = 0$. However, it is only for higher-order clearance loss equations that an "s"-shaped course of the excitation force across the eccentricity is obtained.

If we assume that the excitation forces Q_{2D} caused by pressure distributions can be disregarded for bladings without shroud band, then the coefficients of equation (4.18) can be determined by the least squares method applied to the measured excitation forces $Q_2 \approx Q_{2s}$. Here we obtain a family of curves of the excitation forces as a function of radial clearance width $\underline{s}$, across the eccentricity, whose coefficients determine the course ζ_{sp}^{Q} of the clearance loss that would result as a consequence of the excitation forces. By further adapting this course to the measured efficiency

$$\eta_i = \eta_u - \zeta_{sp}^{Q} \gamma_Q \qquad (4.19)$$

we can determine the peripheral efficiency η_u and a factor γ_Q by which the clearance loss ζ^Q_{sp} from the excitation force measurements would have to be corrected. For $\gamma_Q = 1$, there would be complete agreement (see Figure 4.8, below) between excitation

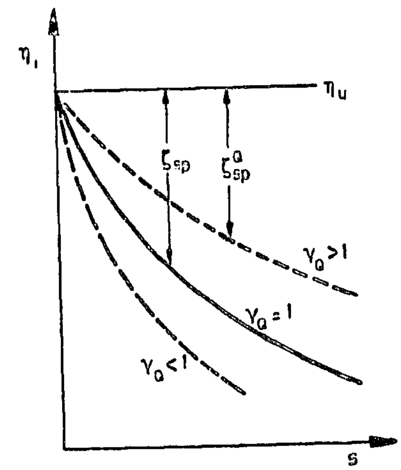

Figure 4.8 Variation of the effciency across the radial clearance width

force and efficiency measurements. For $\gamma_Q < 1$, the measured excitation forces are larger than the forces that can be explained based on the clearance loss, which leads to the conclusion that there are additional effects, for instance due to the pressure distribution, at work. In general the factor will be $\gamma_Q > 1$, since the local clearance loss can be reduced by means of equalizing flows along the perimeter. In this case the measured excitation forces are smaller than those one would calculate from a precise course of the efficiency $\eta_i(s)$.

It was assumed, in the evaluation of the results, that the effective efficiency determined from output measurements at the electric dynamometer are to be set equal to the internal efficiency, $\eta_i = \eta_e$. The measurement of the internal efficiency from the temperatures ahead of and behind the turbine is affected by measurement errors that are too large, for these considerations. But it is to be expected that the friction at the test turbine's ball bearings will affect the efficiency η_e in the same manner for all parameter changes.

Especially important to the above correlation is the assumption that viewed across the perimeter, the smallest clearance loss will also occur at the narrowest clearance width. Because of the torsional effect on the flow, according to section 3.6 this will not always be true. As Figure 4.9, below, shows, a small phase displacement occurs also because the clearance loss occurring /122

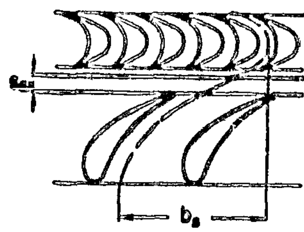

Figure 4.9 Flow-line course

at the stator reduces the tangential force only after an arc length b_s. Because of this, in contrast to equation (4.18) there are transverse forces Q_{1s} active here that must be taken into account, in the correlation with the efficiency variations. The measured restoration forces Q_1 however point towards the fact that in spite of the relatively large flow-line advance (ψ_s = $2b_b/d_m \approx 17°$) this effect is small.

4.3.3. Pressure distribution at the shroud band

The purpose of the pressure measurements at the rotor seal clearance is the determination of the forces arising there. Integration of a pressure curve along the perimeter ψ and in axial direction $\underline{z}$ presupposes a two-dimensional function $p(z, \psi)$ at the rotor surface. Assuming that the pressures measured at the housing wall are constant across the local clearance width, this function can be determined from a limited number of measurement points. For the axial direction it is assumed - for a plain clearance - that in conformance to Figure 4.10, below,

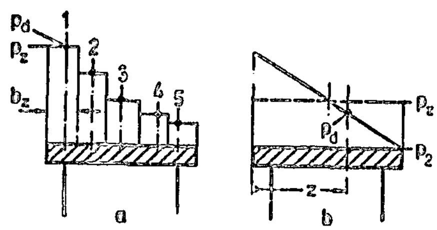

Figure 4.10 Evaluation of measured pressure curves

the measured pressures p_d correspond to the average values across the widths Δz; for a labyrinth, instead, constant pressure may be assumed along the chamber width. On this base it is possible to calculate the compressive forces acting on the rotor as was done in section 3.4. Since in the peripheral direction a maximum of only eight measurement points is available for a pressure curve $p(\psi)$, it is described by means of three Fourier coefficients from equation (3.55). This corresponds /123
to the fitting of a sinusoidal function of variable amplitude, with phase displacement with respect to the course of the local clearance width; it will be recorded with the measurement values submitted later.

Based on the assumptions regarding the course of the pressure curve, the forces determined from it could be subject to systematic error. Despite some deviations, the prescription of a sinusoidal pressure curve in the tangential or peripheral direction appears to lead to only small errors, since higher order Fourier coefficients (equation (3.54)) drop out during integration. In contrast, the result is severely affected by how the widths Δz in Figure 4.10 are established, since the pressure curve is non-linear in axial direction. It would be possible in principle to fit a two-dimensional function $p(z,\psi)$ to the measurement points, but it would lead to substantial calculation efforts, since the parameters would no longer be independent of each other. This would make restrictions necessary such that no increased precision in the results could be expected, in comparison to the above evaluation. Qualitatively, moreover, measurements with only one measurement plane perpendicular to the carrying axis (cf. Figure 4.10b) yield useful results.

Within a measurement sequence, the pressure variations are recorded for each eccentricity and the forces Q_D are computed, from whose course across the eccentricity the increases q_D are calculated by linear regression. Whether the rotor is displaced in a positive or a negative direction (cf. Figure 2.5), for a corresponding definition of the tangential angles the same pressure curves should be obtained. However, due to minute differences in the seal's microgeometry, in part substantial deviations can occur. Therefore, in order to obtain representative descriptions of the pressure course, pressures for equally large positive and negative eccentricities are averaged.

/124

4.4. Transverse forces from an eccentric rotor position and comparison to the efficiency curve

Starting from the central position of the turbine step within the housing, the eccentricity could be adjusted to up to 75% of the radial clearance width, in both directions. The transverse forces acting on the rotor were measured at 15 points, within this range; the course of the forces was approximately linear across the deviation (cf. [5]), for all parameter combinations here investigated. The pressure gradient at the turbine occurred as a function of the throughput, which was fixed because the compressor could not be varied. Correspondingly, similar test conditions are best differentiated for equal throughput, which is recorded in the Appendix, together with other measured turbine step parameters. However, the necessarily somewhat different turbine operating conditions had only little effect on the consideration of the dimensionless slopes K_1 through K_4 of the forces across the deviation.

4.4.1. Blading without shroud band

Figure 4.11, below, shows the clearance excitation coefficients determined from force measurements for rotor blading

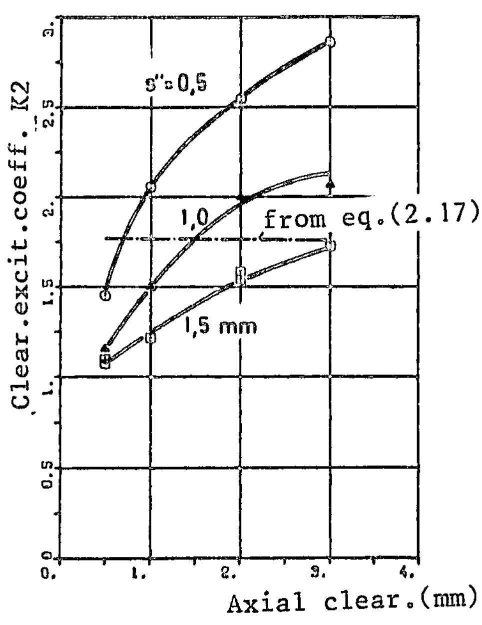

Figure 4.11 Rotor without shroud-band

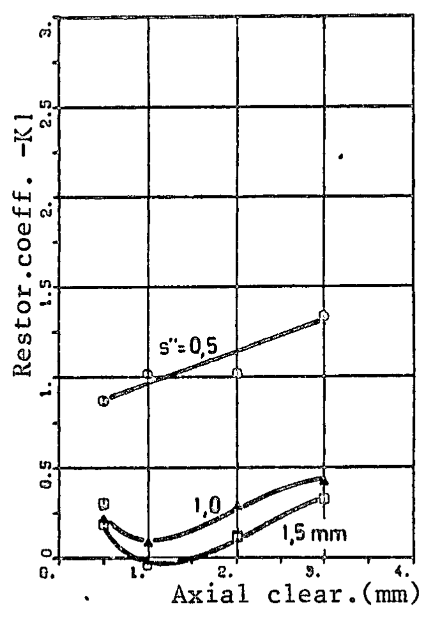

Figure 4.12 Rotor without shroud-band

without shroud-band. For the turbine step investigated, the clearance loss increases as the axial clearance increases, thereby causing an increase in the clearance excitation coefficients K_2. In contrast to the linear theory of equation (2.17), they depend strongly on the radial clearance width. The restoration coefficients $-K_1$ shown in Figure 4.12, above, increase from an axial clearance s_{ax} = 1 mm on, which can be attributed to the flow line displacement illustrated in Figure 4.9, or to differences in the pressure distribution in the stator clearance. We can not state here, with any certainty, whether these restoration forces - which according to equation (2.15) should vanish - are caused by stator or rotor clearance losses. Such a statement is possible only if the housing portion of the rotor clearance can be displaced independently from that of the stator, eccentrically to the rotor (cf. [30]). For a /125 very small axial clearance there may be a finite value for the restoration coefficient, which could be measured somewhat more clearly during tests with standing blading [5]. For this extreme position of the rotor with respect to the housing, due to the step's construction there will be a clearance loss only at the rotor blading, which according to equation (2.15) should not give rise to restoration forces. It is thus not impossible for transverse forces to be caused by a non-uniform pressure distribution along the perimeter, even for blading without shroud-band.

In order to explain the relatively large deviations of the measured clearance excitation coefficients in Figure 4.11 from those expected in theory, we performed a correlation between the excitation forces and the measured efficiencies, in accordance with section 4.3.2. Figure 4.13 below, shows the course of the thus referenced excitation forces for various radial clear- /126 ance widths, across the eccentricity. The family of curves plotted corresponds to the function (4.18), whose parameters

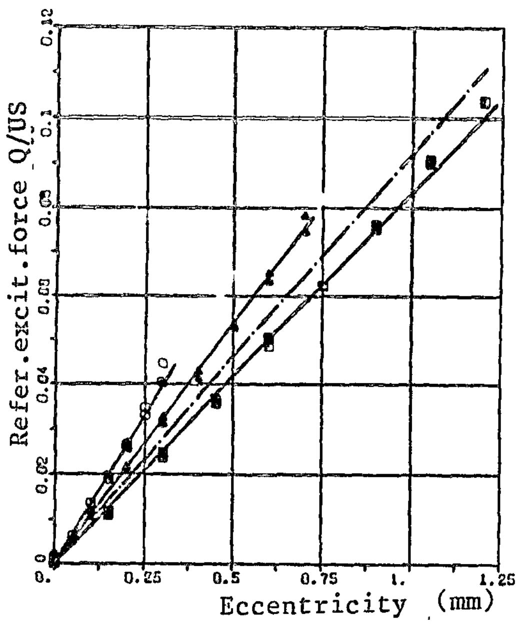

Figure 4.13 Blading without shroud-band
Curve fitted w/2nd
order polynomial for clearance loss
from clearance loss,[14],eq.(2.15)

were determined from the measurement points, by linear regression, as a function of the two variables e and s. Since the course of the excitation forces is linear across the eccentricity, a second order polinomial (4.17) will be sufficient for the clearance loss. However, a higher-order polinomial was able to explain measurements for a standing rotor [5] very well, even though there the course of the excitation forces is non-linear across the eccentricity, characterized by a steeper slope for increasing eccentricity.

It is possible to establish a comparison between the parameters of the functions (4.18), determined from excitation force measurements, and the measured efficiencies, for all axial clearances investigated. Starting from the calculated peripheral efficiency (for s = 0), the broken straight line records the course of the clearance losses from [14], which for this turbine

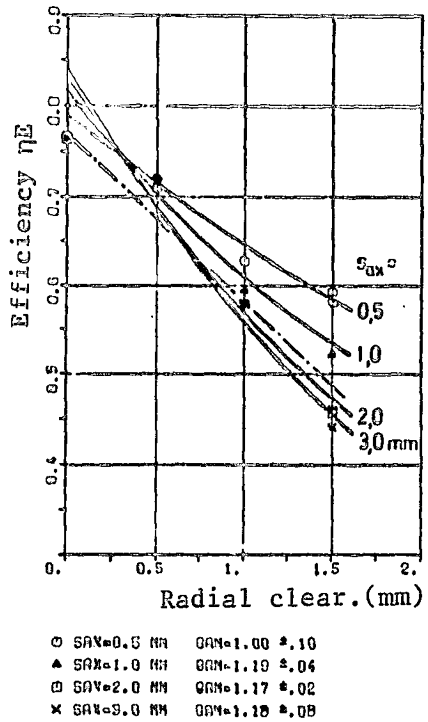

Eff.curve from excit.fce.measurement,
2nd order polynomial fit
-·-From clearance loss, [14]

Figure 4.14 Blading without shroud-band

step agree only very little with the measurements. The slope and curvature of the curves plotted were determined for each axial /127 clearance from the measured excitation forces. If together with equation (4.19) we were to introduce a correction factor $\gamma \approx 1.2$, the agreement between these curves and the measured efficiency would improve. In other words, the excitation forces are only 83% of the forces one should calculate, from the actual course of the efficiencies. Taking into consideration the certainty required for vibration calculations, the excitation forces in bladings without shroud-band can be calculated from a known efficiency curve, using equations (2.16) or (4.18).

4.4.2. Blading with shroud-band

In order to reduce clearance losses, the blading is fitted with

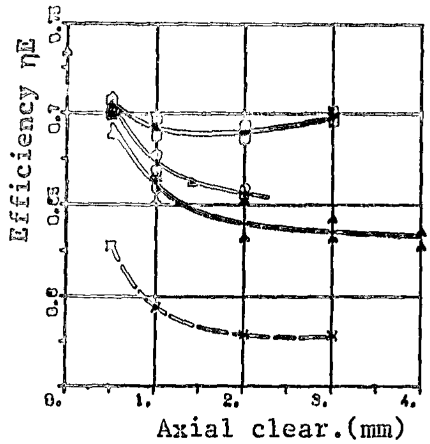

o Plain shroud-band (EB 25, 28)
▲ Two seal-peaks (EB 26, 27)
▫ Three seal-peaks (EB 29)
-- w/o shroud- band (EB 21)

Figure 4.15 Effect of the clearance form

shroud-bands. Figure 4.15, above, shows the course of the measured efficiencies for equal radial clearance widths, as a function of the axial clearance. The efficiencies are significantly improved with respect to blading without shroud band. The recessed labyrinth with three peaks is the most favorable: here the seal effect of the radial clearance is little affected by variations in the axial clearance. Due to the smaller clearance losses, smaller clearance excitation forces are to be expected for banded blading. Figure 4.16, below, /128
shows however that the clearance excitation coefficients are much larger than for blading without shroud-band. As shall be explained in section 4.5, because of a pressure distribution that varies along the perimeter, in the rotor clearance, the measured forces are approximately twice as large as those calculated from equation (2.17) from the clearance loss only. With increasing axial clearance the clearance excitation /129
coefficients become larger; there is a qualitative relationship to the efficiencies of Figure 4.15. Because for increasing clearance loss - i.e., smaller efficiency - the clearance excitation coefficients become larger in the same manner. However, an exact correlation between the excitation forces and

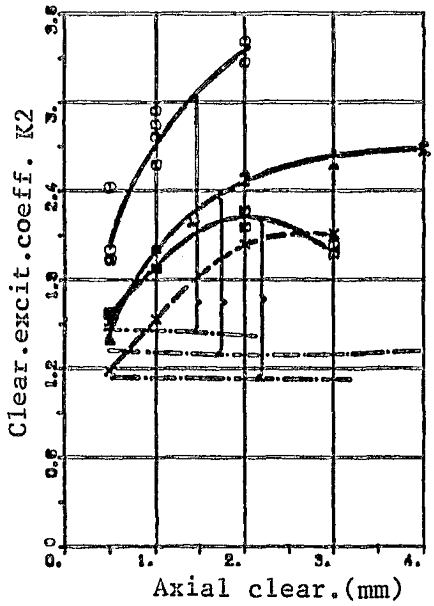

• Plain shroud-band (EB 25+ 28)
▴ Two seal-peaks (EB 26+27)
▪ Three seal-peaks (EB 29)
-·- From clear.loss, eq. (2.17)

Figure 4.16 Effect of the clearance form

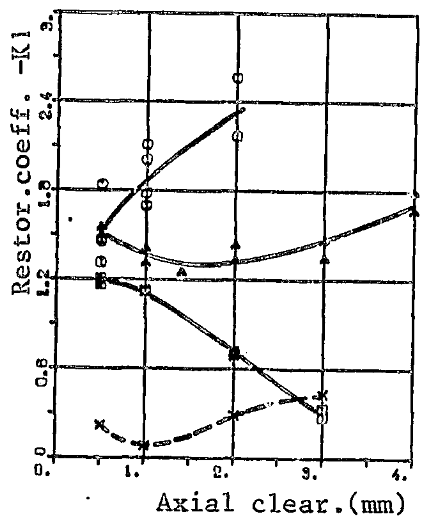

○ Plain shroud-band (EB 25+28)
▴ Two seal-peaks (EB 26+ 27)
□ Three seal-peaks (EB 29)

-- w/o shroud-band (EB 21)

Figure 4.17 Effect of the clearance form

the efficiencies is possible only, when the dependence of the curve on the radial clearance width is known. Figure 4.17, below, shows the restoration coefficients across the axial clearance, which depend strongly on the form of the rotor clearance. For a plain rotor clearance, the restoring forces are largest and can be primarily attributed to a pressure distribution over the rotor shroud-band, as the comparison to blading without shroud-band shows.

4.5. Pressure distribution over the rotor shroud-band and comparison with theory

4.5.1. Shroud-band with plain clearance

Figure 4.18 shows a two-dimensional representation of the

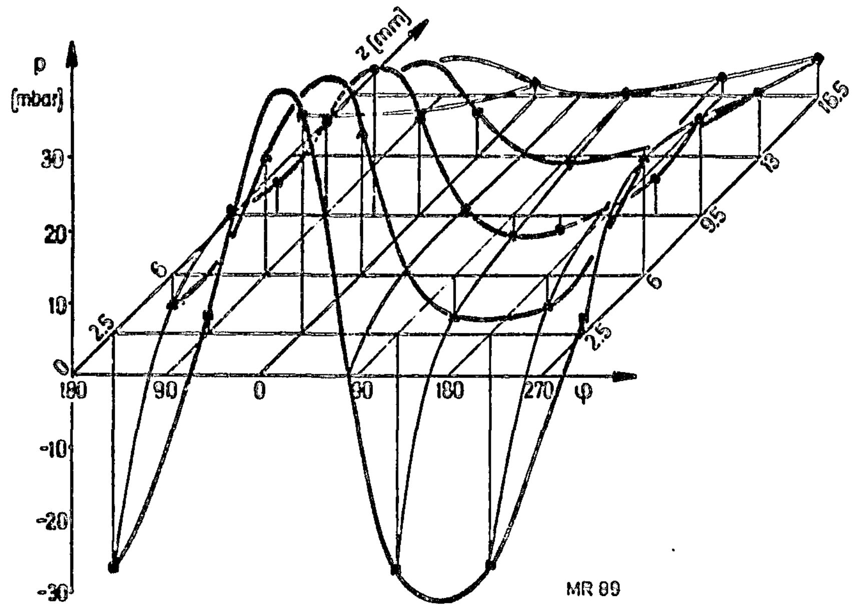

Figure 4.18 Pressure distribution across a plain shroud-band, e = 0.7 mm

pressure course, measured for an eccentricity of 0.7 mm at a plain rotor clearance, both along the perimeter and in axial direction. The static pressure drop at the rotor blading's external section was approximately 60 mbar, in this measurement sequence (cf. Appendix), with an afflux velocity of 140 m/s. Starting from the entrance edge (z = 0; cf. Figure 2.8), the pressure courses for five measurement planes normal to the axis, in accordance with Figure 4.7 (B2), are shown along the shroud band; the axial direction was considerably magnified in comparison to the perimeter. The clearance at the entrance side of the shroud-band here is only half as large as the average radial clearance width. In agreement with the definition in Figure 2.5, the smallest local radial clearance width is found at the tangential angle ψ = 0. Because the flow is subjected to

torsional effects, there is a pressure maximum just before the narrowest clearance, which for individual measurement planes along the shroud-band travels almost 80° against the direction of rotation. Due to the characteristic pressure maximum in 130
front of the narrowest clearance, a force acts on the rotor that has a component in the direction of the deviation, and another one perpendicular to it. In tangential direction the pressure curve does not correspond to a pure sine function, since the maxima are steeper than the minima.

Figure 4.19, below shows, for three selected measurement sequences, the effect of the axial clearance on the measured pressure courses, with the fitted sine function plotted in each case. Measurement sequences 90 and 93 are only qualitatively comparable to sequence 89, already in axonometric representation. Because of a defective seal, the turbine's throughput and hence also the pressure and the velocity in front of the clearance were much smaller, as can be seen from the recorded pressure P1 of the central section.

/132

To calculate the theoretical pressure courses - also plotted on Figure 4.19 - the pressure and the velocity were recalculated, from the turbine step's central section to the entrance radius, using the potential vortex law (cf. section 3.2.1.). The loss coefficients introduced in section 3 to describe the clearance flow affected by torsional forces, were used; their effect has already been thoroughly investigated by means of test calculations. The radial clearance was subdivided in the flow direction in such a manner that the pressure courses represented are valid for the position of the measurement planes. In addition, we plotted the course of the throughput - variable along the perimeter - and for small axial clearances, the course of the pressure at the end of the radial entrance. Due to the manner of construction of the seals studied, the radial exit can be ignored.

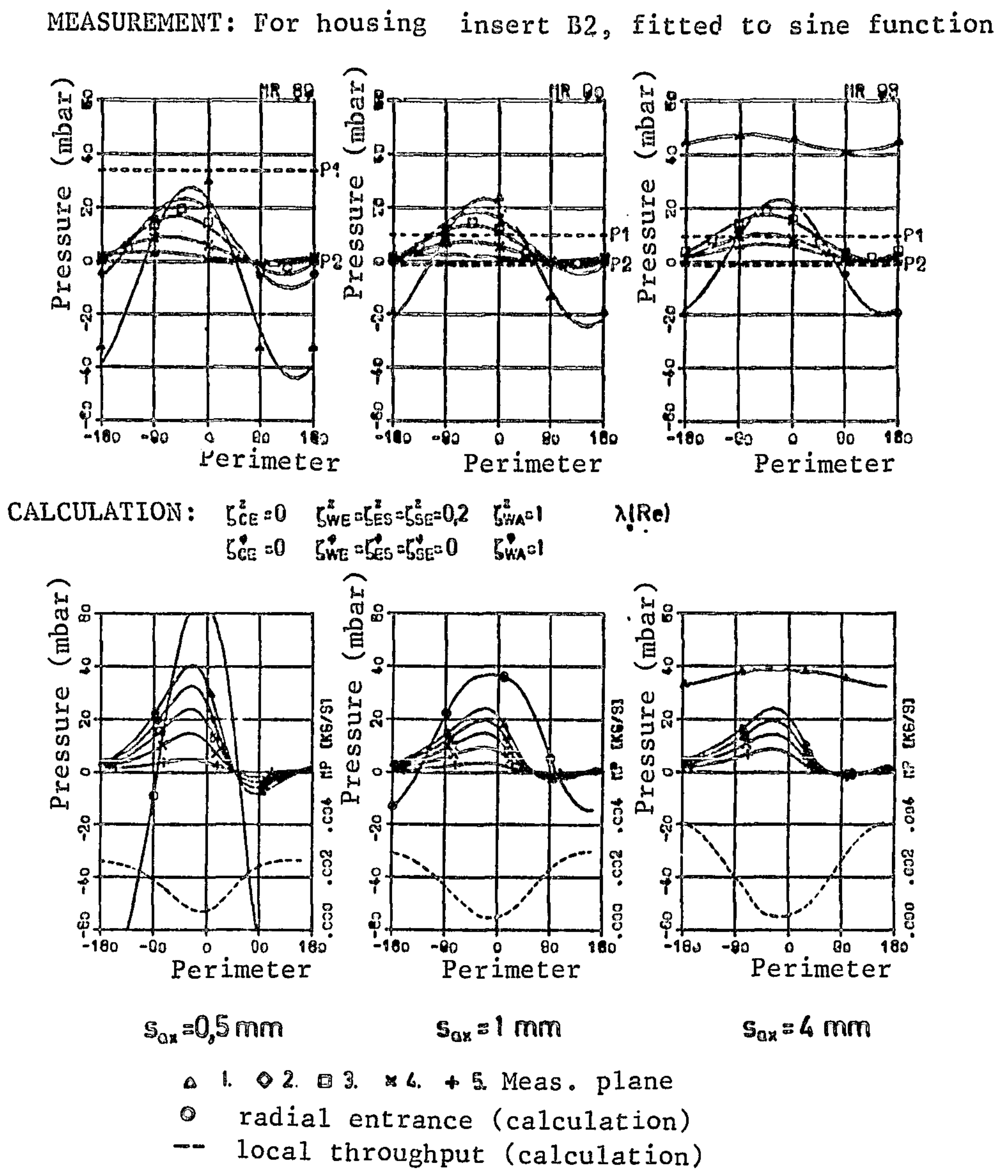

Figure 4.19 Pressure distribution for a plain rotor clearance, for various axial clearances

When the axial clearance is changed, it must be remembered that from Figure 4.7, simultaneously the position of the measurement drill-holes with respect to the shroud-band is displaced. For the gauge ring B2 considered here, with five holes perpendicular to the axis, one can obtain for s_{ax} = 4 mm, for instance, the interesting special case in which the drill-holes of the first plane are already over the radial entrance. In agreement with theory, we obtain here a nearly constant pressure course along the perimeter. By decreasing the axial clearances, the velocities at the shroud-band's front side increase and cause very large pressure differences along the perimeter, as shown by the calculations for s_{ax} = 0.5 mm, for instance. A direct comparison with measurements is not possible, since the drill-holes for the first measurement plane are already over the shroud-band (cf. Figure 4.7). This measurement plane's low pressure must be attributed, at the tangential angle ψ = 180°, for instance, to a flow separation due to cross-section enlargement, which passes from a clearance width s_{ax} = 0.5 mm for the radial entrance, to the locally large radial clearance $\tilde{s}$ = 1.7 mm. During calculations, this would be taken into account by means of contraction coefficients. In addition, the bend-loss coefficients could not be considered constant, as here, but dependent on the local geometry.

/133

Experiments with modified afflux conditions are particularly suited to test the calculations procedure. In a turbine, these conditions can be affected by the percentage reaction, which essentially can be modified with the rate of rotation and the pressure differential for the entire step. Starting from a central operating condition, the pressure curves for both possibilities of variation are shown in Figure 4.20; the simple gauge ring B1 (see Figure 4.7) was used. It has only two drill-holes in the frontal and back measurement planes, which however are so arranged along the perimeter that the course of the curve can be determined from positive and negative eccentricity. With increasing pressure differentials the amplitudes of the pressure curves become larger and at lower rotation rates the position of the pressure maxima shifts.

Figure 4.21, below, shows the slopes of the transverse forces acting on the rotor, as a function of its pressure differential. Due to the reduced number of measurement points, these forces /134

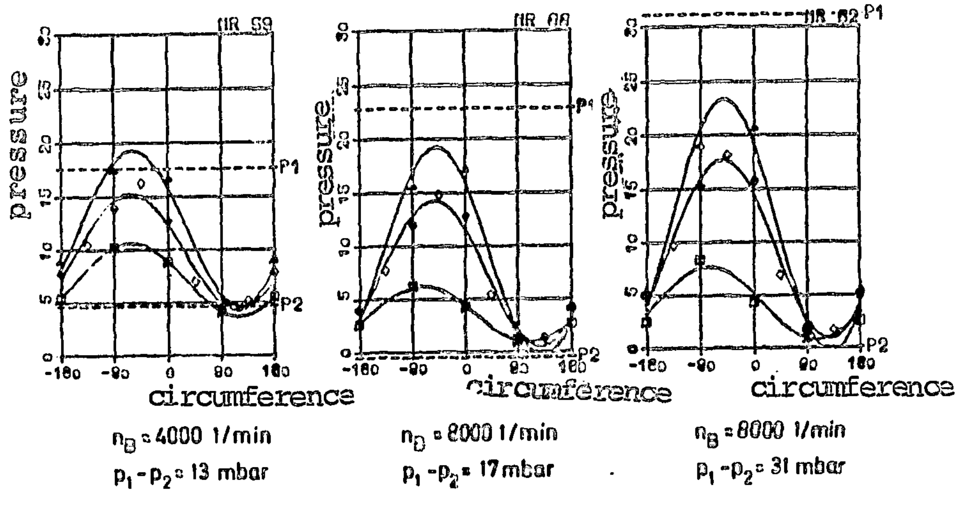

Figure 4.20 Pressure distribution for a plain rotor clearance, e = 0.6 mm, s_{ax} = 1.0 mm

measurement: for housing insert B1 with matched sine function

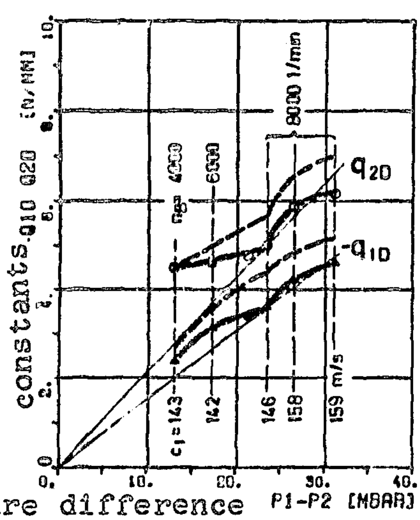

pressure difference

Figure 4.21 Plain shroud-band (B1)

measurement calculation

linear course for ....

were determined based only on the pressure curves of the central measurement plane. Since according to Figure 4.18 the course of the pressure is non-linear in axial direction, the transverse forces thus determined must be considered only qualitatively; nevertheless, the same assumptions were made in the comparative calculations shown. The clearance excitation and restoration coefficients measured increase with increasing rotor pressure gradients. However, different tendencies are noticed for the two pressure gradient variation possibilities. The cause for this is not so much the change in the loss coefficients brought about by the rotating channel wall (cf. Figure 3.24), but must be attributed mainly to the effect of the afflux velocity c_1. During the tests performed at constant rate of rotation n = 8000/min, the relative afflux energy was of approximately the same magnitude (cf. Appendix) and hence, according to Figure 3.26 and equation (3.55), the compressive forces are a linear function of the pressure differential. In contrast, during the variation of the rotation rate the afflux velocity c_1 was nearly constant, due to which according to Figure 3.24 the excitation forces increase parabolically with the pressure differential.

Both tendencies were well described by means of the calculations performed using the data in Figure 4.20. If more precise results can not be expected, it is only because due to a measurement uncertainty of 1% in the throughput and a reading error of 1 mm Hg in the pressure differential for the step, the pressure difference $p_1 - p_2$ for the rotor may already be affected by an error of 5 mbar. Systematic errors that could be included in the simplified calculation of p_1 from equation (4.13) have not been taken into consideration here.

/135

Figure 4.22, below, shows the clearance excitation constants over the axial clearance, for measurement sequences with approximately equal throughput. On the one hand, these constants were determined from the transverse forces acting on the entire step (q_2). In comparison to them, the portion q''_{2D} has been plotted which on the other hand is obtained by integration of the measured pressure distribution over the rotor shroud-band. Starting from the measurement point at s_{ax} = 0.5 mm, a constant

force measurement on entire stage
from pressure distribution (cover band)
theory for rotor gap

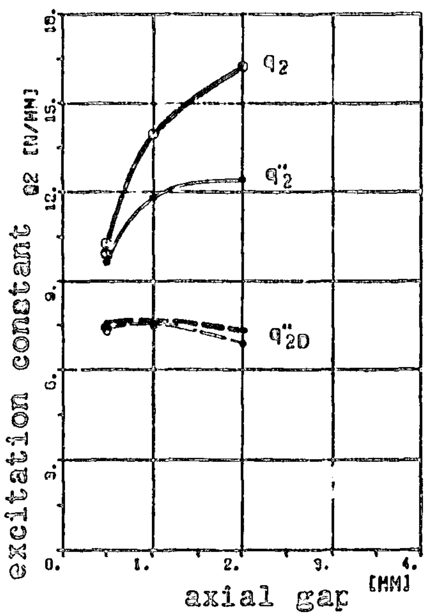

Figure 4.22 Plain shroud-band (B2)

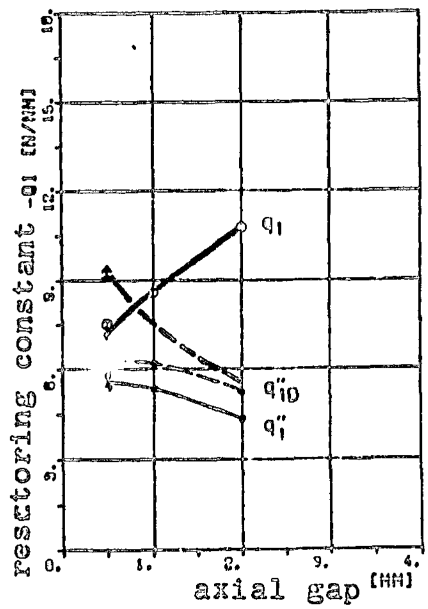

Figure 4.23 Plain shroud-band (B2)

course across the axial clearance may be assumed for the slope of these forces, which is qualitatively confirmed by measurements with the housing insert B1 (cf. Appendix, MR 62 to 64). These slopes q''_{2D} are also confirmed very clearly by calculation. Besides the compressive forces, the calculated slope q''_2 contains the portion q''_{2s}, caused by the variable rotor clearance loss. The transverse forces arising from the stator clearance loss, represented by the difference $q'_2 = q_2 - q''_2$, were not calculated here (however, see $Q^{\times}_{2s}$ in Figure 3.39 for a qualitative comparison).

/136

Figure 4.23, above, shows the restoration coefficients on a similar plot; the portion due to the pressure distribution was again plotted as a qualitative course from comparable measurements. The restoration coefficients calculated from the rotor clearance pressure distribution agree with the measurements only for large axial clearances, due to the deviation explained on the basis of Figure 4.19. The transverse forces (q_1) for the entire step increase with increasing axial clearance; evidently the portion $q_1' = q_1 - q_1''$ can not be neglected here. For the small axial clearance $s_{ax} = 0.5$ mm, a transverse force acting in the direction of deviation is generated in the stator clearance, which based on a sample calculation for a similar clearance form, had already been shown in Figure 3.39 ($s_{ax} \approx SA$). The restoration constant q_1'' calculated only from the rotor clearance flow is always somewhat lower than the portion q_{1D}'' from the pressure distribution, for torsional flow.

4.5.2. Labyrinths with two seal-peaks

The pressure curves measured in the chambers of the dioptric labyrinth (cf. Figure 4.7 C) for an eccentric rotor position are shown in Figure 4.24 for three axial clearance widths. Also drawn was the pressure P1 in front of the rotor, calculated for the central section from measured values; it increases with decreasing axial clearance, because a better seal effect is then achieved. Recalculated for the radius of the clearance entrance, a pressure is obtained that for a large axial clearance approximately corresponds to that measured in front of the first seal peak. Noticeable pressure differences are observed in this chamber only for a very small axial clearance. For s_{ax} = 2.0 mm, the measured value deviates a little from the fitted sine function, which can be attributed to an untight seal at ψ = 0 and $\psi = \pm 180$. Due to it, locally higher velocities and hence, somewhat lower pressures, could occur. In the chamber between the two peaks the pressure curve's amplitudes depend only little on the magnitude of the axial clearance. Behind the last peak /138
the pressure is nearly constant along the perimeter and corresponds approximately to the pressure P2 measured in the

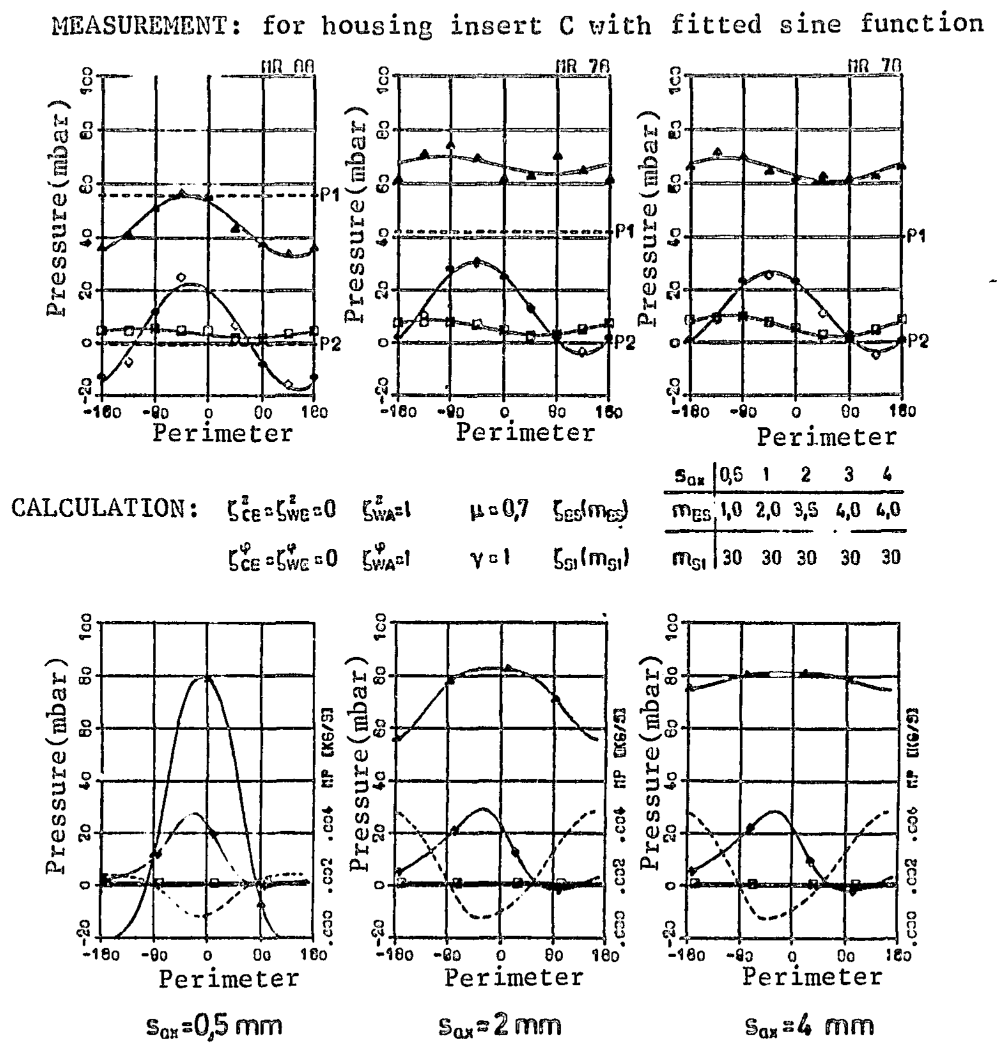

△ before first peak, ◇ labyrinth chamber, □ after last peak
-- local throughput (calculated)

Figure 4.24 Pressure distribution for a rotor clearance with two seal peaks, e = 0.7 mm

central section, behind the rotor.

For the labyrinth, a calculation of the pressure curves depends very much - as shown in section 3.6 - on the assumptions made for the pressure and impulse loss coefficients at the seal-peaks. Assuming a constant contraction coefficient $\mu = 0.7$, the calculations were performed with the pressure loss coefficients from equations (3.40) and (3.41). Through the constants applicable to the seal geometry, these coefficients depend on the local clearance widths and flow angles. The impulse loss coefficient was determined as a factor $\gamma = 1$ from equation (4.49), as a function of the corresponding pressure loss coefficients. Based on the considerations in relation to Figure 3.29, a pressure equalizing flow was not taken into consideration. In addition, the channel widths for the individual stream tubes were assumed to be constant, based on the same assumption, i.e., that this effect is balanced by corresponding local variations in the loss coefficients.

In agreement with the measurements, a relatively low pressure level is observed in the central chamber, caused by the first peaks's low loss coefficient and the changes in the flow angles within the clearance. The amplitudes for these pressure curves are approximately as high as those measured. The very small axial clearance $s_{ax} = 0.5$ mm caused considerable pressure differences in front of the first peak (cf. Figure 4.19), due to the variable velocities in the radial entrance. With the existing empirical loss coefficients, no better agreement between measurement and theory can be attained in this chamber. It remains unclear, in addition, whether the assumption is warranted that the pressure in the chamber before the first seal-peak remains constant, with turbulence and simultaneous redirection of the velocity. It would be conceivable that due to cross-currents within the chamber, the pressures determined through existing measurement drill-holes (cf. Figure 4.7) are not representative for the entire chamber.

/139

By means of section 3.3.4., the loss coefficients can be determined in such a way from the available measurements, that complete agreement exists between the measured and the calculated pressure curves. But this approach also depends on assumptions that limit the general validity of the result. Agreement will especially not be achieved, with the contraction coefficients chosen, if we start from a relationship between pressure and impulse loss coefficients described by means of a factor γ assumed constant along the perimeter (cf. equation (3.49)). Because according to Figure 3.36, the pressure curves are considerably affected by even small changes in the flow angle.

Assuming constant impulse loss coefficients, for instance, the pressure loss coefficients shown in Figure 4.25 (A) below

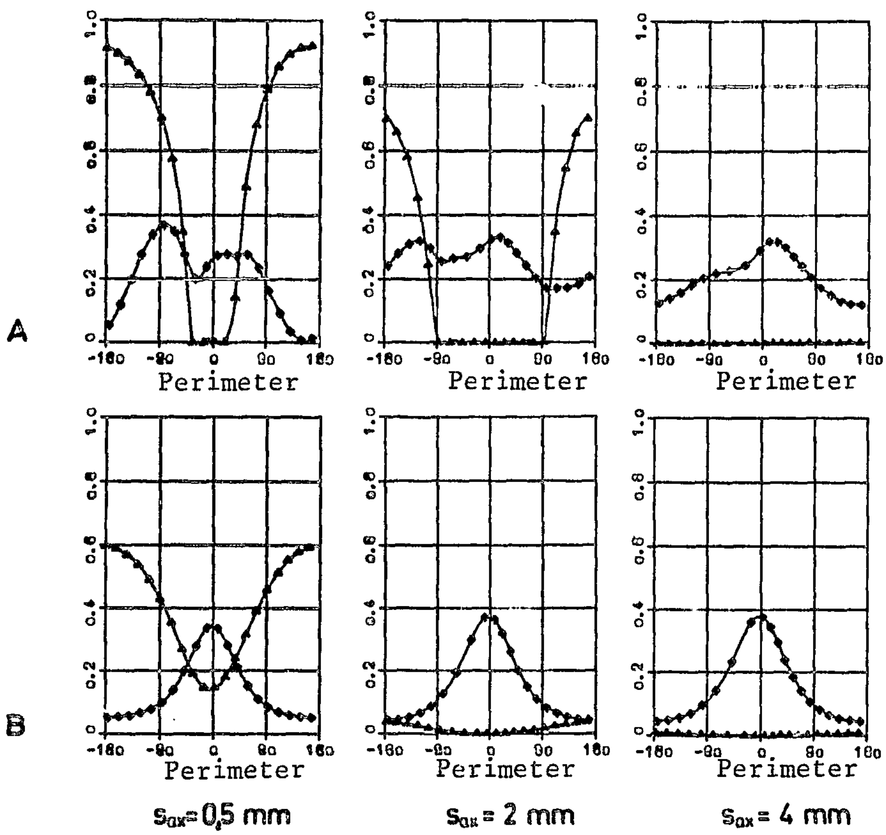

▵ ζ_{ES} chamber before 1st peak, ◇ ζ_{S1} after 1st peak
A from measured pressure curves (Fig.4.24), $\bar{\zeta}$ = 0.2
B used for calculation in Fig.4.24 with $\bar{\zeta}(\gamma,\zeta)$

Figure 4.25 Loss coefficients for rotor clearance with two seal peaks are obtained, which are confirmed qualitatively also for other assumptions regarding the impulse loss coefficients. Disregarding small deviations obtained for the limiting values $\zeta = 0$ and $\zeta = 1$, the measured pressure curves are described exactly by means of these coefficients. However, no unequivocal dependence on the local geometry can be formulated, described for instance in terms of clearance widths, flow angles and distances between peaks, or also by the seal peaks' edge sharpness. For a large axial clearance, the loss coefficients ζ_{ES} for the radial entrance become very small. For this reason the equations taken from the literature (Figure 4.25 (B)) - as shown in Figure 4.24 - yield useful results that are sufficient for turbine steps, since for the usual axial clearance construction approaches, the axial clearance at the radial entrance is much larger than the radial clearance width.

Figure 4.26 shows the measured clearance excitation constants as a function of the axial clearance, in comparison to calculations

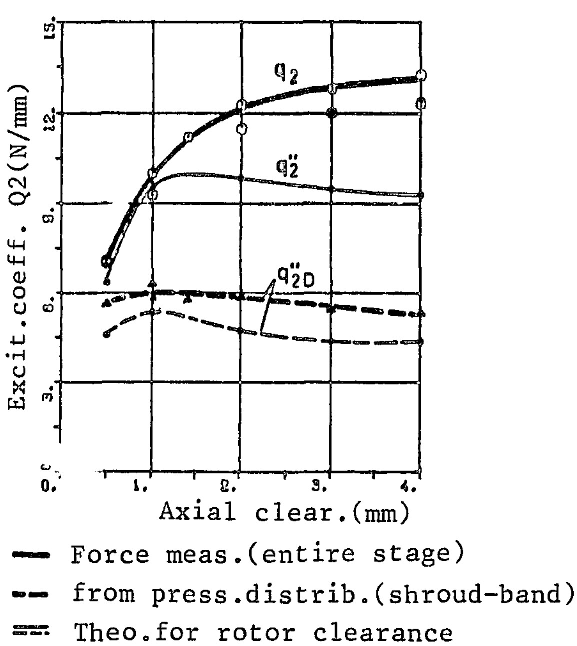

Figure 4.26 Two seal peaks

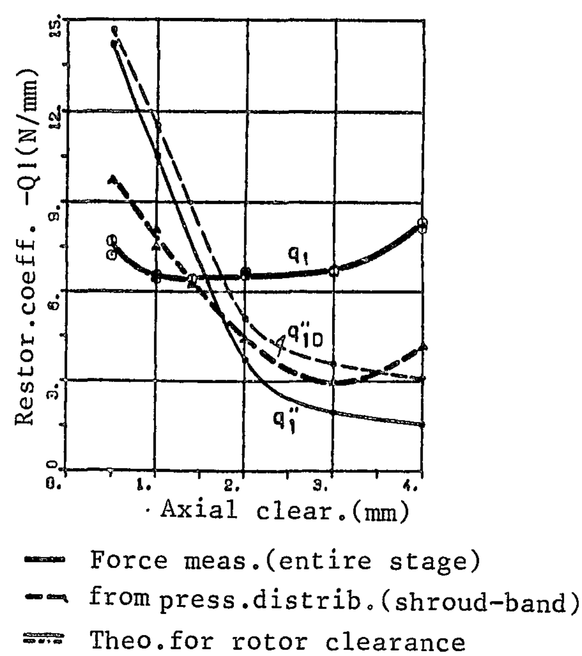

Figure 4.27 Two seal peaks

performed with the data from Figure 4.24. While the transverse force out of the pressure distribution is nearly constant, the total force increases, because the clearance loss increases with increasing axial clearance width. This course is confirmed also by calculations containing only the portion of clearance flow coming from the rotor. The excitation force from the stator seal can be determined as the difference ($q_2 - q_2''$) between the /140 measured total force and the forces determined from the rotor's clearance flow. While the stator clearance loss of the turbine steps studied is just as large as the rotor's (cf. Appendix), due to the equalizing flows only weak excitation forces are generated here.

/141

The restoration constants are shown over the axial clearance, in Figure 4.27, above. The transverse force out of the rotor clearance's pressure distribution is larger, at s_{ax} = 0.5 mm, than the total force measured at the runner, since the stator clearance has the same effect as in Figure 4.23. The theoretically determined restoration force increases very steeply at small axial clearance widths, which may be attributed to the course of the pressure ahead of the first seal peak (see Figure 4.24). Disregarding a small axial clearance, the calculation procedure provides good agreement with measurements, despite the uncertain loss coefficients for the transverse forces (q''_{1D}, q''_{2D}) out of the rotor clearance's pressure distribution. Taking into consideration the transverse forces generated in the stator clearance (cf. qualitatively $Q_1^\times$ and $Q_2^\times$ in Figure 3.39), the forces measured for the entire turbine step (q_1, q_2) can also be completely explained.

/142

4.5.3. Off-set shroud band with three seal peaks

While the dioptric labyrinth was somewhat more favorable as to its seal effect than the plain shroud band, it was possible to considerably increase the step's effiency by means of the off-set labyrinth common in turbine construction (cf. Figure

4.15). The pressure distributions along the perimeter, shown in Figure 4.28, below, were measured in the chambers before the

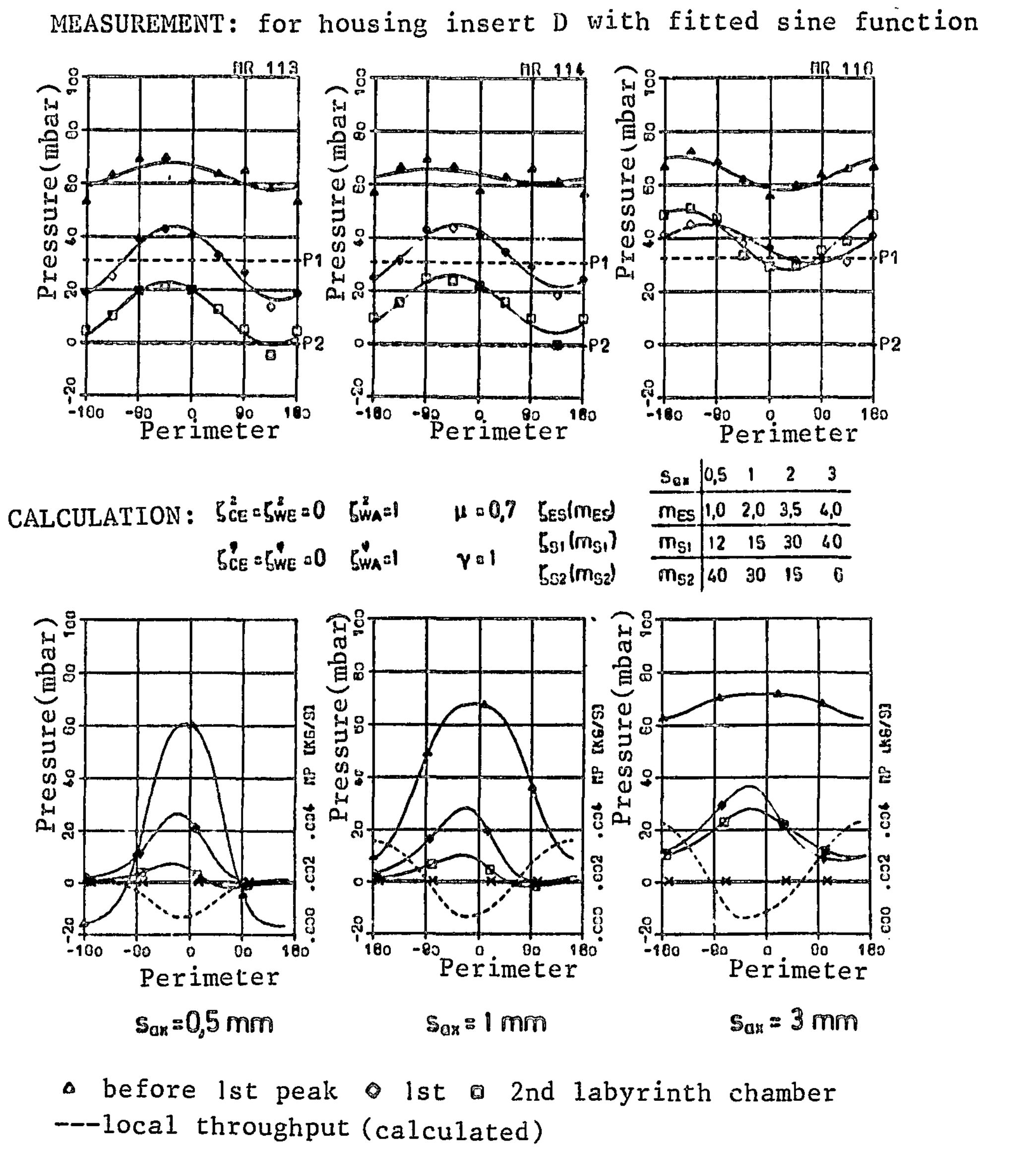

Figure 4.28 Pressure distribution for a rotor clearance with three seal peaks, e = 0.7 mm

first seal peak and between the first and second peaks (see Figure 4.7 (D)). From the results obtained for the dioptric labyrinth, it can be anticipated that the pressure is constant, beyond the last peak and corresponds to the pressure P2 measured beyond the rotor.

Along the perimeter the pressure distributions are similar to those for the dioptric labyrinth; the measurements in the chamber before the first peak again lead us to suspect an untight seal. The pressure course for an axial clearance $s_{ax} = 3$ mm constitute an exception. Here the clearance between the last peak and the front of the shroud-band shoulder becomes very small, and the pressure in the chamber increases, due to the better seal effect. In this arrangement of the seal peaks with respect to shroud-band shoulder, the position of the pressure maximum is also displaced considerably against the direction of torsion.

The theoretical pressure curves were calculated under assumptions similar to those made for the dioptric labyrinth, with the constants for the variable loss coefficients given according to the seal peak positions. Here too, because of the small clearance at the radial entrance, excessive pressure differences occur, while the agreement is better for the amplitudes and phase angles of the pressure curves corresponding to the central chambers. For the large axial clearance $s_{ax} = 3$ mm, the pressure levels in the individual chambers can be reflected by corresponding loss coefficients. The pressure distributions along the perimeter, however, agree only little with the measurements, since the flow cross-sections changed due to the peak positions were not taken into account. In addition, from the position of the measured pressure maxima it must be /144
concluded that due to the oblique oncoming flow at the last peak, a redirection of the flow occurs in tangential direction.

The slopes of the measured excitation constants are shown in Figure 4.29, in comparison to the calculated values. The portion due to the pressure distribution is practically independent of

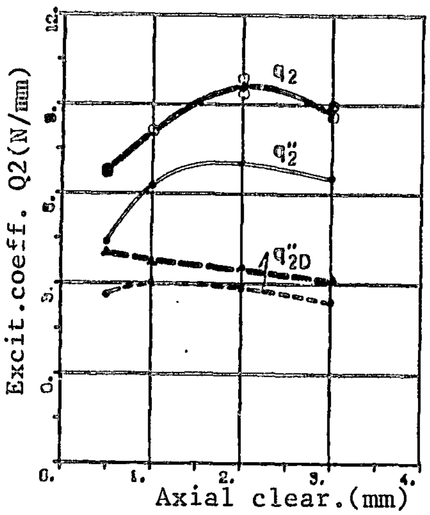

Force meas.(entire stage)
from press.distrib.(shroud-band)
Theo.for rotor clearance

Figure 4.29 Three seal peaks

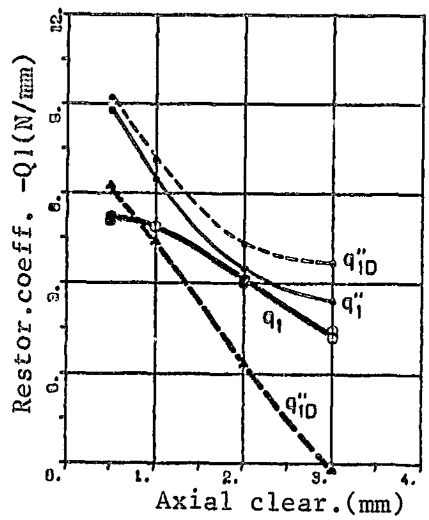

Force meas.(entire stage)
from press. distrib.(shroud-band)
Theo.for rotor clear.

Figure 4.30 Three seal peaks

the axial clearance, as was true of other clearance forms. The slope of the excitation force at the stator - formed as the difference $q_2 - q_2''$ between the measured value for the entire step and the value calculated for the rotor - agrees with the results for plain rotor clearances and for the dioptric labyrinth.

The restoration constants decrease with increasing axial clearance, under the effects of compressive forces, as shown in Figure 4.30. The restoration constants calculated from the rotor pressure distributions agree only qualitatively with the measured values, due to deviations in the pressure curves already explained in connection with Figure 4.28. The difference $q_1 - q_1''$, between the measured total force and and the /145
compressive force, corresponds to the compressive forces generated in the stator clearance, if we disregard the small restoration forces out of the rotor clearance loss. This course, which can also be recognized in Figure 4.27, is qualitatively

confirmed by the complete calculation in accordance with Figure 3.39 for a stator clearance with radial entrance and exit.

It was also possible for the set-off shroud band to determine the loss coefficients in such a manner that the measurements are reproduced exactly. However, it is not possible to provide a generally valid dependence on the local seal geometry, which is here expanded with the shroud-band shoulder. It should nevertheless be expected for the calculated transverse forces to provide better agreement, for the axial clearances that are usually much larger than the radial clearance widths. Special cases, though, resulting from the position of the seal peaks with respect to the shroud band shoulder - as occur in Figure 4.28 for s_{ax} = 3 mm - are excepted.

4.6. Forces due to a rotor-to-housing inclination

Normally, according to Figure 2.5, an inclination of the rotor with respect to the housing occurs only coupled to rotor eccentricity, with the ratio of the axial clearance change a to the eccentricity e being a function of the deflection bending line, the rotor diameter and the arrangement of the turbine step between the bearings. In order to test whether the forces due to both kinds of deviation are additive, a separate and a common displacement were performed on the test turbine. Figure 4.31, below, shows a plot of the relative excitation force Q_2/U_s over the eccentricity e (MR 76) and the force Q_3/U_s over the inclination a = 0.535e (MR 80). Furthermore, the displacement was performed in such a manner that under the action of both effects the forces became larger in one case (MR 84), but smaller in the other (MR 83). Within the measurement precision, they can be readily composed from individual measurements, with the same conclusions also being applicable to the restoration

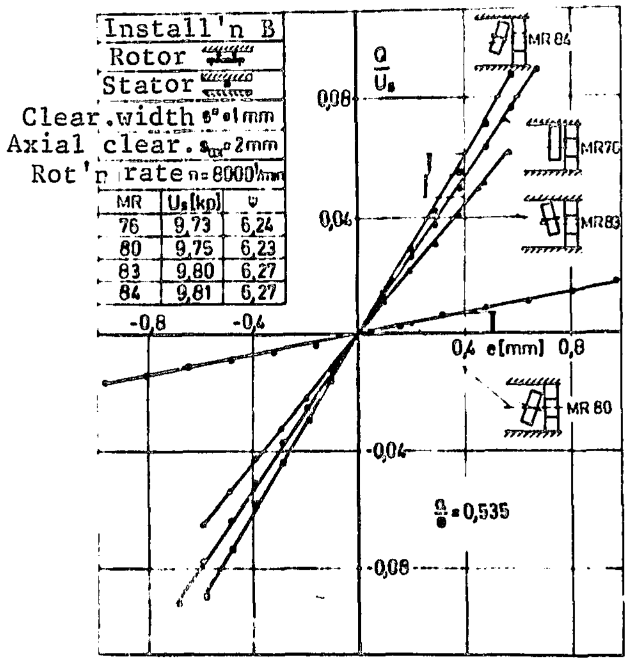

Figure 4.31 Relative excitation forces over the eccentricity and the inclination of the rotor with respect to the housing

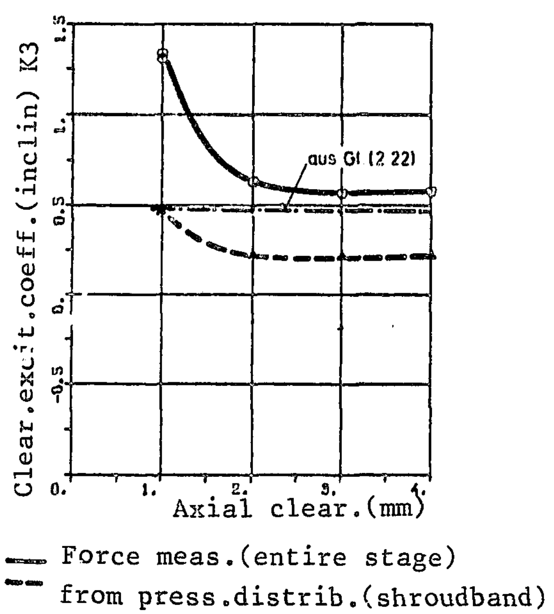

Figure 4.32 Two seal peaks

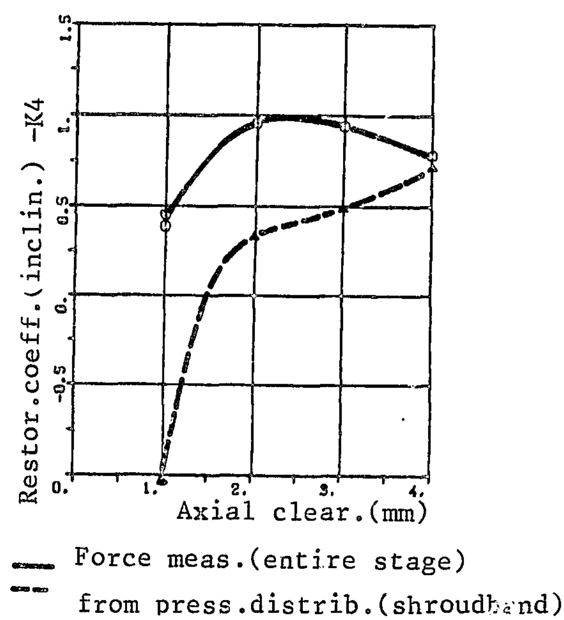

Figure 4.33 Two seal peaks

forces Q_1 and respectively, Q_4. The ratio of the two deviations selected here corresponds approximately to the maximum to be /146 expected for a high-power turbine. The excitation forces for the steps at the turbine entrance were increased here by approximately 10%, with those at the exit being correspondingly reduced (cf. Figure 2.5).

Figure 4.32, above, shows a plot of the dimensionless slope of the excitation force generated due to the rotor's inclination. The clearance excitation coefficient decreases strongly with increasing axial clearance and then attains a constant limiting value; the portion originating in the pressure distribution acts similarly. In the calculation of the theoretical coefficient according to equation (2.22), it was assumed that the entire clearance loss at the rotor was due to the axial seal effect. For this reason, for the large axial clearance the sum of the theoretical forces out of the clearance loss and out of the pressure distribution yields excessively high values. Due to the linear clearance loss equation, the theoretical coefficient is independent of the axial clearance. The restoration coeffi- /147 cients are shown in Figure 4.33, above. The forces originating in the pressure distribution depend particularly strongly on the axial clearance width, here.

The pressure differences generated due to an inclination of the rotor with respect to the housing are shown in Figure 4.34, below, for various axial clearances. In accordance with its definition, the axial clearance - now variable along the perimeter because of the inclination - is smallest at $\psi = 0$. Correspondingly, this is also where the highest velocities occur, which cause a minimum in the pressure curve in the chamber before the first seal peak. For a large axial clearance this effect no longer exists, due to the smaller pressure differences. The position of the now only weakly marked pressure maximum in the central chamber depends on the axial clearance width. The pressure differences are small in comparison to those

MEASUREMENT: for housing insert C, with fitted sine function

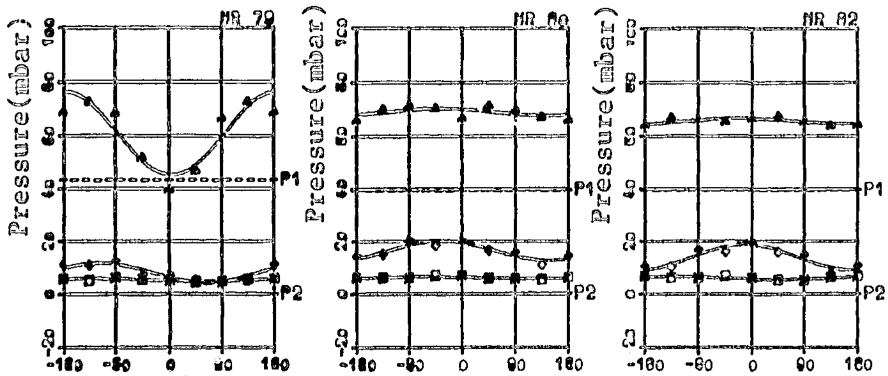

$c = 0{,}52$ mm, $s_{ax} = 1$ mm; $a = 0{,}69$ mm, $s_{ax} = 2$ mm; $a = 0{,}69$ mm, $s_{ax} = 4$ mm

▲ before 1st peak, ◇ Labyrinth chamber, ▫ after last peak

Figure 4.34 Pressure distribution for a rotor clearance with two seal peaks

generated for an eccentric ro. r position, even though very large axial clearance changes were tested, such as would hardly be possible with a vibrating turbine shaft.

/148

Assuming a linear clearance excitation theory, it is possible to formulate a relationship between the excitation force caused by the inclination of the rotor, and efficiency curve. From equations (2.19) to (2.22) we obtain the slope of the local clearance loss over the axial clearance,

$$\frac{\zeta_{Sp,a}}{s_{ax}} = 2\,\frac{a_{3s}}{U_s/l''} = 2\,\frac{K_{3s}}{l''}$$

as a function of the clearance excitation coefficient K_{3s}, caused by the changes in the local tangential force. It can be determined as the difference $K_{3s} = K_3 = K_{3D}$ between the total clearance excitation coefficient and the portion due to the pressure distribution, from the available measurements. Figure

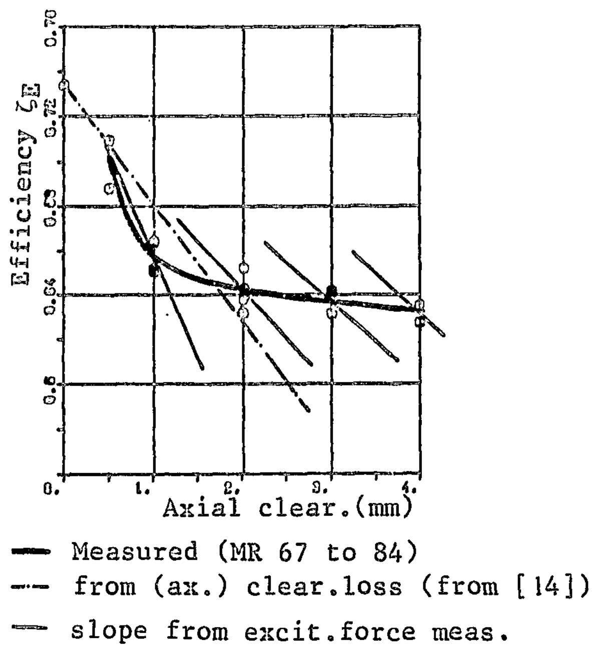

Figure 4.35 Two seal peaks

4.35, above, shows the efficiency curve, as a function of the axial clearance. Starting from the calculated tangential efficiency for the step, the linear efficiency decrease which results from the clearance loss due to the shroud-band entrance shoulder, is plotted, according to equation (2.19). The slopes /149
determined from the excitation force measurements are qualitatively in agreement with the non-linear efficiency curve. However, there are deviations for large axial clearances, caused either by compressive forces at the stator clearance, or due to the fact that an inclination of the rotor can also cause small radial clearance changes. If we take these side effects into consideration, the relationship between the excitation forces and the efficiency course seems sufficiently confirmed also for the case of an inclination between rotor and housing.

5 SUMMARY

The rotors of thermal turbomachines can become endangered by self-excited vibrations that may impose severe output restrictions on the affected power plants, if these vibrations are caused by clearance excitation. For a theoretical description of the system, it is necessary to know the transverse forces that act in dependance on a deviation of the rotor from its centered position with respect to the housing. The component perpendicular to the direction of deviation acquires special significance, since in circumpolar vibrational movement it act; by setting up vibrations in the turbine shaft.

The excitation force can be described as the resultant of the turbine stage's tangential force, which becomes variable for an eccentric rotor position. Therefore, for a given rotation rate, it is a function of the stage's output and of the course of the clearance loss over the radial clearance width. In the case of blading with shroud-band, the excitation forces can be considerably enhanced due to a variable pressure distribution in the rotor's seal clearance. This effect was studied in detail by means of a calculation procedure in which the torsionally affected flow at the clearance - caused by the main flow, in turbine stages - was especially taken into account.

Sample calculations show that the excitation forces due to a pressure distribution in the seal clearance increase with increasing pressure gradient and especially, with increases in the tangential velocity before the clearance. However, the characteristic quantity is the relative afflux energy, to be obtained from the dynamic pressure of the tangential velocity before the clearance, related to the pressure gradient operating at the seal clearance. Correspondingly, because of the large relative afflux energy at turbine stages in impulse

construction, larger excitation forces become active due to the pressure distribution over the rotor's shroud-band, than in /151 reaction stages. However, the form of the seal clearance and the empirical loss coefficients, which describe the clearance flow as a function of the geometry, also have a significant effect on the magnitude of the excitation forces.

The experimental studies were performed on an impulse turbine stage, varying the rotor's clearance form. The rotor was mounted in a kind of two-component balance, connected to a dynamometrical brake; the transverse forces were measured as a function of its deviation with respect to the housing. By means of efficiency measurements at various radial clearance widths, it was possible to show that for blading without shroud-band the excitation forces could be calculated from the clearance loss alone. In contrast, for the bladings with shroud-bard investigated, in spite of lower clearance losses, larger excitation forces were observed; these could be explained by means of measurements of the pressure distribution at the rotor clearance.

Considering the complexity of the flow processes in a seal clearance, the agreement between the measured pressure curves and the theory is relatively good; minor deviations - especially for small axial clearance widths, can be explained in terms of the simplifying assumptions made regarding the loss coefficients. For the usual constructions, the transverse forces acting on a turbine stage - caused by the clearance loss, on the one hand, and the pressure distribution along the rotor perimeter, on the other - can be determined with sufficient accuracy.

/152

6 DESIGNATIONS USED

A	surfaces, flow cross-sections
a	specific work, axial clearance change due to inclination
b	seal clearance length
$C_E^{\times}$	relative afflux energy
c	absolute velocity at blading
c_p	specific heat capacity
d	diameter
EB	insert condition to describe stage geometry
e	eccentricity of the rotor with respect to the housing
f_L	control magnitude (plain clearance - labyrinth)
h	chamber height
Δh_s	isentropic gradient
K', K''	clearance loss coefficients
K	coefficient for the transverse forces of the flow medium
l	blade length, flow paths in the control space
MR	measurement sequence number
m	mass, constant for seal peak loss coefficients
$\dot{m}$	throughput
n	rotation rate
P	output, compressive force on control space
p	pressure
Q	transverse force of the flow medium
q	coefficient for the transverse force depending on the deviation
Re	Reynold's number
r	radii
S	support force
s	clearance width
T	temperature
t	distance of the seal peaks
U, U_s	tangential or peripheral force, isentropic tangential force

u tangential or peripheral velocity
v, w velocities within the clearance
w relative velocity at the blading
x, y, z spatial coordinates
z', z'' number of seal peaks

/153

α flow angle, angle of rotor inclination
α, β flow angles at turbine blading
ζ, $\bar{\zeta}$ pressure loss and impulse loss coefficients
η efficiency
$\varkappa$ isentropy exponent
λ friction coefficient
μ contraction coefficient
ρ density
ψ tangential or peripheral angle, bending angle
ϕ pressure coefficient of the turbine stage
ω angular velocity
$\mathfrak{L}$, $\mathfrak{w}$ load vector
$\mathfrak{K}$ load matrix proportional to the deviation
$\bar{\mathfrak{K}}$ load matrix proportional to the velocity
$\mathfrak{r}$ percentage reaction

Subscript and superscripts:

$^{\times}$ dimensionless representation
$\tilde{}$ clearance width variable along perimeter
$'$ stator
$''$ rotor
1 in the direction of deviation
2 perpendicular to direction of deviation (preceding the direction of rotation)
A radial exit
B reference magnitude
D from pressure distribution
E radial entrance
i, n support point in flow direction
k, j support point in tangential direction

S radial clearance

s originating in clearance loss

Stage control surfaces:

0 before the stator

1 between bladings

2 behind rotor

7 REFERENCES

1 Thomas, H.-J., Instabile Eigenschwingungen von Turbinenlaeufern, angefacht durch die Spaltstroemung in Stopfbuchsen und Beschauflung [Unstable natural vibration of turbine rotors induced by the clearance flow in glands and blading], Bull. de l'A.I.M. 71, No.11/12, 1039-1063 (1958).

2 Kraemer, E., Selbsterregte Schwingung von Wellen infolge von Querkraften [Self-excited vibration of shafts due to transverse forces], BWK 20, No.7, 307-312 (1968).

3 Pollmann, E., Stabilitaet einer in Gleitlagern rotierenden Welle mit Spalterregung [Stability of a shaft rotating in friction bearings, under clearance excitation], Fortschrittsbericht VDI-Zeitschrift Reihe 1 [Progress Report, VDI (Association of German Engineers) Journal Series 1], No. 15 (1969).

4 Thomas, H.-J., Grenzleistungsprobleme bei thermischen Turbomaschinen [Limiting output problems in thermal turbo-machines], Mitt. VGB 51, No. 4, 286-293 (1971)

5 Thomas, H.-J., Urlichs, K. and Wohlrab, R., Laeuferinstabilitatet infolge Spalterregung [Rotor instability due to self-excitation], Forschungsvereiningung Verbrennungskraftmaschinen [Research Association for Internal Combustion Engines], Frankfurt, Issue 167 (1974)

6 Glienicke, J., Experimentelle Ermittlung der statischen und dynamischen Eigenschaften von Gleitlagern fuer schnellaufende Wellen. Einfluss der Schmierspaltgeometrie und der Lagerbreite [Experimental determination of the static and dynamic characteristics of friction bearing for

high speed shafts. Effect of the lubrication clearance geometry and of the bearing width], Progress Report, VDI Journal Series 1, No. 22 (1970).

7 Gasch, R., Stabiler Lauf von Turbinenrotoren [Stable running of turbine rotors], Konstruktion 17, No. 11, 447-452 (1965).

8 Gasch, R., Unwucht-erzwungene Schwingungen und Stabilitaet von Turbinenlaeufern [Unbalance-forced vibrations and stability of turbine rotors], Konstruktion 25, No. 5, 161-168 (1973).

9 Vogel, D. H., Die Stabilitatet gleitgelagerter Rotoren von Turbomaschinen unter besondere Beruecksichtigung einer Erregung durch Spaltstroeme [The stability of friction bearing-supported turbo-machine rotors with special consideration to clearance flow excitation], Dissertation, Munich Institute of Technology, 1969.

10 Schirmer, G. F., Zur Stabilitaet der Schwingungen von Turbinenwellen [On the stability of turbine shaft vibrations], Dissertation, Darmstadt Institute of Technology, 1969.

11 Winter, C.-J., Lastabhaengige instabile Bewegung von Turbinenlaeufern [Load dependent, unstable motion of turbine rotors], Dissertation, Darmstadt Institute of Technology, 1968.

12 Piltz, E., Belastungen von Dampfturbinenlaufraedern bei Auslenkung der Welle [Stress on steam turbine rotors under shaft deviation], Konstruktion 24, No. 4, 141-148 (1972).

13 Piltz, E., Einfluss von Dampfbelastung auf die Stabilitaetsgrenze einer einstufigen Modellturbine [Effect of steam charge on the limit of stability of a single-stage

model turbine], Konstruktion 25, No. 4, 130-135 (1973).

14 Traupel, W., "Thermische Turbomaschinen" [Thermal Tubo-machines] Vol.1, (1st Ed.), Springer (Berlin, Goettingen, Heidelberg) 1958. (2nd. Ed.: 1967).

15 Trutnowsky, K., "Beruehrungsfreie Dichtungen" [No-contact seals], VDI Publishers, Duesseldorf 1973.

16 Truckenbrodt, E., "Stroemungsmechanik" [Flow Mechanics], Springer (Berlin, Heidelberg, New York) 1968.

17 Lomakin, A. A., Die Berechnung der kritischen Drehzahl und der Bedingungen fuer Sicherung der dynamischen Stabilitatet des Laeufers von hydraulischen Hochdruck-Maschinen unter Beruecksichtigung der Kraefte, die in den Dichtungen entstehen [Calculation of the critical speed and the conditions to insure the dynamic stability of hydraulic high-pressure machine rotors, taking into consideration the forces generated in the seals], Energomasinostroenie 4, No. 4, 1-5 (1958).

18 Domm, U., Dernedde, R. and Handwerker, Th., Der Einfluss der Stufenabdichtung auf die kritische Drehzahl von Kesselspeisepumpen [The effect of stage sealing on the critical speed of boiler feeders], VDI Report No. 113 (1967).

19 Kiesewetter, H. and Wolter, W., Einige Bemerkungen ueber die dezentrierende Kraft auf umstroemten Kolben [Some remarks on the decentering force on pistons immersed in flow], Maschinenbautechnik 12, No. 2, 69-73 (1963).

20 Alford, J. S., Protecting turbomachinery from self-excited rotor whirl, Transactions ASME, J. of Eng.f.Power 87, No. 10, 333-344 (1965).

21 Spurk, J. H. and Keiper, R., Selbsterregte Schwingungen bei Turbomaschinen infolge der Labyrinthstroemung [Self-excited vibration in turbo-machines due to the labyrinth flow], Ingenieur-Archiv 43, No. 2/3, 127-135 (1974).

22 Kostyuk, A. G., A theoretical analysis of the aerodynamic forces in the labyrinth glands of Turbomachines, Teploenergetika (Thermal Engineering) 19, No. 11, 29-33 (1972).

23 La Roche, U., Untersuchung der Stroemung ueber einen Absatz im Zusammenhang mit den Injektionsverlusten bei Dampf und Gasturbinen [Study of the flow across a set-off in relation to the injection losses in steam and gas turbines], Communication from the Institute for Thermal Turbomachines, Swiss Institute of Technology at Zurich, No. 10 (1965)

24 Neumann, K., Zur Frage der Verwendung von Durchblickdichtungen im Dampfturbinenbau [On the question of using dioptric seals in steam turbine construction], Maschinenbautechnik 13, No. 4, 188-195 (1964).

25 Neumann, K., Untersuchungen von Wellendichtungen fuer Dampfturbinen bei hohen Dampfparametern [Study of shaft seals for steam turbines under high steam parameters], Maschinenbautechnik 15, 27-31 (1966).

26 Groddeck, K.-H., Probleme der beruehrungsfreien Hochdruckstopfbuchsen [The problems of non-contact high-pressure glands], Forschung Ing.-Wesen 23, No. 5, 183-195 (1957).

/156

27 Stingelin, V., Theoretische und experimentelle Untersuchungen an Gaslagern [Theoretical and experimental

studies on gas bearings], Communications from the Institute for Aerodynamics, Swiss Institute of Technology at Zurich, No. 32 (1963).

28 Rosenberg, S. Sch., Orlik, W. G. and Marcenko, U. A., Untersuchung aerodynamischer Querkraefte bei einer Wellenexzentrizitaet [Study of aerodynamic transverse forces in the case of shaft eccentricity], Energomasinostroenie 8, 15-17 (1974).

29 Hochreuther, W., Kraefte bei axial durchstroemten Spalten [Forces in clearances with axial flow], Dissertation, Stuttgart University 1975.

30 Wohlrab, R., Spalterregung bei thermischen Turbomaschinen [Clearance excitation in thermal turbo-machines], Dissertation, Munich Institute of Technology (1975).

8 APPENDIX: TABLE OF MEASURED VALUES

The Table below lists the mid-section magnitudes of the test turbine and the slopes of the forces over the eccentricity for selected measurement sequences. The stage geometry is described by means of the insert as defined in section 4.2. The individual magnitudes are explained in the sequence of the computer print-out, with a listing for the equation number.

MR	Measurement sequence number
SAX	axial clearance
NB	operating speed
M	throughput, (4.1)
DHS	isotropic gradient, (4.2)
PSI	pressure coefficient, $\phi = 2\Delta h_s/u$
US	isentropic tangential force
ETAE	effective efficiency, (4.4)
ETAU	tangential efficiency, (4.5)
REAK	percentage reaction, (4.14)
REAM	percentage reaction from measurement p_{1w} (cf. Figure 4.4)
KSI	ratio $\zeta = \zeta''/\zeta_{sp}$, corresponds to q''_{2s}/q_{2s}
Q2S	theoretical excitation force, (2.15)
US/L	reference magnitude U_s/l for following constants
Q2	excitation coefficient (entire stage)
Q1	restoration coefficient (entire stage)
Q2D	excitation coefficient from pressure distribution
Q1D	restoration coefficient from pressure distribution
CES	relative afflux energy for rotor clearance, (3.24), recalculated for external tadius using (3.8)
PO	pressure before turbine stage p_o
DPO2	pressure difference $p_o - p_2$
DP12	pressure difference $p_1 - p_2$ from (4.13)
TO	temperature before stage [°C]
CO	afflux velocity, (4.6)
C1	stator exit velocity, (4.15)
C2	velocity behind rotor, (4.15)
AL2	outflow angle, (4.15)

MR	SAX	NB	M	DHS	PSI	US	ETAE	ETAI	ETAU	REAK	REAM	KSI	Q2S
--	MM	UPM	KG/S	KJ/KG	---	N	----	----	----	----	----	--	N/MM

Insert cond. 231 w/o shroud band (s=0.5 mm) Form A

MR	SAX	NB	M	DHS	PSI	US	ETAE	ETAI	ETAU	REAK	REAM	KSI	Q2S
39	0.5	8000	.389	14.8	5.50	78.5	.720	.704	.748	.222	.068	.57	7.2
40	1.0	8000	.389	14.7	5.48	78.2	.721	.694	.750	.213	.068	.57	7.2
41	2.0	8000	.389	14.8	5.51	78.7	.710	.715	.749	.219	.068	.57	7.2
42	3.0	8000	.389	14.7	5.48	78.2	.716	.720	.750	.212	.068	.57	7.2

Insert cond. 211 w/o shroud-band (s=1.0 mm), Form A

MR	SAX	NB	M	DHS	PSI	US	ETAE	ETAI	ETAU	REAK	REAM	KSI	Q2S
17	0.5	8000	.393	14.4	5.37	77.3	.628	.666	.764	.145	-	.57	7.1
16	1.0	8000	.393	14.1	5.26	75.8	.594	.651	.769	.121	-	.57	7.0
14	2.0	8000	.392	14.0	5.20	74.7	.579	.644	.771	.117	-	.57	6.9
15	3.0	8000	.392	14.1	5.25	75.6	.578	.639	.769	.121	-	.57	7.0

Insert cond. 221 w/o shroud-band (s=1.5 mm), Form A

MR	SAX	NB	M	DHS	PSI	US	ETAE	ETAI	ETAU	REAK	REAM	KSI	Q2S
30	1.0	8000	.398	14.0	5.22	76.3	.521	.357	.772	.105	.071	.57	7.0
31	2.0	8000	.398	14.0	5.22	76.2	.459	.357	.772	.105	.071	.57	7.0
27	2.0	8000	.399	14.0	5.21	76.1	.456	.331	.772	.105	.072	.57	7.0
32	3.0	8000	.398	14.0	5.22	76.3	.440	.357	.772	.105	.071	.57	7.0

Insert cond. 251 Plain shroud-band, Form B1

MR	SAX	NB	M	DHS	PSI	US	ETAE	ETAI	ETAU	REAK	REAM	KSI	Q2S
59	1.0	4000	.360	12.3	18.30	122.8	.495	.456	.56[illegible]	.091	-	.38	7.9
60	1.0	6000	.368	12.6	8.34	84.5	.617	.617	.709	.117	-	.47	6.3
66	1.0	8000	.385	13.6	5.06	71.5	.677	.523	.769	.145	-	.49	5.5
65	1.0	8000	.422	15.9	5.93	91.7	.659	.540	.755	.139	-	.50	7.3
64	0.5	8000	.429	16.7	6.22	97.7	.707	.599	.742	.169	-	.49	7.6
62	1.0	8000	.429	16.4	6.12	96.1	.666	.535	.747	.157	-	.50	7.7
63	2.0	8000	.429	16.2	6.02	94.5	.659	.522	.753	.132	-	.50	7.4

Insert cond. 281 Plain shroud-band, Form B2

MR	SAX	NB	M	DHS	PSI	US	ETAE	ETAI	ETAU	REAK	REAM	KSI	Q2S
89	0.5	8000	.423	16.9	6.29	97.7	.707	.770	.741	.171	.041	.49	7.6
--Throughput corrected MR 90 to 93--													
90	1.0	8000	.326	10.0	3.72	44.6	.671	.748	.788	.098	.046	.50	3.5
91	2.0	8000	.322	10.0	3.74	44.1	.660	.722	.786	.131	.054	.50	3.5
92	3.0	8000	.320	10.1	[illegible].70	49.4	.650	.744	.788	.100	.057	.50	3.6
93	4.0	8000	.331	10.3	3.[illegible]	46.5	.649	.740	.789	.091	.059	.49	3.6

Insert cond. 271 Two seal-peaks, Form C

MR	SAX	NB	M	DHS	PSI	US	ETAE	ETAI	ETAU	REAK	REAM	KSI	Q2S
68	0.5	8000	.400	16.2	6.03	88.4	.688	.731	.725	.284	.178	.49	6.4
75	1.0	8000	.416	16.8	6.24	95.3	.664	.727	.734	.217	.188	.43	6.6
76	2.0	8000	.417	16.8	6.24	95.4	.652	.706	.735	.210	.190	.42	6.6
77	3.0	8000	.418	16.7	6.21	95.1	.642	.701	.737	.201	.193	.42	6.5
78	4.0	8000	.418	16.7	6.20	95.0	.635	.704	.737	.200	.195	.42	6.5

Insert cond. 291 Three seal-peaks, Form D

MR	SAX	NB	M	DHS	PSI	US	ETAE	ETAI	ETAU	REAK	REAM	KSI	Q2S
113	0.5	8000	.406	14.8	5.52	82.3	.700	.776	.756	.175	-	.37	5.2
114	1.0	8000	.407	14.8	5.52	82.4	.688	.762	.756	.17[illegible]	-	.37	5.2
115	2.0	8000	.407	14.9	5.54	82.6	.687	.764	.756	.17[illegible]	-	.37	5.2
116	3.0	8000	.407	14.9	5.56	82.8	.696	.756	.754	.18[illegible]	-	.37	5.2

MR	US/L	Q2	-Q1	Q2D	-Q1D	CES	PO	UPO2	DP12	TO	CO	C1	C2	AL2
--	N/MM	N/MP	N/MM	N/MM	N/MM	---	MBAR	MBAR	MBAR	C	M/S	M/S	M/S	GRD
Insert cond. 231 w/o shroud-band (s=0.5 mm), Form A														
39	4.1	6.1	3.7	-	-	1.4	1143	187	39.3	23	24	145	41	64
40	4.1	8.6	4.3	-	-	1.4	1142	185	37.4	24	24	145	41	65
41	4.1	10.7	4.3	-	-	1.4	1143	186	38.0	24	24	145	41	64
42	4.1	12.0	5.6	-	-	1.4	1142	185	37.3	26	24	145	41	65
Insert cond. 211 w/o shroud-band (s=1.0 mm), Form A														
17	4.1	4.8	0.9	-	-	1.8	1129	179	24.5	25	25	150	37	71
16	4.0	6.1	0.3	-	-	2.0	1125	175	20.0	25	25	151	35	74
14	3.9	8.0	1.1	-	-	2.1	1123	173	19.2	24	25	150	34	75
15	4.0	8.4	1.7	-	-	2.0	1125	175	19.9	24	25	150	35	74
Insert cond. 221 w/o shroud-band, (s=1.5 mm), Form A														
30	4.0	5.0	-0.2	-	-	2.2	1135	175	17.3	25	25	151	34	76
31	4.0	6.5	0.5	-	-	2.2	1135	175	17.4	25	25	151	34	76
27	4.0	6.3	0.5	-	-	2.1	1134	175	17.4	23	25	151	34	76
32	4.0	7.1	1.3	-	-	2.2	1135	175	17.3	25	25	151	34	76
Insert cond. 251 Plain shroud-band, Form B1														
59	6.5	9.5	3.8	4.5	2.4	2.6	1092	149	13.0	24	24	143	72	33
60	4.4	10.1	5.8	4.6	3.1	2.1	1100	154	17.2	24	24	142	47	48
66	3.8	10.7	7.5	5.0	3.6	1.8	1117.	170	23.3	21	24	146	34	75
63	4.0	12.4	8.6	5.9	4.2	1.9	1150	202	26.4	21	26	158	41	64
64	5.1	10.3	6.8	5.1	3.3	1.7	1161	214	33.9	21	26	159	45	59
62	5.1	14.0	8.6	6.2	4.6	1.8	1158	211	31.1	19	26	159	44	61
65	5.0	16.2	10.8	6.2	4.1	1.9	1154	207	25.6	20	26	160	42	63
Insert cond. 281 Plain shroud-band, Form B2														
89	5.1	9.9	7.5	7.5	9.1	1.7	1160	213	34.2	25	26	160	46	58
---Throughput corrected MR 90 to 93---														
90	2.3	7.5	6.2	4.6	6.1	2.2	1067	119	11.3	25	22	128	27	114
91	2.3	8.7	7.8	3.9	3.0	2.0	1067	120	15.0	26	22	126	27	109
92	2.4	9.7	8.7	3.9	5.4	2.2	1069	121	11.6	26	22	129	27	112
93	2.4	9.5	9.2	3.6	4.5	2.3	1070	123	10.7	26	22	131	27	112
Insert cond. 271 Two seal-peaks, Form C														
68	4.7	7.0	7.2	5.6	9.7	1.1	1175	208	56.2	24	24	145	49	56
75	5.0	10.0	6.6	6.3	8.0	1.4	1167	213	43.6	25	26	155	48	57
76	5.0	12.3	6.7	5.8	4.4	1.4	1166	213	42.1	25	26	155	48	57
77	5.3	12.8	6.7	5.4	3.0	1.5	1165	212	40.0	25	26	156	47	58
78	5.0	13.2	8.4	5.3	4.1	1.5	1165	211	39.8	25	26	156	47	58
Insert cond. 291 Three seal-peaks, Form D														
113	4.3	6.7	5.2	4.0	6.2	1.6	1164	191	31.5	23	25	149	39	66
114	4.3	8.1	4.9	3.7	4.4	1.7	1164	191	31.3	23	25	150	39	66
115	4.3	9.4	3.0	3.5	0.3	1.6	1164	191	31.6	23	25	150	39	66
116	4.4	8.6	1.9	3.1	-3.1	1.6	1165	192	32.7	23	25	149	40	66